

Electrostatic coalescence and light scattering

Citation for published version (APA):

Bosch, van den, H. F. M. (1996). *Electrostatic coalescence and light scattering*. [Phd Thesis 1 (Research TU/e / Graduation TU/e), Chemical Engineering and Chemistry]. Technische Universiteit Eindhoven.
<https://doi.org/10.6100/IR470469>

DOI:

[10.6100/IR470469](https://doi.org/10.6100/IR470469)

Document status and date:

Published: 01/01/1996

Document Version:

Publisher's PDF, also known as Version of Record (includes final page, issue and volume numbers)

Please check the document version of this publication:

- A submitted manuscript is the version of the article upon submission and before peer-review. There can be important differences between the submitted version and the official published version of record. People interested in the research are advised to contact the author for the final version of the publication, or visit the DOI to the publisher's website.
- The final author version and the galley proof are versions of the publication after peer review.
- The final published version features the final layout of the paper including the volume, issue and page numbers.

[Link to publication](#)

General rights

Copyright and moral rights for the publications made accessible in the public portal are retained by the authors and/or other copyright owners and it is a condition of accessing publications that users recognise and abide by the legal requirements associated with these rights.

- Users may download and print one copy of any publication from the public portal for the purpose of private study or research.
- You may not further distribute the material or use it for any profit-making activity or commercial gain
- You may freely distribute the URL identifying the publication in the public portal.

If the publication is distributed under the terms of Article 25fa of the Dutch Copyright Act, indicated by the "Taverne" license above, please follow below link for the End User Agreement:

www.tue.nl/taverne

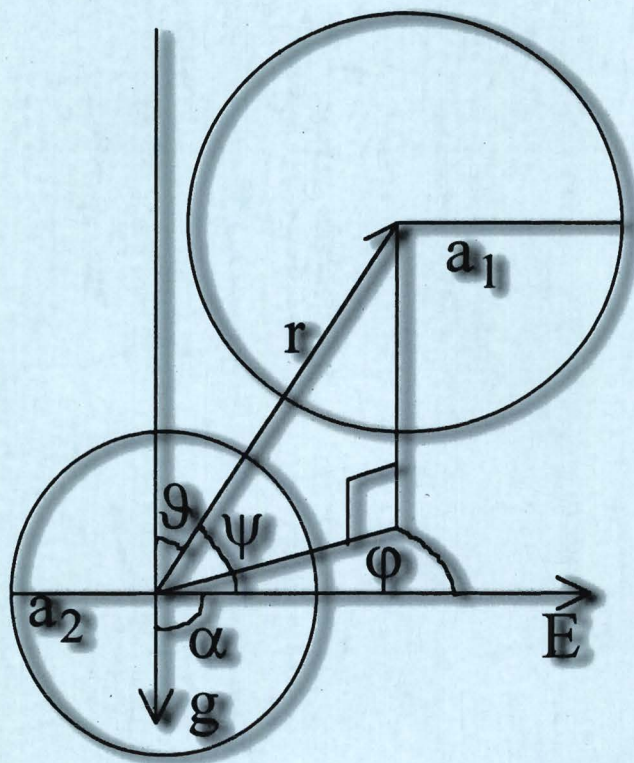
Take down policy

If you believe that this document breaches copyright please contact us at:

openaccess@tue.nl

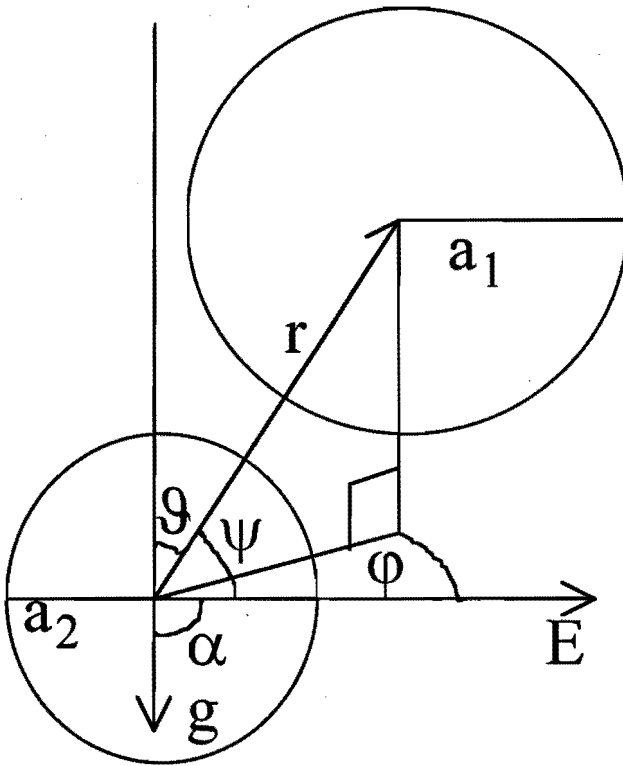
providing details and we will investigate your claim.

Electrostatic Coalescence and Light Scattering



Erik van den Bosch

Electrostatic coalescence and light scattering



Erik van den Bosch

Electrostatic coalescence and light scattering

PROEFSCHRIFT

ter verkrijging van de graad van doctor aan de
Technische Universiteit Eindhoven, op gezag
van de Rector Magnificus, prof.dr. M. Rem,
voor een commissie aangewezen door het College
van Dekanen in het openbaar te verdedigen op
maandag 25 november 1996 om 16.00

door

Henricus Franciscus Maria van den Bosch

geboren te Gassel

Dit proefschrift is goedgekeurd door de promotoren:

prof.dr.ir. P.J.A.M. Kerkhof

prof.dr.ir. A.K. Chesters

en de copromotor:

dr.ir. K.J. Ptasinski.

Druk: universiteitsdrukkerij
T.U.Eindhoven

ISBN: 90-386-0179-4

aan mijn ouders,
aan Jopie

Dankwoord

Alle mensen die op een of andere manier bijgedragen hebben aan dit proefschrift wil ik bedanken. Ik wil met name mijn promotor Piet Kerkhof bedanken voor het in mij gestelde vertrouwen en de prettige ongedwongen sfeer tijdens de gehele promotieduur. Vervolgens wil ik mijn copromotor Krzysztof Ptasinski bedanken voor de meer dan prettige samenwerking en voor het corrigeren van mijn schrijfwerk. Voor dit laatste wil ik zeker ook Anniek van Bemmelen bedanken. Daarnaast ben ik dank verschuldigd aan Leen Meerman, die als afstudeerder een zeer belangrijke bijdrage aan dit proefschrift geleverd heeft. De medewerkers van de werkplaats, Toon verstappen, Piet van Eeten, Frans van der Krieken en Chris Luyck wil ik bedanken voor de prettige samenwerking bij de bouw van mijn meetopstelling, met name Frans wil ik bedanken voor het vervaardigen van de meetcel. Ik bedank Peter Montfoorts voor het kritisch vergelijken van twee opstellingen voor deeltjes-grootte-meting. Ton Staring wil ik bedanken voor de prettige samenwerking bij een ander onderzoek in de groep Externe Velden. Ik dank mijn kamergenoten Kees Koning, Erik Lahey, Frank Jeurissen, Gert-Jan Schoenmakers, Willem-Jan Okkerse en andere (ex-)collegae voor de koffie en alle discussies over onderwerpen van zeer uiteenlopende aard. Tenslotte wil ik mijn familie en vrienden bedanken voor hun onontbeerlijke morele steun.

Het in dit proefschrift beschreven onderzoek werd financieel gesteund door het SRTCA (Shell).

summary

The research presented in this thesis deals with several calculation methods, concerning electrostatic coalescence, i.e. the merging of two conducting drops in an insulating medium due to an electric field, light scattering, especially forward light scattering, and optical particle sizing. The final goal was measurement and calculation of the evolution of a drop size distribution during electrostatic coalescence.

The first chapter presents besides a short introduction to all considered calculation methods also a short overview of publications concerned with both a conducting and an insulating phase in an electric field, considering emulsions as well as single drops.

Chapter 2 gives a general introduction for light scattering by spherical particles, especially for the geometric optics approximation.

In Chapter 3 expressions for the glory and edge contribution are derived from the exact Mie solution for scattering by spheres.

Chapter 4 gives minimal averaging requirements for the calculation of a scattering matrix with a specified accuracy. In a very dilute dispersion a scattering matrix \mathbf{A} provides a linear relation $\mathbf{A}\mathbf{x}=\mathbf{b}$ between a discrete scattering pattern \mathbf{b} and a discrete size distribution \mathbf{x} . Calculation times for scattering matrices are given using both the exact Mie solution and the geometric optics approximation.

Chapter 5 presents an experimental method for determining drop size distributions during electrostatic coalescence, and a method to account for multiple scattering in the calculation of a size distribution, i.e. if the above mentioned relation is no longer valid. A resulting measured evolution of the size distribution during electrostatic coalescence is presented.

In Chapter 6 the electrostatics of two conducting spheres in a parallel electric field are treated by an image method using both charge and dipole images.

In Chapter 7 relative trajectories are calculated for two spherical neutral drops due to gravity, an applied electric field, the van der Waals interaction, and hydrodynamic interaction. All interactions are assumed to be unretarded. The relative trajectories lead to collision efficiencies and collision rates. A model is presented to predict the change of a given size distribution, based on gravity induced settling of the drops, and electric field dependent collision cross sections for all pairs of drops. The resulting height-dependent evolution of an initially homogeneous size distribution is compared to an experimentally determined evolution. Because only binary interactions are considered, this model is only valid for dilute dispersions.

In Chapter 8 the most important conclusions are summarized and some remaining discrepancies are discussed.

samenvatting

Het onderzoek zoals beschreven in dit proefschrift behandelt een aantal rekenmethoden betreffende elektrostatistische coalescentie, d.w.z. het samenvloeien van twee geleidende druppels in een niet geleidend medium onder invloed van een elektrisch veld, lichtverstrooiing, in het bijzonder voorwaartse lichtverstrooiing, en optische deeltjes-grootte-meting. Het uiteindelijke doel was meting en berekening van de verandering van de druppelgrootte-verdeling tijdens elektrostatistische coalescentie.

Het eerste hoofdstuk geeft naast een korte introductie voor alle beschouwde rekenmethoden ook een kort overzicht van publicaties over een geleidende en een isolerende fase samen in een elektrisch veld, waarbij zowel emulsies als enkele druppels beschouwd worden.

Hoofdstuk 2 geeft een algemene inleiding voor lichtverstrooiing door bolvormige deeltjes, in het bijzonder voor de geometrische optica benadering.

In hoofdstuk 3 worden uitdrukkingen voor de "glory" en randbijdragen afgeleid van de exact Mie oplossing voor verstrooiing door bollen.

Hoofdstuk 4 geeft minimale middelingseisen voor de berekening van een verstrooiingsmatrix met een bepaalde nauwkeurigheid. In een zeer verdunde emulsie geeft een verstrooiingsmatrix A een lineaire relatie $Ax=b$ tussen een discreet verstrooiingspatroon b en een discrete deeltjes-grootte-verdeling x . Berekeningstijden voor een verstrooiingsmatrix worden gegeven waarbij zowel de exacte Mie oplossing als de geometrische optica benadering gebruikt is.

Hoofdstuk 5 beschrijft een experimentele methode om druppel-grootte-verdelingen tijdens elektrostatistische coalescentie te bepalen, en een methode om rekening te houden met meervoudige verstrooiing bij de berekening van een druppel-grootte-verdeling, als vergelijking $Ax=b$ niet meer geldt. Een zo bepaald verloop van de druppel-grootte-verdeling tijdens elektrostatistische coalescentie wordt getoond.

In hoofdstuk 6 wordt de elektrostatistische situatie van twee geleidende bollen in een homogeen elektrisch veld behandeld met behulp van beelden van ladingen en dipolen.

In hoofdstuk 7 worden relative banen berekend voor twee bolvormige neutrale druppels, t.g.v. de zwaartekracht, een opgelegd elektrisch veld, de van der Waals interactie en hydrodynamische interactie. Aangenomen wordt dat alle interacties ongeretardeerd zijn. De relatieve banen leiden tot botsings-doorsneden en botsings-frequenties. Er wordt een model gepresenteerd om het verloop van de druppel-grootte-verdeling te voorspellen, gebaseerd op bezinkende druppels en elektrisch-veld-afhankelijke botsingsdoorsneden voor alle paren van druppels. Het resulterende verloop van een aanvankelijk homogene druppel-grootte-verdeling wordt vergeleken met een experimenteel bepaald verloop. Omdat alleen binaire interacties beschouwd worden, is dit model alleen bruikbaar voor dispersies met een lage druppel-dichtheid.

In hoofdstuk 8 zijn de belangrijkste conclusies samengevat en worden enkele overgebleven discrepanties behandeld.

contents

1. Introduction.	
1.1. Experimental electric coalescers.	1
1.2. Single conducting drops.	2
1.3. Coalescence of two drops.	2
1.4. Objectives	3
1.5. Microscoping video recordings.	3
1.6. Forward light scattering	3
1.7. Theoretical model	4
1.8. Thesis overview	4
<i>references</i>	5
2. Forward light scattering	
2.1. Introduction	11
2.2. Amplitude function	11
2.3. Mie theory	12
2.4. Rayleigh scattering - small particles	13
2.5. Fraunhofer diffraction	14
2.6. Geometrical optics (GO)	17
2.7. Phase relations	22
2.8. Exceptional rays	23
2.9. Extinction	26
2.10. Complex angular momentum (CAM) theory	27
2.11. Conclusion	28
<i>references.</i>	28
3. Edge contribution to forward scattering	
3.1. Introduction	29
3.2. Asymptotic approximation	30
3.3. Glory rays	33
3.4. Edge functions	34
3.5. Absorbing sphere	36
3.6. Transparent sphere	37
3.7. Comparison with CAM extinction efficiency	39
3.8. Summary	40
<i>references.</i>	41
4. Scattering matrix	
4.1. Introduction.	42
4.2. Calculation of scattering matrix.	42
4.3. Fraunhofer diffraction	44
4.4. Averaging requirements.	45
4.5. GO approximation.	48
4.6. Results.	50
<i>references</i>	51

5. Particle sizing.	
5.1. Introduction.	52
5.2. Experimental set-up	53
5.3. Single scattering inversion	56
5.4. Redistribution matrix	57
5.5. Iterative multiple forward scattering inversion	59
5.6. Results	62
5.7. Conclusion	64
Appendix	64
<i>references</i>	67
6. Two spheres in a parallel electric field	
6.1. Introduction.	68
6.2. Dipole image	69
6.3. Two spheres	70
6.4. One image position	72
6.5. Multiple image position	73
6.6. Image dipoles	73
6.7. Imposed electric potentials	74
6.8. Isolated spheres	75
6.9. Potentials	77
6.10. Sphere -sphere forces	77
6.11. Equal earthed contacting spheres	80
6.12. Conclusion	82
Appendix	83
<i>references</i>	83
7. Electrostatic coalescence	
7.1. Introduction.	84
7.2. Relative velocities	84
7.3. Trajectories	87
7.4. Collision cross sections	89
7.5. Height-dependent size distribution.	92
7.6. Results and discussion.	94
7.7. Conclusion	98
<i>Appendices: bispherical coordinates, Hamaker force</i>	99
<i>references</i>	101
8. Conclusions	
8.1. Forward light scattering	102
8.2. Electrostatic coalescence.	103
List of symbols	104

Chapter 1. Introduction.

Electrostatic coalescence is important for separations of water-in-oil type (w/o) emulsions, but also for raindrop growth in clouds during thunder storms. An electric field polarizes the drops of a conducting dispersed phase in an insulating continuous phase. Two polarized drops attract one another and may coalesce, i.e. merge into one larger drop. Charging of drops may also lead to faster coalescence and separation. Electrostatic coalescers have been applied in petrochemical industries for over fifty years for removal of water from crude oil, that in some cases is mixed with water for desalination. A complete fundamental understanding of all mechanisms contributing to the enhanced coalescence is still lacking. Several authors give a review of suggested mechanisms¹⁻³.

Light scattering measurements are frequently used to determine particle sizes. Differently sized particles have different scattering patterns and can thus be distinguished. Measurement of forward light scattering patterns of dilute dispersions is a widely used method for determining the sizes of the particles or drops in the dispersion. The forward scattering pattern of a particle is largely due to the Fraunhofer diffraction of the non-incident light and depends therefore mainly on the cross section of the particle and hardly on the material properties of the particle. For accurate size measurements the exact scattering patterns should be used.

1.1. Experimental electric coalescers.

Different types of experimental electric coalescers with different electrode configurations and different time dependencies for the applied electric field, i.e. a.c., d.c. and pulsed d.c. fields, have been presented during the last decades¹⁻³⁴. The effect of pulse frequency on the performance of an electric coalescer was subject of a few papers¹⁰⁻¹². Frequently used electrode configurations are two parallel plates or grids, of which the lower one often in the separated conducting phase, the upper one sometimes coated with a solid insulating layer or replaced by a glass tube or bulb filled with a saturated salt solution. These latter insulated electrodes are advantageous for an a.c. and pulsed d.c. field, because a chain of water drops connecting the electrodes only provides a local short cut and draws less current than such a chain between non-insulated electrodes, so a higher field is maintained^{7,27}. These experimental coalescers are often tested for high fractions (10%-50%) water and a typical electric field strength is 1kV/cm. A more complicated electrode geometry is for example a number of charged metal spheres moving in a d.c. field between two grid electrodes¹⁹. The performance of the

experimental coalescers is also defined in different ways. A few authors relate the performance to the evolution of the size distribution in the dispersion²⁸⁻³⁴.

1.2. Single conducting drops.

An electric field E also deforms single conducting drops³⁵⁻⁵⁴. For small deformations a spherical drop with radius a obtains a prolate shape with semi major axis a' parallel to the field, semi minor axis b in the plane normal to the field ($a^3 = a'b^2$) and eccentricity e , $e^2 = 1 - b^2/a'^2 = 3/2 \cdot \epsilon E^2 r / \gamma$ where ϵ is the dielectric permittivity of the continuous phase and γ is the surface tension³⁵. The experimental conditions considered in this work, $\epsilon E^2 < 2.3 \text{ Nm}^{-2}$, $r < 10^{-4} \text{ m}$, $\gamma = 0.05 \text{ Nm}^{-1}$ lead to the eccentricity $e^2 < 7 \cdot 10^{-3}$ and $a'/b < 1.004$, i.e. electrostatic deformation of single drops is for this work negligible. For larger deformations the resulting shape of the drop depends on the ratio of the dielectric permittivities and on the ratio of the electric conductivities of the two phases. Conical points may be formed that eject small droplets or an elongated drop may fall apart in several drops, similar to the Rayleigh instability. An electric field may also be used to disperse large drops⁵⁵ or influence evaporation of fuel drops for combustion improvement⁵⁶.

If a conducting fluid is injected into an insulating fluid through a nozzle, the resulting drop size may be drastically reduced by a high voltage between the nozzle and another electrode⁵⁷⁻⁶⁷. The field therefore increases the surface area and enhances heat and mass transfer. Transfer to or from a single drop is also enhanced by shape oscillations and electrically induced circulation (Taylor flow) around and in a single drop⁶⁸⁻⁹¹. Several experimental electro-contactors have been presented that use these effects⁹²⁻⁹⁵.

1.3. Coalescence of two drops

Coalescence of two drops may be considered as a multi step process⁴. First two drops approach one another. Just before the drops touch, both their near contact areas will flatten or dimple and a thin film of the continuous phase is left between the drops. The size of the flattened area depends on the force that pushes the drops together. The same force also causes the film to drain slowly. If the film is thin enough it will rupture and the two drops merge, possibly leaving a daughter droplet behind. An electric field modifies all these separate steps. Chains of water drops are formed if the approach of two drops is faster than drainage and rupture of the remaining film. This situation arises if sufficient surfactants are present and is a commonly observed. Coalescence of a conducting drop at a flat liquid-liquid interface in an electric field has also been investigated⁹⁶⁻⁹⁸.

1.4. Objectives.

The initial objective of this study was a better fundamental understanding of electrostatic coalescence. This thesis, however, only considers the effect of an electric field on the first step of coalescence, i.e. the approach of two drops. The following steps are assumed to occur instantaneously. This was found to be correct for the considered experimental system. The theoretical model presented in this thesis leads eventually to the evolution of a given initial size distribution. The second objective was the verification of the theoretical model by measuring the evolution of the drop size distribution during electrostatic coalescence using forward light scattering.

1.5. Microscopic video recordings.

For the experimental work presented in this thesis a special cell has been built, consisting of two parallel plate electrodes and four transparent perspex walls, having a content of $1 \times 15 \times 40 \text{ mm}^3$. Microscopic video recordings of a 1 per cent water-in-kerosene emulsion in this cell show that in w/o emulsions without surfactants in a large enough electric field, only the initial approach of two drops in the size range 5-100 μm determines the collision rate and that the time required for the final approach, film drainage and film rupture is negligible. While the initial approach of two drops may be filmed using a standard 50Hz camera, two very close separate spherical drops require less than 1/50 second to coalesce into one larger spherical drop. Several occurrences of two coalescing drops (10-20 μm) were viewed frame by frame, but no intermediate situations were found. If surfactants are present, chain formation occurs, and switching off the electric field allows chained drops to separate again due to gravity. A very clear observation was due to a small hair of 200 μm from a cleaning tissue that remained in the cell. The hair touched one of the electrodes and caused an electrohydrodynamic flow, as if charge injected at the point of the hair into the kerosene was pushed away in the direction pointed to by the hair and the induced observable velocity was approximately 5mm/s.

1.6. Forward light scattering

The mentioned cell was initially built to measure the forward light scattering pattern of a water-in-kerosene emulsion during electrostatic coalescence. A parallel laser beam passing through a 1 promille water-in-kerosene emulsion in the cell is partially scattered by the water drops (Fig.7.1) and the forward scattering pattern of the emulsion is measured. The scattering patterns of spheres of different sizes are known and assuming incoherent scattering by different spheres allows calculation of the drop size distribution. If the scattered laser power is small relative to the undisturbed power then the measured

discrete scattering pattern \mathbf{b} is linearly related to the discrete size distribution \mathbf{x} by a scattering matrix: $\mathbf{Ax}=\mathbf{b}$. If scattered power in the emulsion is again significantly scattered, this linear relation is no longer valid and multiple scattering must be accounted for.

The size range considered in the presented experimental work allows exact calculation of the scattering patterns of spherical drops according to Mie¹⁰¹. In view of future work or other applications, attention was also given to the faster Geometrical Optics approximation¹⁰¹ that leads to accurate scattering patterns for very large spheres. It is shown that a separate expression for the contribution from the rays incident on the edge of the sphere to the forward scattering pattern, significantly improves this approximation, allowing faster calculation of scattering matrices.

1.7. Theoretical model

The theoretical model for electrostatic coalescence presented in this thesis considers the relative velocity of two spherical drops due to the combined effect of gravity, an applied electric field, unretarded van der Waals interaction and hydrodynamic interaction allowing for internal circulation. Inertial forces, Brownian motion, approach due to shear of the continuous phase, dimpling, electric deformation and surface tension gradients are not considered. The relative velocity of two drops leads to relative trajectories, collision efficiencies, collision rates, and the evolution of a given initial size distribution.

1.8. Thesis overview

In chapter 2 a general introduction to light scattering, especially the Geometric Optics approximation, will be given. Chapter 3 presents a method to derive values for edge functions that describe the edge contribution to forward scattering. In chapter 4 minimal averaging conditions are derived for the calculation of scattering matrices. In chapter 5 a method is presented for determining size distributions using forward light scattering measurements during electrostatic coalescence, and a measured evolution of the size distribution of water drops in kerosene is shown. Chapter 6 presents a method to calculate the electrostatic interaction between two spheres in an electric field. Chapter 7 describes the theoretical model for electrostatic coalescence in w/o emulsions with a small water fraction. Chapters 3 and 6 have been published^{99,100}. Chapters 5 and 7 are submitted for publication.

references

Reviews

1. Waterman, L.C., "Electrical coalescers", *Chem.Eng.Progress* **61**, 51 (1965).
2. Scott, T.C., "Use of electric fields in solvent extraction: a review and prospectus", *Sep. Purif. Methods*, **18**, 65 (1989).
3. Ptasinski, K.J. and Kerkhof, P.J.A.M., "Electric field driven separations: phenomena and applications", *Sep.Sci.Techn.* **27**, 995 (1992).
4. Chesters A.K., "The modelling of coalescence processes in fluid-fluid dispersions: A review of current understanding", *Trans IChemE*, **69A**, 259 (1991).

Experimental coalescers

5. Bailes, P.J. and Larkai, S.K.L., "An experimental investigation into the use of high voltage dc fields for liq.sep", *Trans.Icheme.* **59**,229 (1981).
6. Bailes, P.J. and Larkai, S.K.L., "Liquid phase separation in pulsed dc fields", *Trans.Icheme.* **60**,115 (1982).
7. Bailes, P.J. and Larkai, S.K.L., "The application of electric fields to phase separation in a solvent extraction system", *AIChE.Symp.Ser.* **238**,Vol.**80**,170 (1984).
8. Bailes, P.J. and Larkai, S.K.L., "Influence of phase ratio on electrostatic coalescence of water-in-oil dispersions", *Chem.Eng.Res.Des.* **62**,33 (1984).
9. Bailes, P.J. and Dowling, P.D., "The production of pulsed e.h.t. voltages for electrostatic coalescence", *J.Electrost.* **17**,321 (1985).
10. Joos, F.M. and Snaddon, R.W.L., "On the frequency dependence of electrically enhanced emulsion separation", *Chem.Eng.Res.Des.* **63**,305 (1985).
11. Bailes, P.J. and Larkai, S.K.L., "Electrical analysis of an electrostatic coalescer", *Chem.Eng.Res.Des.* **65**,445 (1987).
12. Snaddon, R.W.L. and Joos, F.M., "Electrostatically enhanced emulsion separation", *Chem.Eng.Res.Des.* **65**,448 (1987).
13. Fujinawa, Katsuhiko and Morishita, Mitsugu, "Demulsification of w/o emulsion by use of high voltage of ac fields", *J.Chem.Eng.Japan* **17**,6,632 (1984).
14. Goto, Masahiro and Irie, Jin, "Electrical demulsification of w/o emulsion by continuous tubular coalescer", *J.Chem.Eng.Japan* **22**,4,401 (1989).
15. Hano, Tadashi and Ohtake, Tkaaki, "Demulsification kinetics of w/o emulsion in an ac electric field", *J.Chem.Eng.Japan* **21**,4,345 (1988).
16. Kataoka, Takeshi and Nishiki, Tadaaki, "Development of a continuous el.coal.of w/o emulsion in liq.surf.membrane proc", *Sep.Sci.Techn.* **25**,171 (1990).
17. Lavrov, I.S. and Skachkov, A.E., "Influence of a nonuniform electric field on the behavior of emulsions and of model systems of nonpolar and weakly polar liquids", *Zh.Prik.Khim.* **50**,8,1802 (1977).

18. Sjoblom, G.L. and Goren, S.L., "Effect of dc electric fields on liquid-liquid settling", *I&Ec Fund.* **5**, 4, 519 (1966).
19. Skachkov, E.A. and Lavrov, I.S., "Electrodynamic treatment of reversed-type emulsions", *Zh.Prik.Khim.* **58**, 6, 1266 (1985).
20. Yamaguchi, M. and Kobayashi, A., "Continuous separation of an emulsion of water in oil by applying a dc el.field", *Int.Chem.Eng.* **27**, 3, 506 (1987).
21. Yamaguchi, Manabu and Sugaya, Hiroyuki, "Hydrodynamic behavior of disp.phase in a spray col.with an el.field for l-l ex", *J.Chem.Eng.Japan* **21**, 2, 179 (1988).
22. Yamaguchi, Manabu and Sugaya, Hiroyuki, "Liquid-liquid extraction characteristics of a spray column with a dc el.field", *J.Chem.Eng.Japan* **22**, 1, 25 (1989).
23. Yoshida, Fumiya and Yamaguchi, Manabu, "An exp.study of el.hyd.disp.from a liquid film flowing down an inclined plate", *J.Chem.Eng.Japan* **19**, 1, 1 (1986).
24. Yoshida, Fumiya and Yamaguchi, Manabu, "Continuous demulsification of o/w emulsion by m.of an inclined el.liq-liq cont.", *J.Chem.Eng.Japan* **21**, 4, 428 (1988).
25. Yoshida, Fumiya and Yamaguchi, Manabu, "Characteristics of el.disp.from water film flowing down an inclined plate", *J.Chem.Eng.Japan* **21**, 2, 123 (1988).
26. Hauertmann, H.B. and Degener, W., "Electrostatic coalescence: reactor, process control, and important parameters", *Sep.Sci.Tech.* **24**, 253 (1989).
27. Hsu, E.C. and Li, N.N., "Membrane recovery in liquid membrane separation processes", *Sep.Sci.Techn.* **20**, 115 (1985).

Drop size distributions

28. Sadek, E.S. and Hendricks, C.D., "Electrical coalescence of water droplets in low-conductivity oils", *Ind.Eng.Chem.Fundam.* **13**, 2, 139 (1974).
29. Hendricks, C.D. and Sadek, S., "Electric field enhanced coalescence of drops in liquid emulsions", *Ieee Trans.Ind.Appl.Ia-13*, 5, 489 (1977).
30. Sinaiskii, E.G., "Gravitational separation of disperse sys.with pre.aggr.of particles in an el.f", *Inz.Fiz.Zh.* **33**, 3, 412 (1977).
31. Williams, T.J. and Bailay, A.G., "Changes in the size distribution of a w/o emulsion due to el.f.induced coalesce", *Ieee Tran.Ind.Appl.Ia-22*, 3, 536 (1986).
32. Afanas'Ev, A.A. and Protod'Yakov, I.O., "Drop size distribution in an electrocontact extractor", *Zh.Prik.Khim.* **57**, 12, 2701 (1984).
33. Burkitbaev, E.M. and Kotoyants, K.V., "Water droplet coagulation during electrical dehydration of petroleum", *Inz.Fiz.Zh.* **53**, 4, 1137 (1987).
34. Scott, T.C. and Sisson, W.G., "Droplet size characteristics and energy input req.of em.formed in pulsed el.f.", *Sep.Sci.Tech.* **23**, 1541 (1988).

Dropshape

35. O'Konski, C.T. and Thacher, H.C.Jr., "The distortion of aerosol droplets by an electric field", *J.Phys.Chem.* **57**, 955 (1953).
36. O'Konski, C.T. and Harris, F.E., "Electric free energy and the deformation of droplets in electrically cond. sys.", *J.Phys.Chem.* **61**, 1172 (1957).
37. Kao, K.C., "Some electromechanical effects on dielectrics", *Brit.J.Appl.Phys.* **12**, 629 (1961).
38. Garton, C.G. and Krasucki, Z., "Bubbles in insulating liquid: stability in an electric field", *Proc.Roy.Soc.A* **280**, 211 (1964).
39. Taylor, Sir G.F.R.S., "Disintegration of waterdrops in an electric field", *Proc.Roy.Soc.A* **280**, 383 (1964).
40. Rosenkilde, C.E., "A dielectric fluid drop in an electric field", *Proc.Roy.Soc.A* **312**, 473 (1969).
41. Brazier-Smith P.R., "Stability and shape of isolated and pairs of water drops in an electric field", *Phys.Fluids* **14**, 1, 1 (1971).
42. Torza S. and Cox R.G., "Electrohydrodynamic deformation and burst of liquid drops", *Phil.Tran.Roy.Soc.Lon.A* **269**, 295 (1971).
43. El Sawi M., "Distorted gas bubbles at large reynolds number", *J.Fluid Mech.* **62**, 1, 163 (1974).
44. Vanden-Broek J.M. and Keller J.B., "Deformation of a bubble or a drop in a uniform flow", *J.Fluid Mech.* **101**, 4, 673 (1980).
45. Miksis, M. and Vandenbroek, J.M., "Axisymmetric bubble or drop in a uniform flow", *J.Fluid Mech.* **108**, 89 (1981).
46. Miksis, M.J., "Shape of a drop in an electric field", *Phys.Fluids* **24**, 11, 1967 (1981).
47. Eicke, H.F., "The distortion of electr. conducting, thermodyn. stable microphases by an el.f.", *Helv.Chim.Acta* **66**, 5, 1569 (1983).
48. Moriya, Satoru and Adachi, Keiichiro, "Deformation of droplets suspended in visc. media in an elec. field. rate of d.", *Langmuir* **2**, 155 (1986).
49. Vu N. and Carleson T.E., "Electric field effects on drop size and terminal velocity in liquid-liquid syst.", *AIChE.J.* **32**, 10, 1739 (1986).
50. Perona, J.J. and Byers, C.H., "Electrostatic forces on conducting fluid spheroids in a parallel field", *Chem.Eng.Sci.* **42**, 11, 2785 (1987).
51. Calero, J.F. and Chato, J.C., "The electrohydrostatics of a conductive liquid meniscus", *Ieee*, 88 Ch 2565-0/88/0000-1547 (1988).
52. Nishiwaki, Tsuyoshi and Adachi, Keiichiro, "Deformation of viscous droplets in an electric field", *Langmuir* **4**, 170 (1988).
53. Basaran, O.A. and Scriven, L.E., "Axisymmetric shapes of isolated charged drops", *Phys.Fluids A* **1**, 5, 795 (1989).

54. Basaran, O.A. and Scriven, L.E., "Axisymmetric shapes of charged drops in an external electric field", *Phys. Fluids A* **1**, 5, 799 (1989).

Droprupture

55. Scott, T.C., "Surface area generation and droplet size control using pulsed electric fields", *AIChE J.* **33**, 9, 1557 (1987).
56. Harstad, K. and Bellan, J., "Electrostatic dispersion of drops in clusters", *Combust. Sci. Techn.* **63**, 169 (1989).

Drop formation

57. Borzabadi E. and Bailey A.G., "The profiles of axially symmetric electrified pendant drops", *J. Electrostatics* **5**, 369 (1978).
58. Byers C.H. and Perona J.J., "Drop formation from an orifice in an electric field", *AIChE J.* **34**, 9, 1577 (1988).
59. Hibiki, T. and Yamaguchi, M., "Formation of single charged droplets from a laminar liquid jet in a uniform el.f.", *Int. Chem. Eng.* **30**, 2, 300 (1990).
60. Kim H.S. and Kim W.S., "The mechanism of droplet formation and prediction of the droplet size in l-l sys", *Intern. Chem. Eng.* **30**, 1, 169 (1990).
61. Morimoto Y., "Electrification of a water drop in an electric field", *Japan. J. Appl. Phys.* **14**, 10, 1595 (1975).
62. Takamatsu T. and Hashimoto Y., "Theoretical and experimental studies of charged drop formation in a unif. el.f.", *J. Chem. Eng. Japan* **14**, 3, 178 (1981).
63. Takamatsu T. and Yamaguchi M., "Formation of single charged drops in liquid media under a uniform electric field", *J. Chem. Eng. Japan* **15**, 5, 349 (1982).
64. Takamatsu T. and Yamaguchi M., "Formation of single charged drops in a non-uniform electric field", *J. Chem. Eng. Japan* **16**, 4, 267 (1983).
65. Tamano K., "Measurement of the size distr. of drops by an electric charge. effect at drop formation", *Intern. Chem. Eng.* **26**, 4, 698 (1986).
66. Tsukada T. and Sato M., "Static drop formation in an electrostatic field", *J. Chem. Eng. Japan* **19**, 6, 537 (1986).
67. Bailes P.J., "Solvent extraction in an electrostatic field", *Ind. Eng. Chem. Proc. D.D.* **20**, 564 (1981).

Single drop circulation and vibration

68. Taylor G.F.R.S. and McEwan A.D., "The circulation produced in a drop by an electric field", *Proc. Roy. Soc. A*, **291**, 159 (1965).
69. Bailes P.J. and Thornton J.D., "Electrically augmented liquid-liquid extraction in a two-component system", *Proc. Int. Solvent Extr. Conf.* **2**, 1431 (1971).

70. Morrison, F.A. Jr., "Transient heat and mass transfer to a drop in an el.f.", *J.Heat Transfer* **099**, 269 (1977).
71. Griffiths, S.K. and Morrison, F.A. Jr., "Low peclet number heat and mass transfer from adrop in an electric field", *J.Heat Transfer* **101**, 484 (1979).
72. Kaji, N. and Mori, Y.H., "Augmentation of direct-contact heat transfer to drops with an intermittent electric field.", *J.Heat Transfer* **102**, 32 (1980).
73. Chang, L.S. and Carleson, T.E., "Heat and mass transfer to translating drop in an electric field", *Int.J.Heat Mass Tr.* **25**, 7, 1023 (1982).
74. Takamatsu, T. and Yamaguchi, M., "Terminal velocity of single charged drops through diel.liq.in a uniform el.f.", *Chem.Eng.Japan* **16**, 4, 324 (1983).
75. Griffiths, S.K. and Morrison, F.A. Jr., "The transport from a drop in an alternating electric field", *Int.J.Heat Mass Tr.* **26**, 5, 717 (1983).
76. Griffiths, S.K. and Morrison, F.A. Jr., "The fluid motion and transport in and about an assemblage of drops in an el.f.", *J.Coll.Int.Sci.* **94**, 2, 514 (1983).
77. Chang, L.S. and Berg, J.C., "Fluid flow and tranferbehaviour of a drop translating in an electric field at intermediate Reynolds numbers", *Int.J.Heat Mass Tr.* **26**, 6, 823 (1983).
78. Carleson, T.E. and Berg, J.C., "Marangoni and electrical field effects upon mass transfer to translating drops", *Chem.Eng.Comm.* **25**, 117 (1984).
79. Chang, L.S. and Berg, J.C., "Electroconvective enhancement of mass or heat exc.in the pres.of interf.t.grad", *AIChE.J.* **31**, 1, 149 (1985).
80. Chang, L.S. and Berg, J.C., "The effect of interfacial tension gradients on the flowstruc.of drops in an el.", *AIChE.J.* **31**, 4, 551 (1985).
81. Cheng, K.J., "Capillary oscilations of a drop in an electric field", *Phys.Lett.* **112A**, **8**, 392 (1985).
82. Yamaguchi M. and Takamatsu T., "An experimental study of mass transfer rate in disp.phase for single drops el.f", *J.Chem.Eng.Japan* **18**, 4, 325 (1985).
83. Carleson, T.E. and Fuller, E., "The effects of electrical charge upon mass from drops exhibiting interf.turbul.", *Chem.Eng. Comm.* **57**, 277 (1987).
84. Mochizuki, T. and Mori, Y.H., "Augmenation of direct-contact heat transfer to a train of drops by app.of el.f", *J.Chem.Eng.Japan* **20**, 6, 609 (1987).
85. Scott, T.C., "Visualization of flow fields and interfacial phenomena in l-l solvent extraction", *Sep.Sci.Techn.* **22**, 503 (1987).
86. Wham, R.M. and Byers, C.H., "Mass transport from single droplets in imposed electric fields", *Sep.Sci.Techn.* **22**, 447 (1987).
87. Scott, T.C. and Byers, C.H., "A model for mass transfer in oscilating-circulating liquid drops", *Chem.Eng.Comm.* **77**, 67 (1988).

88. De Kee, D. and Chhabra, R.P., "A photographic study of shapes of bubbles and coal in non newtonian polymer sol", *Rheol. Acta* **27**, 656 (1988).
89. Kaji, N. and Mori, Y.H., "Electrically induced shape oscillation of drops as means of heat tr.enh:dropdyn", *J.Heat Transfer* **110**, 695 (1988).
90. Kaji, N. and Mori, Y.H., "Electrically induced shape oscillation of drops as means of heat tr.enh:heat tr.", *J.Heat Transfer* **110**, 700 (1988).
91. Scott, T.C. and Basaran, O.A., "Characteristics of electric-field-induced oscillations of translating liq.drops", *Ind.Eng.Chem.Res.* **29**, 901 (1990).

Electric field contactors

92. Kowalski, W. and Ziolkowski, Z., "Increase in rate of mass transfer in extraction columns by means of an el.field", *Int.Chem.Eng.* **21**, 2, 323 (1981).
93. Martin, L. and Vignet, P., "Electrical field contactor for solvent extraction", *Sep.Sci.Techn.* **18**, 1455 (1983).
94. Bailes, P.J. and Stitt, E.H., "Column liquid contacting with vigorous agitation balanced by electrostatic coalescence.", *Chem.Eng.Res.Des.* **65**, 514 (1987).
95. Scott, T.C. and Wham, R.M., "An electrically driven multistage countercurrent solvent extraction device.", *Ind.Chem.Res.* **28**, 94 (1989).

Film drainage

96. Allan, R.S. and Mason, S.G., "Effect of electric fields on coalescence in liquid+liquid systems", *Trans.Far.Soc.* **57**, 2027 (1961).
97. Brown, A.H. and Hanson, C., "Effect of oscillating electric fields on coalescence in liquid-liquid systems", *Trans.Far.Soc.* **61**, 1754 (1964).
98. Brown, A.H. and Hanson, C., "The effect of oscillating electric fields on the coalescence of liquid drops", *Chem.Eng.Sci.* **23**, 841 (1968).

Other

99. H.F.M. van den Bosch, P.J.A.M. Kerkhof and K.J. Ptasinski, "Edge contribution to forward scattering by spheres", *Appl.Opt.* **35**, 2285 (1996).
100. H.F.M. van den Bosch, P.J.A.M. Kerkhof and K.J. Ptasinski, "Two conducting spheres in a parallel electric field", *J. of Appl. Phys.* **78**, 6345 (1995).
101. H. C. van de Hulst, *Light Scattering by Small Particles*, Wiley New York (1957)

Chapter 2. Forward light scattering

2.1. Introduction

Particle sizes can be measured using the particles scattering properties. Differently sized particles have different scattering patterns and can thus be distinguished. In this chapter commonly known calculation methods for calculating scattering patterns are discussed. This is merely done as introduction for the next chapters where calculation methods are presented for the edge contribution to forward scattering by spheres and for scattering matrices, that linearly relate discrete scattering patterns and discrete size distributions.

2.2. Amplitude function

Consider a spherical particle in a plane electromagnetic wave with incident electric field amplitude

$$E_i(z) = E_0 \cdot e^{i(kz - \omega t)}, \quad (2.1)$$

wave number $k = \omega / c$. The wave scattered by the particle located at position z is a spherical outgoing wave. Its intensity at large distance is therefore proportional to the inverse of the squared distance r from the particle: $I \sim r^{-2}$. The amplitude ($\sim \sqrt{I}$) may therefore be written as

$$E_s(r, \vartheta, \varphi) = E_0 \cdot S(\vartheta, \varphi) \cdot \frac{e^{i(kr - \omega t)}}{ikr} \quad (2.2)$$

defining the dimensionless complex amplitude function $S(\vartheta, \varphi)$. The coordinate ϑ gives the angle between the direction of the incident and scattered wave, while φ gives the azimuth angle (Fig.2.1). The reason for the factor $i = \sqrt{-1}$ in the denominator in this definition will be explained in section 4.

Assume a plane wave incident on the sphere polarized with the electric field parallel to the plane of the drawing (Fig.2.2). Symmetry considerations lead to a scattered wave that is in the plane of the drawing ($\varphi = \pi/2$) and in the perpendicular plane ($\varphi = 0$) also polarized with electric field parallel to the plane of the drawing, while for other azimuth angles ($0 < \varphi < \pi/2$) the scattered wave may have a deviating polarization. The complex amplitude functions S_1 and S_2 in the scattering planes for $\varphi = 0$ and $\varphi = \pi/2$ may be different and are defined by combining Eqs.2.1 and 2.2 as

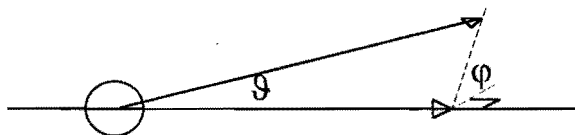


Figure 2.1. Definition of angles ϑ and φ .

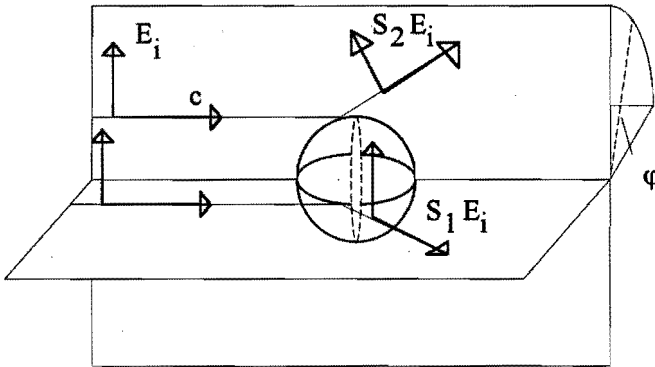


Figure 2.2. Linear polarized light is after scattering by a sphere still linearly polarized in two perpendicular planes.

$$E_s(r, \vartheta, 0) = E_i \cdot S_1(\vartheta) \cdot \frac{e^{i(kr - kz)}}{ikr} \quad (2.3)$$

$$E_s\left(r, \vartheta, \frac{\pi}{2}\right) = E_i \cdot S_2(\vartheta) \cdot \frac{e^{i(kr - kz)}}{ikr}. \quad (2.4)$$

With respect to an arbitrary scattering plane the electric field of a general incident wave consists of a normal (polarization 1) and a parallel (polarization 2) component, leading to a corresponding normal and a parallel component of the scattered wave.

If the incident wave with intensity I_0 is unpolarized or exactly circular polarized, then the intensity distribution for any azimuth angle ϕ is the average of the intensity distributions from both scattering amplitude functions;

$$I(\vartheta) = \frac{i \cdot I_0}{k^2 r^2}, \quad i = \frac{i_1 + i_2}{2}, \quad i_j = |S_j|^2 \quad (2.5)$$

where $j = 1, 2$. The amplitude function S_j and the intensity functions i_j and i are dimensionless and describe scattering for large r .

2.3. Mie theory

Mie gave an exact solution for the scattering of a plane electromagnetic wave by a sphere of arbitrary size and arbitrary refractive index. A full description of the theory is given by van de Hulst¹ and also Bohren and Huffman². The latter also give a computer algorithm that is used in this work to calculate exact scattering patterns.

The complete scattering pattern of a spherical homogeneous particle depends on two parameters: the relative refractive index $m = n_2 / n_1$ and the size parameter x . The refractive index n_1 of the medium is assumed to be a real number, the refractive index n_2 of the particle may be a complex number $n_2^2 = \epsilon_2 = \epsilon_r \epsilon_0 - 4\pi i \sigma / \omega$, where ϵ_r is the

relative dielectric permittivity, ϵ_0 is the vacuum dielectric permittivity, σ is the particle conductivity and $\omega/(2\pi)$ is the frequency. An imaginary component of the refractive index corresponds with absorption of light, due to the conductivity σ of the medium. The size parameter $x = ka = 2\pi a / \lambda$, with external wave number k and particle radius a , gives the ratio of the circumference of the particle and the external wavelength λ .

A plane electromagnetic wave is the simplest solution of the Maxwell equations in orthogonal coordinates (x,y,z) . For the Maxwell equations in spherical coordinates (r,ϑ,φ) the same plane wave is an infinite summation of elementary solutions with known coefficients. Besides the external incident wave, there is also an internal wave and an external scattered wave with coefficients determined by the boundary conditions at the sphere surface.

The number of elementary solutions, required for an accurate solution, depends on the size parameter, approximately as $x+4x^{1/3}+2$. A faster approximate method that may be used for large values of the size parameter x is the ray optics or geometrical optics (GO) approximation as discussed in section 2.6. The concept 'light ray' is only useful if at least a width of the order of the wave length at an interface is refracted to approximately the same direction, requiring $a \gg \lambda$, i.e. $x \gg 10$.

2.4. Rayleigh scattering - small particles

If a particle with an isotropic complex dielectric permittivity ϵ_2 in a medium with dielectric permittivity ϵ_1 is very small compared to the wavelength of the incident wave

$$x \ll 1 \quad (2.6)$$

and also compared to the wavelength inside the particle

$$x \cdot |m| \ll 1 \quad (2.7)$$

where $m^2 = \epsilon_2 / \epsilon_1$, then the particle becomes a radiating dipole with dipole moment $\mathbf{p} = \alpha_p \cdot \mathbf{E}_i$ parallel to the electric field of the incident wave, where the polarizability

$$\alpha_p = \frac{\epsilon_2 - \epsilon_1}{\epsilon_2 + 2\epsilon_1} \cdot a^3$$

is proportional to the volume of the particle. Dipole radiation in the plane normal to the dipole ($\varphi=0$) is independent of the angle ϑ , and in the plane of the dipole ($\varphi=\pi/2$) proportional to $\cos\vartheta$. The complex amplitude functions are given by¹

$$\left. \begin{array}{l} S_1(\vartheta) \\ S_2(\vartheta) \end{array} \right\} = i \cdot \alpha_p \cdot k^3 \left\{ \begin{array}{l} 1 \\ \cos\vartheta \end{array} \right. \quad (2.8)$$

If only the first condition (Eq.2.6) is fulfilled then the particle becomes a radiating multipole, leading to resonance peaks as just can be seen for $m=1.33$ in Fig.2.3. For

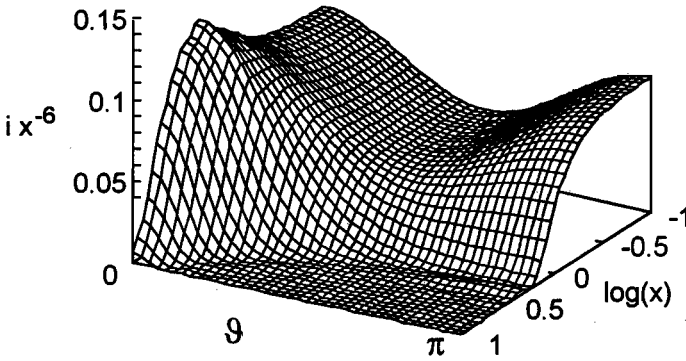


Figure 2.3. Exact intensity function $i x^{-6}$ according to Mie as function of scattering angle $0 < \vartheta < \pi$ and size parameter x for $m=1.33$, showing the change from Rayleigh scattering at $x=10^{-1}$ to forward directed scattering at $x=10$.

larger values of m resonance is more significant. The intensity function for unpolarized waves

$$i(\vartheta) = \left(\frac{m^2 - 1}{m^2 + 2} \right)^2 \cdot \frac{1 + \cos^2 \vartheta}{2} \cdot x^6 \tag{2.9}$$

depends therefore very strongly on the size parameter x . Rayleigh scattering is the limiting case of the exact solution for $x \rightarrow 0$ (Fig.2.3).

2.5. Fraunhofer diffraction

The total scattering pattern of a particle is assumed to consist of contributions due to incident rays that are reflected and refracted in different directions (Fig.2.7). An other contribution comes from the non incident rays that cause a specific angular intensity distribution called Fraunhofer diffraction through interference at large distance. Contrary to the Rayleigh theory, the Fraunhofer theory is not a limiting case of the exact solution, but is found by comparison to approach the exact forward scattering pattern for $x \rightarrow \infty$.

Huygens assumed a wave front to consist of an infinite number of coherent sources all contributing to a new wave front in forward direction. Fresnel formulated a quantitative relation for this principle by an integration over the first wave front

$$E_s = \iint E_i \cdot \frac{1}{ir\lambda} \cdot e^{ikd} dA \tag{2.10}$$

where E_i and E_s are the amplitudes of both wave fronts, r is the distance between the wave fronts and d is the distance between area dA and point P on the wave fronts (Fig.2.4). This relation is valid for $kr \gg 1$.

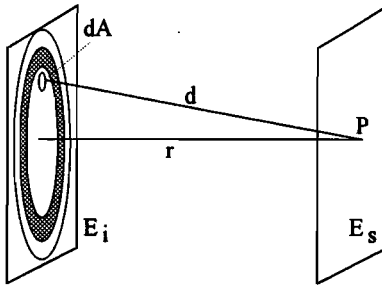


Figure 2.4. Fresnel zones in one wave front that contribute with alternating sign to a point of a next wave front.

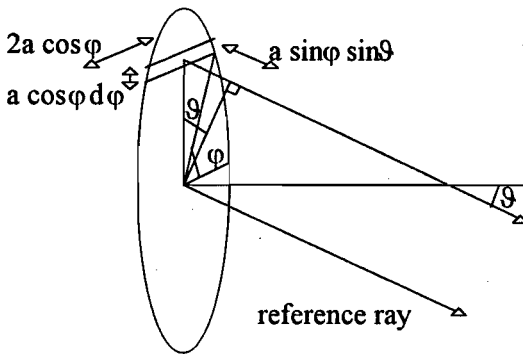


Figure 2.5. Small strip in circular wave front contributing to diffraction.

Integration of this expression over a large enough area ($\gg r\lambda$) results in the required relation for the amplitudes of two infinite wave fronts at a distance r from each other

$$E_s = E_i \cdot e^{ikr} \quad (2.11)$$

The factor $1/(r\lambda)$ in Eq.2.10 indicates that an area $r\lambda$ of the primary wave front effectively contributes to the amplitude in a point of the second wave front. The factor i indicates that the average distance between this area and the considered point in the second front is a quarter wave length longer than the (shortest) distance r ($d_{av}=r+\lambda/4$).

A partially blocked infinite wave front may be constructed by adding a small wave front with opposite amplitude. An infinite wave front has no scattering pattern. The intensity function $i_{Frb} = |S_{Frb}|^2$ of an infinite wave front blocked by a small particle is therefore equal to the intensity function of a corresponding small hole in an infinite screen (Babinet's principle). Assume a plane electromagnetic wave illuminating a screen at $z = 0$ with a circular opening with radius a and size parameter $x=ka \gg 1$ (Fig.2.5). The integration according to Eq.2.10 is then limited to the circular opening. The area of an infinitesimal strip is given by $dA = 2a \cos\phi \cdot a \cos\phi d\phi$. The total amplitude in a point far away ($r \rightarrow \infty$) in direction θ is found by integration according to Eq.2.10 with d also

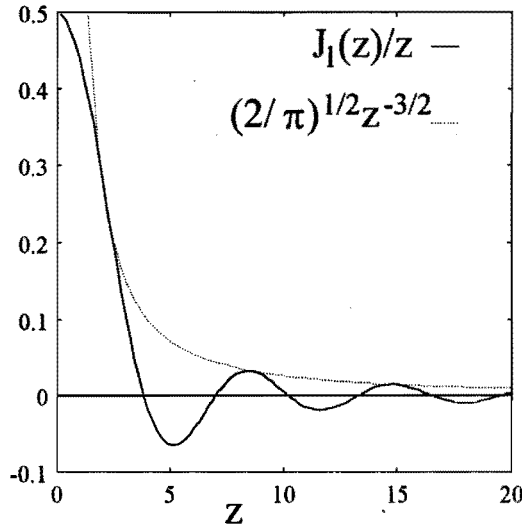


Figure 2.6. Fraunhofer amplitude function $S_{\text{Frh}}(x, \vartheta) / x^2 = J_1(z) / z$ with $z = x\vartheta$, ϑ in radians, and its envelope function $(2/\pi)^{1/2} z^{-3/2}$ that is valid for large z .

depending on the direction ϑ . The resulting amplitude does not depend on the polarization of the incident wave.

$$E_s(r, \vartheta) = \int_{-\pi/2}^{\pi/2} \frac{E_i}{ir\lambda} e^{ik(r-a\sin\varphi\sin\vartheta)} 2a^2 \cos^2\varphi d\varphi \quad (2.12)$$

Equation 2.12 leads with Eqs.2.3 or 2.4 and $z = x \cdot \sin\vartheta \approx x \cdot \vartheta$ to the real, i.e. not complex, Fraunhofer amplitude function

$$S_{\text{Frh}}(x, \vartheta) = \frac{x^2}{\pi} \int_{-\pi/2}^{\pi/2} e^{iz\sin\varphi} \cos^2\varphi d\varphi = x^2 \frac{J_1(z)}{z} \quad (2.13)$$

with J_1 the integer Bessel function of the first kind. The function $J_1(z)/z$ is shown in Fig.2.6. The amplitude function for the Fraunhofer diffraction is the same for both polarizations. The amplitude function is maximal for $\vartheta=0$, $S_{\text{Frh}}(x,0)=x^2/2$, and has its first minimum at $\vartheta=3.83/x$. The width of the main lobe is thus proportional to the inverse of the size parameter x .

Equation 2.13 also follows from the Helmholtz-Kirchhoff relation³ for scalar waves, stating that the field at any point P can be expressed by an integral of the field over a surrounding surface. A direction factor should then be included, leading to an extra factor $(1+\cos\vartheta)/2$ in Eq.2.13 that is only relevant for large angles.

The size parameter of a typical laser beam used in forward light scattering measurements, i.e. the ratio of beam width and wavelength, is of the order of 10^5 , and spreading of the undisturbed laser beam is limited to very small angles.

A particle in a laser beam scatters a part of the wave front by reflection and refraction, and leaves an incomplete wave front (Fig.2.7). The new wave front may be represented by a large wave front with negative amplitude, with a small circular wave front with positive amplitude added to it. Both circular wave fronts contribute to the resulting diffraction pattern with the amplitude function given in Eq.2.13, with different values for x and opposite sign. If more particles are located at random positions in the laser beam, then the far field diffraction amplitude from the large wave front is for the angle $\vartheta=0$ slightly diminished by the opposite smaller wave fronts. The large angle scattering is mainly determined by the particles, provided enough particles are present. The number of particles N_p for a particular particle size parameter x_p , leading to the same large angle scattering as the "laser beam", may be deduced by equating the envelope function (Fig.2.6) for the Fraunhofer diffraction intensity ($i_{Fth} = S_{Fth}^2$) for both beam and particles and is found to be $N_p = x_b/x_p$, where x_b is the size parameter for the laser beam, x_p is the particle size parameter and N_p gives the minimum number of particles required for particle sizing using forward scattering.

Although Fraunhofer diffraction describes only half of the intensity scattered by a particle, it is for values of $x > 10$ the major contribution in the forward direction and may be considered as the basis for particle sizing using forward light scattering. Small particles have a wide scattering pattern, while large particle have a narrow scattering pattern.

2.6. Geometrical optics (GO)

The part of the wave front incident on the particle is spread over a much wider angle range than the Fraunhofer diffraction. Its contribution in the exact forward direction ($\vartheta=0$) is smaller than the Fraunhofer contribution.

Part of a light ray that hits a sphere is directly reflected and a part is refracted into the sphere. The ray inside the sphere will keep reflecting against the surface, and at every reflection a part refracts to the outside. The deduction by Van de Hulst¹ is extended with the generalized Snell's law allowing complex reflection- and transmission coefficients.

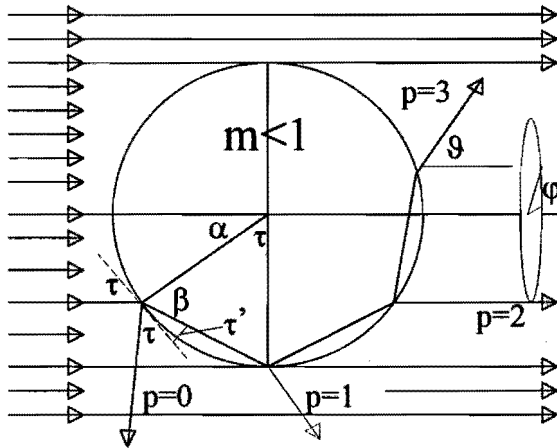


Figure 2.7. Separation of wave front in incident and non-incident rays for a sphere with $m < 1$. The non incident rays cause a Fraunhofer diffraction contribution. The rays that hit the sphere are partly reflected and partly refracted. Four outgoing rays are denoted by $p=0,1,2,3$.

A finite light ray from a plane wave with intensity I_0 is determined by $d\alpha$ and $d\phi$ and contains a flux of energy given by

$$I_0 a^2 \sin\alpha \cos\alpha d\alpha d\phi \quad (2.14)$$

This energy will be divided among all outgoing rays denoted by $p=0,1,2$ etc. (Fig.2.7).

The angle of refraction β of the inside ray is given by Snell's law:

$$\sin\beta = \frac{\sin\alpha}{m} \quad (2.15)$$

In this equation complex values are permitted for both m ($\text{Im}[m] > 0$) and β , the angle of incidence α is real.

The electric field amplitudes of reflected and transmitted wave at an interface are given by the Fresnel reflection and transmission coefficients.

$$r_1 = \frac{\cos\alpha - m \cdot \cos\beta}{\cos\alpha + m \cdot \cos\beta} \quad r_2 = \frac{m \cdot \cos\alpha - \cos\beta}{m \cdot \cos\alpha + \cos\beta} \quad (2.16)$$

The sign of these coefficients corresponds to the components of the electromagnetic wave perpendicular to the plane of incidence, i.e. the electric field for polarization 1 (Fig.2.2) and the magnetic field for polarization 2. The reflection of polarization 2 is sometimes defined with the opposite sign, referring to the component of the electric field parallel to the interface. The definition used here is more appropriate for calculating scattering amplitudes.

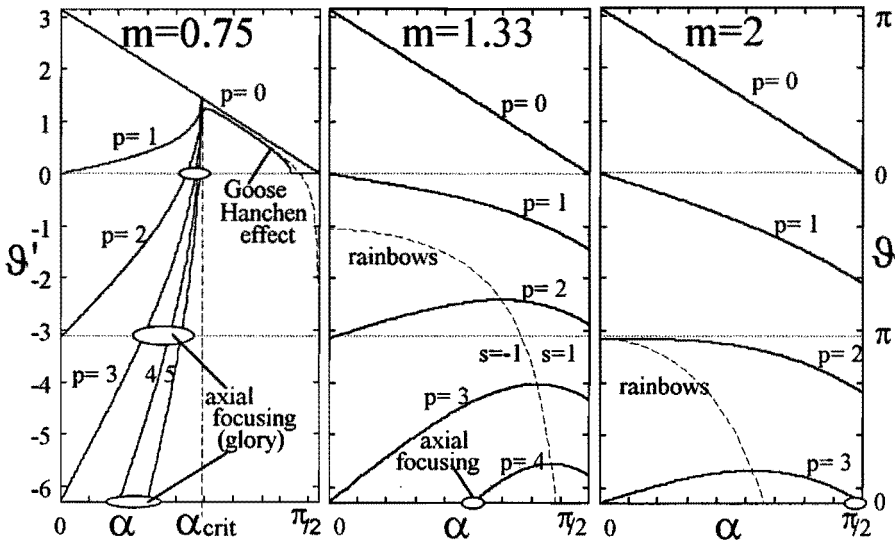


Figure 2.8. Scattering angle \mathcal{S}' for three values of the relative refractive index m and several outgoing rays denoted by p (Fig.2.7) as function of the angle of incidence α . Special angles are indicated. Van de Hulst¹ earlier presented the figure for $m=1.33$.

The above equations describe the reflection and transmission of the incident wave at the sphere surface. The ray that is transmitted into the sphere will again strike the surface, but from the other side with angle of incidence β , angle of refraction α and relative refractive $1/m$. The total amplitude transmission coefficient $\varepsilon_j(p)$ is given by $\varepsilon_j(0) = r_j$ while for $p \geq 1$

$$\varepsilon_j(p) = (1 - r_j^2)(-r_j)^{p-1} \tag{2.17}$$

The sum for all p of $|\varepsilon_j(p)|^2$, representing the relative energy fluxes, is equal to 1.

The total deviation \mathcal{S}' from the direction of the original ray for a leaving ray denoted by p is deduced from Fig.7,

$$\mathcal{S}'(\alpha, m, p) = (\pi - 2\alpha) - p \cdot (\pi - 2\beta_r) = 2(\tau - p\tau') \tag{2.18}$$

For real m the angle β is real. For complex m the real angle β_r is given by Petykiewicz³.

The scattering angle \mathcal{S} in the interval $(0, \pi)$ relates to this total scattering angle \mathcal{S}' by

$$\mathcal{S}' = -h \cdot 2\pi + q \cdot \mathcal{S} \tag{2.19}$$

where h is an integer and $q = +1$ or $q = -1$. In Fig.2.8 the total scattering angle \mathcal{S}' is shown as function of the angle of incidence α for three values of the relative refractive index: $m=3/4$, i.e. an air bubble in water, $m=4/3$, i.e. a water drop in air and $m=2$. A ray that hits a spherical particle at a specific angle of incidence α is divided over several rays p leaving the particle at different scattering angles \mathcal{S}' .

Figure 2.8 indicates how the functions $\mathfrak{S}'(\alpha, p)$ depend on the relative refractive index m . For central incidence ($\alpha=0$) the scattering angle does not depend on m : $\mathfrak{S}'(0, p) = (1-p)\pi$. The scattering angle for reflected rays is also independent of m : $\mathfrak{S}'(\alpha, 0) = \pi - 2\alpha$.

For $m < 1$ a critical angle of incidence α_{crit} exists, with $\sin \alpha_{\text{crit}} = m$, for which according to geometrical optics all leaving rays ($p=0, 1, \dots$) are coincident. For $\alpha > \alpha_{\text{crit}}$ all light is reflected. Three extreme cases may be deduced from Fig.2.8:

- for $m=0$ all functions $p \geq 1$ are vertical lines at $\alpha=0$ and only $p=0$ actually contributes to the scattering pattern
- for $m=1$ all functions $\mathfrak{S}'(\alpha, m, p)$ are lines passing through the point $\alpha=\pi/2$, $\mathfrak{S}'=0$. Both reflections coefficients for $m=1$ are equal to zero, and only $p=1$ contributes to the scattering pattern. The "rainbows" parabola touches the $p=1$ line.
- for $m=\infty$ all functions are lines parallel to the $p=0$ function. Only $p=0$ contributes to the scattering pattern.

The range $d\mathfrak{S}$ around the scattering angle \mathfrak{S} in which the incident ray with range $d\alpha$ is scattered is found by differentiating \mathfrak{S} using Snell's law, leading for real m to

$$d\mathfrak{S} = \left(2p \frac{\cos \alpha}{m \cdot \cos \beta} - 2 \right) d\alpha \quad (2.20)$$

For complex m the expression for the derivative $d\mathfrak{S}/d\alpha$ is not given here.

The energy flux of the incident ray (Eq.2.14), multiplied with the averaged squared moduli of the already calculated total transmission coefficients ε_1 or ε_2 , gives for a leaving ray the energy flux. This flux is at a large distance r spread over an area r^2 times the solid angle $|\sin \mathfrak{S} d\mathfrak{S} d\varphi|$. The intensity for polarization $j = 1, 2$ is given by

$$I_j(r, \mathfrak{S}, \varphi) = |\varepsilon_j|^2 \frac{a^2 \sin \alpha \cos \alpha d\alpha d\varphi}{r^2 |\sin \mathfrak{S} d\mathfrak{S} d\varphi|} \quad (2.21)$$

Using Eqs.2.5 and 2.21 and $ka=x$ the intensity function for both polarizations is written as

$$i_j = |S_j|^2 = x^2 |\varepsilon_j|^2 D \quad (2.22)$$

$$\text{with } D(\mathfrak{S}) = \left| \frac{\sin \alpha \cdot \cos \alpha}{\sin \mathfrak{S} (d\mathfrak{S} / d\alpha)} \right|, \quad D(0) = \frac{1}{(d\mathfrak{S} / d\alpha)^2} \quad (2.23)$$

The modulus of the complex amplitude function S_j for each ray is given by the root of i_j , the phase of the complex amplitude functions is calculated in the next section.

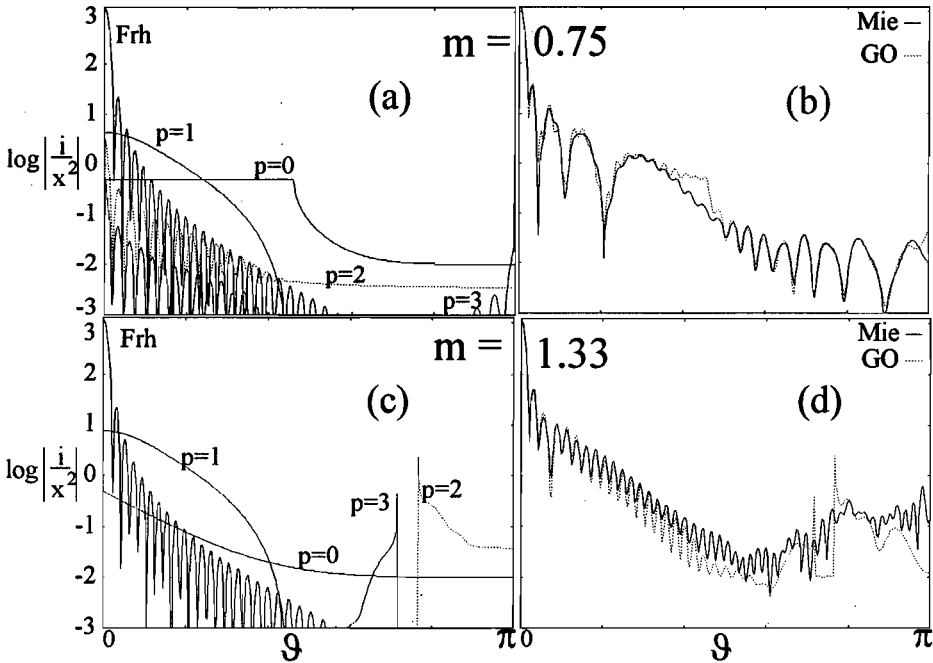


Figure 2.9. Scaled intensity functions i for the indicated refractive indices according to the indicated calculation methods for $x=50$. The GO intensity function in figures b and d was calculated by adding the amplitude functions corresponding with the contributions shown in figures a and c, respectively.

The factor D , called the divergence, describes the geometrical widening of the incident beam. The factor x^2 shows that the intensity is proportional to the cross section of the sphere. The forward directed Fraunhofer diffraction intensity is proportional to x^4 . For very large particles the forward directed intensity ($x\vartheta < 4$) is completely determined by Fraunhofer diffraction. There are different cases for which the nominator of D equals zero, i.e. $D \rightarrow \infty$, and GO leads to erroneous results. These cases will be considered in section 2.7.

In Figs.2.9a and 2.9c the intensity functions i/x^2 for the Fraunhofer diffraction and the first contributions from the ray optics approximation are shown for $x=50$ and respectively $m=0.75$ and $m=1.33$. In both cases the Fraunhofer diffraction is the major contribution for small scattering angles ϑ . For larger angles the $p=1$ ray forms the larger contribution, to be followed by the $p=0$ ray (reflection). For $m=1.33$ both the $p=2$ and $p=3$ rays become major contributions in the backward direction ($\vartheta > \pi/2$).

The total intensity function may in some cases be approximated by adding the intensity function of all contributions, including the Fraunhofer diffraction contribution. The correct intensity however is found by adding the complex amplitude functions S_1 and S_2 of all contributions, and then calculating the intensity function. Besides the moduli of the complex amplitude functions, derived in this section, also the phase of the complex amplitude function is required.

2.7. Phase relations

Besides the phase changes due to reflection and transmission, already given by the total transmission coefficients $\epsilon_j(p)$, three other phase contributions must be included to give the correct phase of a scattered ray, relative to the real Fraunhofer contribution.

- 1. reference ray.

The reference ray is an imaginary ray with constant wavelength outside and inside the sphere. It travels with no phase change through the center of the sphere and from there in any direction. The factor i in the denominator in Eqs.2.3 and 2.4, defining the amplitude functions, gives a factor i in the amplitude function for the reference ray, or a phase shift $+\pi/2$. The amplitude of the incident wave front is opposite to the amplitude of the (imaginary) wave front, used to calculate the Fraunhofer amplitude function of a scattering particle. This gives another phase shift π for the reference ray. The total phase of the reference ray relative to the Fraunhofer amplitude function becomes

$$\sigma_1 = -\frac{\pi}{2} \quad (2.24)$$

The following phase shifts are all relative to this reference ray:

- 2. length of optical path

The length l of the optical path directly affects the phase of a leaving ray. The phase shift relative to the reference ray follows from Fig.2.7, and is given by

$$\sigma_2 = 2x \cdot (p \operatorname{Re}[m \cos\beta] - \cos\alpha) \quad (2.25)$$

- 3. focal lines

Focal points and focal lines are points and lines in space where several rays of a wave front cross. Van de Hulst¹ considers an astigmatic converging beam, i.e. a curved wave front with two different principal radii of curvature, having two focal distances with two focal lines instead of one focal point. He shows that calculation, according to Eq.2.10, of the diffraction pattern of this wave front, gives beyond one focal line a wave front with an extra phase shift $-\pi/2$. Beyond both focal lines the extra phase shift is $-\pi$.

A ray that is scattered by a sphere crosses $p-(1-s)/2$ times an adjacent ray, with $s = 1$ or -1 the opposite of the sign of $d\vartheta/d\alpha$. Each crossing happens similar for all azimuth angles. Connecting one such crossing for all azimuth angles gives a circle around the axis $\vartheta=0$. This circle represents a focal line. The same ray passes $-2k+(1-q)/2$ times the axis $\vartheta=0$ and crosses there the matching rays from all other azimuth angles. The full axis therefore is a focal line. The total advance in phase due to focal lines is

$$\sigma_3 = -\frac{\pi}{2} \left(p - 2k + \frac{s-q}{2} \right) \quad (2.26)$$

The total phase of all separate rays relative to the Fraunhofer contribution is the sum of all mentioned phase shifts.

$$\begin{aligned} \sigma &= \sigma_1 + \sigma_2 + \sigma_3 \\ \sigma &= -\frac{\pi}{2} + 2x(p \operatorname{Re}[m \cos\beta] - \cos\alpha) - \frac{\pi}{2} \left(p - 2k + \frac{s-q}{2} \right) \end{aligned} \quad (2.27)$$

These three contributions to the phase shift are independent of polarization. Knowing the modulus (Eq.2.22) and phase the complex amplitude function for each ray becomes

$$S_j = x \cdot \varepsilon_j \cdot D^{1/2} \cdot e^{i\sigma} \quad (2.28)$$

The total complex amplitude for a specific angle ϑ is the sum of the Fraunhofer amplitude and the amplitudes for all possible rays going in that specific direction ϑ . A certain value of p may have no contribution for a certain scattering angle ϑ , while another value of p may have more than one contribution to a specific scattering angle ϑ .

Figures 2.9b and 2.9d show the intensity functions for the GO approximation calculated by summing the complex amplitude functions for all contributions shown in Figs.2.9a and 2.9c, leading to other values than the summation of intensities of these contributions would give. Their agreement with the exact Mie calculation is for $m=0.75$ and $\vartheta > \pi/2$ very good. For larger values of x , the inaccurate angle ranges become smaller (Fig.2.10). The inaccuracies of the GO approximation occur near special angles as discussed in the next section.

2.8. Exceptional rays

In this section five cases with different types of rays that are not correctly described by GO are discussed. Some of them are indicated in Fig.2.8.

-1. rainbow

For $m > 1$ and values of $p > m$ the scattering angle $\vartheta(\alpha)$ has a maximum where $d\vartheta/d\alpha = 0$ ($D \rightarrow \infty$, Eq.2.23). Close to the rainbow angles the geometrical optics approximation

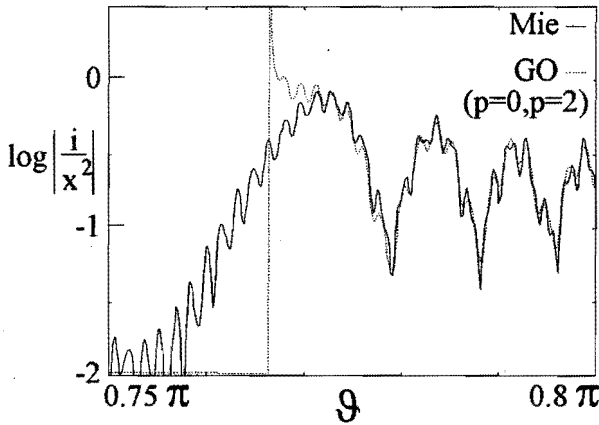


Figure 2.10. Intensity function i/x^2 of the indicated contributions for $x=1024$ near the rainbow angle for $m=1.33$.

deviates from the exact solution. Rewriting Eq.2.18 with the condition $d\vartheta/d\alpha=0$, leads to the following equation for the angle of incidence α for a ray scattered to a rainbow angle

$$\cos^2\alpha = \frac{m^2 - 1}{p^2 - 1} \quad (2.29)$$

This equation leads to a function $\vartheta(\alpha)$ through all rainbow angles for all values of p , indicated by a dashed line in Fig.2.8.

A rainbow angle ϑ depends through the refractive index on the wavelength. Different colors have their intensity maximum at slightly different angles. The well known rainbow corresponds to the $p=2$ contribution from cloud or rain droplets scattering sun light. The $p=3$ rainbow with its colors in reversed order is less intense but also often visible. For ϑ just below a rainbow angle two rays with different angles of incidence are scattered in the same direction. Their interference causes minima and maxima in the scattering pattern, as can just be seen for the $p=2$ contribution in Fig.2.9, but more clearly in Fig.2.10 giving the larger fluctuations. The exact Mie calculation shows that not the exact geometrical rainbow angle, but the angle of the first interference maximum corresponds to the actual angle of highest intensity. For larger size parameters this angle will be closer to the geometrical rainbow angle, and the angle range for which the ray optics approximation fails is smaller. The small ripple in Fig.2.10 is due to interference with the reflection $p=0$.

An approximation for the amplitude function near the rainbow was obtained by Airy¹, who constructed a virtual wave front from all rays leaving near the rainbow, and then calculated the diffraction pattern of that wave front.

-2. axial focus - "glory"

Rays with scattering angle $\vartheta = \pi$ and $\alpha \neq 0$ ($D \rightarrow \infty$, Eq.2.23), indicated by small ellipses in Fig.2.8, leave the particle parallel to the axis $\vartheta = 0$ at the same distance from the axis as they arrive: $a \cdot \sin \alpha$. Fig.2.7 shows the $p=2$ contribution for $m < 1$. These rays have contrary to rays with $\vartheta \neq \pi$ for all azimuth angles ϕ the same direction in space, i.e. they have a focal point on the axis at infinity. This is sometimes referred to as axial focusing or glory scattering. Langley and Marston^{4,5} calculated the amplitude function for glory rays by constructing a wave front for all rays leaving in a direction close to $\vartheta = 0$ for all azimuth angles ϕ , and calculating the diffraction pattern of this wave front. They also observed corresponding virtual ring sources inside a sphere. This approach was already suggested by van de Hulst, who also gave an asymptotic approximation for the exact solution allowing a direct derivation of the equation for axially focused rays (Chapter 3). In the backward direction such rays are major contributions to the intensity. In the forward direction they slightly modify the Fraunhofer diffraction pattern.

The optical effect leading to the name "glory" is due to a relative strong backward reflection from mist or clouds. This makes driving a car with lights on in a thick fog difficult, but the name results from the colored rings around a shadow on a cloud, as can be seen from a mountain top or an aircraft, making each observer 'his own saint'. The near backward $p=2$ contribution from water drops for $\alpha = \pi/2$, leading to this "glory", requires a small extra angular displacement (15°) to be emitted exactly backwards ($m=1.33$, Fig.2.8). This extra angular displacement was first quantitatively explained by Nussenzweig⁸ using complex wave numbers (see -4. critical angle). Nussenzweig also gives a historical review of recorded observations of the "glory" and references that present color photographs.

-3. edge rays

Rays that hit near the edge ($\alpha = \pi/2$) of the sphere are reflected close to the forward direction ($\vartheta \sim 0$). This grazing reflection occurs for all azimuth angles ϕ . As for the glory a limited wave front and its diffraction pattern could be calculated. Because the phase of the edge reflection in forward direction, contrary to the earlier mentioned contributions from axial focusing, does not depend on the size parameter x , the amplitude function should be added to the Fraunhofer amplitude function and is likely to be more significant. The edge contribution may be derived from the exact solution as shown in Chapter 3.

For $m > 1$ the extreme edge ray ($\alpha = \pi/2$) is partly refracted into the sphere and leaves the sphere partly at regular ϑ intervals (Fig.2.8). This ray is both inside and for all $p > 1$

outside the sphere a boundary between a lit and shadow region. Some light diffracts from the lit region to the shadow region. Therefore the ray optics approximation is also inaccurate close to the angles ϑ to which a part of the edge ray is refracted, .

-4. critical angle

A two-dimensional plane wave with wave vector $\mathbf{k}_1 = (k_{1,x}, k_{1,z})$ incident at a plane interface $z=0$ between two media 1 and 2 with refractive indices n_1 and $n_2 < n_1$, respectively, leads to a reflected wave $\mathbf{k}_r = (k_{1,x}, -k_{1,z})$ and a transmitted wave $\mathbf{k}_2 = (k_{2,x}, k_{2,z})$, where the transmitted wave vector components satisfy $k_{2,x} = k_{1,x}$ and $k_{2,z}^2 = |\mathbf{k}_2|^2 - k_{2,x}^2 = (n_2 / n_1)^2 |\mathbf{k}_1|^2 - k_{1,x}^2$. For a wave incident at an angle larger than the critical angle α_{crit} , where $\sin \alpha_{\text{crit}} = n_2 / n_1$, the z -component in medium 2 $k_{2,z}$ is imaginary. In this case the wave vector \mathbf{k}_2 represents a surface wave, that travels along the interface having an amplitude that exponentially depends on the distance from the interface. No power is refracted into the medium 2, but the power of an incident wave is shifted along the interface before it emerges as a reflected wave. (Goose-Hanchen effect³). The complex angular momentum approximation⁸ accounts for these types of waves traveling along the sphere interface.

Right below the critical angle the reflection coefficients steeply increase to the value 1 causing the steep increase for the reflected wave $p=0$ in Fig.9a. Kingsbury and Marston^{6,7} constructed a virtual wave front for the $p=0$ and $p=1$ rays near that angle and calculated the diffraction pattern. They neglected the Goose-Hanchen effect, but they found a reasonable match with the Mie theory. The angle range for which this effect plays an important role also depends on the size parameter.

-5. Anomalous Diffraction

Considering only the near forward direction, then for $m \approx 1$ only the ray $p=1$ contributes significantly. Instead of considering separate rays the circular wave front that passes the sphere is considered. Just as for the Fraunhofer contribution the diffraction pattern of this front is calculated, taking the position dependent phase delay into account (van de Hulst¹, Chap.11, p.183).

2.9. Extinction

Extinction describes the intensity decrease of light due to the presence of particles. The extinction cross section C_{ext} is the area that effectively removes energy from a proceeding wave. The extinction efficiency of a particle is defined as the ratio of this area C_{ext} and the geometric cross section πa^2 .

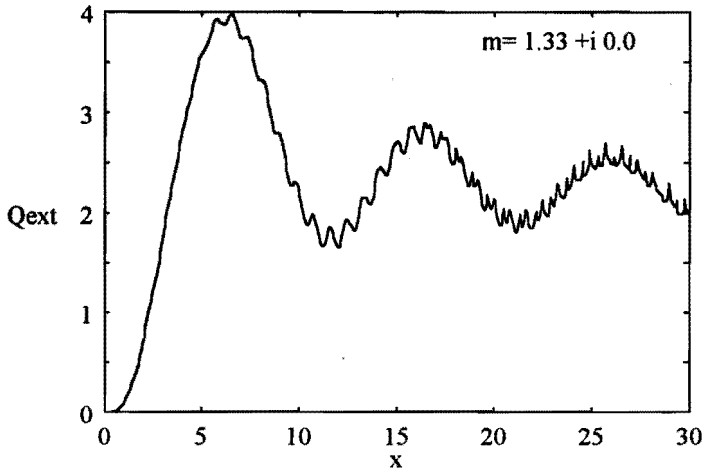


Figure 2.11. Extinction efficiency Q_{ext} as function of size parameter x for $m=1.33$

$$Q_{\text{ext}} = \frac{C_{\text{ext}}}{\pi a^2} = \frac{4}{x^2} S(0) \quad (2.30)$$

The extinction efficiency for perfectly absorbing particles (Eq.2.13) $Q_{\text{ext}}=2$, i.e. the area that effectively removes energy, is twice the geometric cross section. This ratio is explained by "Babinet's principle", i.e. the diffraction pattern of a wave front, partially blocked by a particle, is equal to the diffraction pattern of a hole with the same geometric cross section as the particle. The diffraction of the surrounding rays removes thus an equal amount of energy from the original direction as the particle itself. The geometric cross section effectively lowers the forward scattering amplitude of the undisturbed wave front, giving a factor 2 in the resulting square of the remaining forward intensity. Figure 2.11 shows that for relative refractive index $m=1.33$ the extinction efficiency approaches slowly this value.

2.10. Complex angular momentum (CAM) theory

Several features in the exact solution of scattering by a sphere are not or inaccurately described by ray tracing and simple diffraction theory. The CAM theory, described by Nussenzweig⁸, includes surface waves, i.e. complex wave numbers, and gives a quantitative explanation for virtually all noticed features. The Mie theory shows that e.m. scattering by a sphere may be exactly described by three sets of infinite summations of certain solutions of the Maxwell equations in spherical coordinates for the incident, internal and scattered wave, respectively, that satisfy the boundary conditions at the sphere surface. A transformation is possible, that allows all internal solutions to be separated in contributions that represent waves travelling towards or away from the

center. A wave travelling towards the center implies the presence of a similar outgoing wave. The incident wave, the directly reflected wave, and the first of the inside waves travelling towards the center together satisfy the boundary conditions. The first of the internal waves travelling away from the center is partially reflected and partially transmitted at the sphere surface by spherical reflection coefficients, etc. This transformation of the exact solution has as the GO approximation separate contributions corresponding with a different number of internal paths. The subsequent summation of all terms corresponding with one ray allows approximate expressions for $|m - 1|^{1/2} x^{1/3} \gg 1$ and $(1 + m^2)^{1/2} \cdot x^{-1/3} \ll 1$.

2.11. Conclusion.

The scattering properties of spherical particles with any size parameter x and any relative refractive index m are exactly given by the solution from Mie, that requires however for large x a long calculation time. Geometrical Optics gives for large values of x and $\rho = 2x(m - 1) \gg 1$ an approximation for the scattering pattern. The accuracy of the GO approximation is better for larger x , but this depends strongly on m and the considered scattering angle.

References

1. H. C. van de Hulst, *Light Scattering by Small Particles*, Wiley New York (1957)
2. G. F. Bohren and D. R. Huffman, *Absorption and Scattering by Small Particles*, Wiley, New York (1983)
3. J. Petykiewicz, *Wave Optics*, Kluwer Academic Publishers (1992)
4. D. S. Langley and P. L. Marston, "Forward Glory Scattering From Bubbles," *Appl. Opt.* **30**, 3452-3458 (1991).
5. D. S. Langley and M. J. Morrell, "Rainbow Enhanced Forward and Backward Glory Scattering," *Appl. Opt.* **30**, 3459-3467 (1991).
6. P. L. Marston and D. L. Kingsbury, "Scattering by a bubble in water near the critical angle: interference effects", *J.Opt.Soc.Am.* **71**, 192 (1981).
7. D. L. Kingsbury and P. L. Marston, "Mie scattering near the critical angle of bubbles in water" *J.O.S.A.Letters* **71**, 358 (1981)
8. H. M. Nussenzweig, *Diffraction Effects in Semiclassical Scattering*, (Cambridge University Press, 1992).

Chapter 3. Edge contribution to forward scattering.

Edge functions T_1 and T_2 , which describe the polarization-dependent edge contribution to forward scattering by spheres, are derived from the exact Mie solution. The edge functions significantly improve approximate methods to calculate forward scattering patterns. All the relative refractive indices and the $64 < x < 2048$ size parameter range are considered. For smaller values of x the approximations are inaccurate while for larger values of x the edge contribution is very small. For m close to 1 an asymptotic approximation is used. Otherwise the familiar geometrical optics approximation and the similar physical optics approximation for glory rays are used. Both geometrical and physical optics equations can be deduced from the above mentioned asymptotic approximation.

3.1. Introduction

The scattering pattern of spherical particles, with any relative refractive index $m = n_{\text{sphere}} / n_{\text{medium}}$ and size parameter $x = 2\pi a / \lambda$, where a is the radius of the sphere and λ is the wavelength, may be calculated using the exact solution according to Mie^{1,4}, but this requires a long calculation time for large values of x .

For x large and m not close to 1, it is possible to calculate the scattering pattern of a sphere by calculating separately the contributions from incident and non-incident rays. The incomplete wave front of the non-incident rays gives a Fraunhofer diffraction pattern. The energy of an incident ray is divided among several leaving rays p , see Fig.2.7, giving several contributions to the scattering pattern that can be calculated using geometrical optics (GO).

Glory rays, i.e. non-axial rays that are scattered in forward or backward direction, have infinite intensity according to the GO approximation. Langley and Marston^{2,3} detail a Physical Optics (PO) approximation, using both ray optics and diffraction theory. It is shown in this chapter that like the GO equations, the PO equations may be derived from the exact solution via an asymptotic approximation presented by Van de Hulst¹ (Chap.12, p.208).

This asymptotic approximation may not be used for rays incident on the edge of the sphere, i.e. for small values of τ (Fig.2.7). The partially reflected rays close to the forward direction will diffract into the shadow region behind the sphere just like the rays that miss the particle and cause the Fraunhofer diffraction. The edge domain for which reflected rays are significantly diffracted depends on the size parameter and is given by

$\tau < x^{-1/3}$ (Van de Hulst¹ Chap.17, p.349), i.e. for very large values of x the edge contribution may be neglected.

It will be shown that the difference between the exact Mie solution and the approximation for forward scattering patterns, for moderate values of x (64-2048) and averaged over a size range Δx , results from the edge domain. This edge contribution can be expressed by two edge functions T_1 and T_2 that can be represented by several polynomials of x and m . The averaged Mie solution may now be reconstructed by adding the approximation and the edge contribution.

Two authors describe other approximate calculation methods for light scattering that also have separate terms for the edge contribution.

Nussenzveig^{5,6,7} presents the complex angular momentum (CAM) theory that gives a physical explanation for all features of the exact Mie solution. The CAM theory allows approximate expressions that are valid for $x^{1/3} \gg 1$ and $|m-1|^{1/2} x^{1/3} \gg 1$. A presented expression for the extinction efficiency⁷ is compared with our result.

Chen^{8,9} generalizes the Eikonal Approximation (valid for scalar waves and m near 1) with two parameters and adapts these parameters to fit the approximation to the exact solution in the exact forward direction. The maximum size parameter, for which a scattering pattern $0 < \vartheta < 30^\circ$ is presented, is $x = 30$ together with $m = 1.33$. The GO approximation with an edge contribution is a better approximation for this case, maybe because the difference for both polarizations at the edge is not accounted for in the generalized eikonal approximation. Calculation times for both methods are not compared.

3.2. Asymptotic approximation.

In this section the asymptotic approximation that was presented by van de Hulst¹, Ch.12 to demonstrate the correspondence of the exact solution and the GO approximation is used to derive an asymptotic formula (AF) that will be used to approximate the forward scattering pattern for $m \approx 1$. Sharma¹⁰ used the same approximation to explain the large range of m values where the anomalous diffraction approximation¹, Ch.11 gives good results for the extinction efficiency $Q_{\text{ext}} = 4 \cdot S(0) / x^2$.

The exact solution is given by (van de Hulst¹, Chap.9)

$$S_1(x, \vartheta) = \sum_{n=1}^{\infty} \frac{2n+1}{n(n+1)} [a_n \pi_n(\cos \vartheta) + b_n \tau_n(\cos \vartheta)] \quad (3.1)$$

and a corresponding expression for S_2 with a_n and b_n interchanged. The terms of Eq.3.1 are large for $n < x$, and drop sharply to zero for n near x . Only approximate expressions for the Mie coefficients a_n , b_n and the spherical harmonics τ_n , π_n are presented in this thesis. The exact solution may be calculated faster using an algorithm by Bohren and Huffman⁴. Both scattering coefficients can be exactly written as (van de Hulst, Chap.10)

$$a_n = \frac{1}{2}(1 - e^{-2i\alpha_n}) \quad b_n = \frac{1}{2}(1 - e^{-2i\beta_n}) \quad (3.2)$$

Both coefficients contain a term $1/2$ that corresponds with the Fraunhofer diffraction and is omitted in the further consideration. The remaining terms depend on the size parameter x and the relative refractive index m . For large x and excluding the edge domain the following asymptotic approximation may be used (van de Hulst, Chap.12)

$$a_n = \frac{-e^{-2i\alpha_n}}{2} \approx \frac{u_0}{2} \cdot \frac{u_i + r_2}{1 + u_i \cdot r_2} = \frac{u_0}{2} \cdot \left[r_2 + (1 - r_2^2) \cdot \sum_{p=1}^{\infty} u_i^p \cdot (-r_2)^{p-1} \right] \quad (3.3)$$

where reflection coefficient $r_2 = \tan(\tau - \tau') / \tan(\tau + \tau')$. The angles τ and τ' are defined by

$$x \cdot \cos \tau = x' \cdot \cos \tau' = n + 1/2 \quad (3.4)$$

where $x' = m \cdot x$. Equation 3.4 demonstrates the localization principle, i.e. each term n in Eq.3.1 corresponds with a ray incident at a specific angle of incidence. The separate terms in the right hand side of Eq.3.3 correspond to the leaving rays $p=0,1,2..etc$ (Fig.2.7). A similar approximation is allowed for b_n with r_2 replaced by $r_1 = \sin(\tau - \tau') / \sin(\tau + \tau')$. The function

$$u_0 = -i \cdot e^{-2i \cdot x \cdot f} \quad \text{with} \quad f = \sin \tau - \tau \cdot \cos \tau \quad (3.5)$$

contains external values, and

$$u_i = -i \cdot e^{2i \cdot x' \cdot f'} \quad \text{with} \quad f' = \sin \tau' - \tau' \cdot \cos \tau' \quad (3.6)$$

contains internal values for angle and size parameter. The notation used here deviates from the notation used by van de Hulst in the meaning that $e^{-i\omega t}$ instead of $e^{i\omega t}$ is used as time dependence.

For one value of $p > 1$ the scattering coefficients are given by

$$a_n \approx \frac{u_0 u_i^p}{2} (1 - r_2^2) (-r_2)^{p-1} = \frac{u_0 u_i^p}{2} \epsilon_{2,p} \quad (3.7)$$

$$b_n \approx \frac{u_0 u_i^p}{2} (1 - r_1^2) (-r_1)^{p-1} = \frac{u_0 u_i^p}{2} \epsilon_{1,p} \quad (3.8)$$

where the total amplitude transmission coefficients $\epsilon_{j,p}$ were already defined by Eq.2.17.

Van de Hulst¹ replaces besides the scattering coefficients a_n and b_n also the spherical harmonics π_n and τ_n in Eq.3.1 by asymptotic approximations, that are valid for all angles except close to the forward and backward direction. The function π_n is much smaller than τ_n so the amplitude functions S_j are mainly determined by the corresponding total amplitude transmission coefficients $\varepsilon_{j,p}$. A subsequent stationary phase approximation leads to the GO equations.

Van de Hulst already suggests replacing the spherical harmonics π_n and τ_n by asymptotic approximations that are valid near the forward or backward direction for large n , i.e. excluding axial rays

$$\pi_n(\cos\vartheta) \approx n(n+1) \frac{J_0(u) + J_2(u)}{2} s^{n-1} = n(n+1) \frac{J_1(u)}{u} s^{n-1} \quad (3.9)$$

$$\tau_n(\cos\vartheta) \approx n(n+1) \frac{J_0(u) - J_2(u)}{2} s^n = n(n+1) J_1'(u) s^n \quad (3.10)$$

where for the forward direction $u = (n+1/2) \cdot \vartheta$ and $s=1$, while for the backward direction $u = (n+1/2)(\pi - \vartheta)$ and $s=-1$, and J_0 , J_1 and J_2 are the first three integer Bessel functions of the first kind.

The forward scattering amplitude, excluding the Fraunhofer diffraction and reflection terms and using the average reflection coefficient $r = (r_1 + r_2)/2$, leads to the scattering coefficients

$$a_n = b_n \approx u_0 \cdot \left(\frac{u_i + r}{1 + u_i \cdot r} - r \right)$$

Substituting in Eq.3.1 also Eq.3.4 and the first part of Eqs.3.9 and 10 leads to following approximation

$$\frac{S_j(x, \vartheta)}{x^2} = \int_{\tau_{\text{low}}}^{\pi/2} u_0 \cdot \left(\frac{u_i + r}{1 + u_i \cdot r} - r \right) J_0(x \cos\tau \cdot \vartheta) \cdot \cos\tau \cdot \sin\tau d\tau, \quad (3.11)$$

that is independent of the polarization $j=1,2$ and where the summation of Eq.3.1 is replaced by an integral over $dn = d(x \cos\tau) = x \sin\tau d\tau$, using the fact that only terms $n \leq x$ significantly contribute. This replacement is allowed if the integrand is a slowly varying function of τ . For $m < 1$ the function u_i (Eq.3.6) is a rapid fluctuating function for $0 < \tau < \tau_{\text{crit}}$, where $\cos\tau_{\text{crit}} = m$ defines the critical angle for refraction into a medium with lower refractive index. The lower limit of the integral in Eq.3.11 is therefore taken as $\tau_{\text{low}} = \tau_{\text{crit}}$, while for $m > 1$ $\tau_{\text{low}} = 0$. The anomalous diffraction approximation (see Ch.2, p.26) that is valid for $m \approx 1$ results from Eq.3.11 by substituting $r = 0$, $u_0 \cdot u_i = -e^{i\rho \sin\tau}$, $\rho = 2x(m-1)$ and $\tau_{\text{low}} = 0$.

The advantage of this asymptotic formula over the exact Mie solution is the following. The Mie algorithm makes, regardless of the value of m , a summation over a little more than x terms. The integrand in Eq.3.11 is for m near 1 a slowly varying function of τ and for sizing systems using forward scattering the integral is determined numerically accurately enough with $O(1) \cdot x^{2/3}$ terms.

While the cumulative integral of the anomalous diffraction approximation for $z=0, \vartheta=0$ in the complex domain gives a smooth spiral, the corresponding cumulative result Eq.3.11, for $z=0$ gives approximately the same spiral with oscillating curvature. The use of the asymptotic formula Eq.3.11 will be referred to by the abbreviation AF.

3.3. Glory rays

In this section an equation for glory rays, i.e. non axial rays that are scattered in forward or backward direction (e.g. $p=2$ in Fig.2.7) is derived using the approximations of the previous section. The result matches the Physical Optics (PO) approximation by Langley and Marston^{2,3}. They also consider the rainbow enhanced glory, that is not considered here.

The presented derivation is similar to the derivation of the GO equations by van de Hulst¹. Substituting Eqs.3.7, 3.8, 3.9 and 3.10 in Eq.3.1 and the corresponding equation for S_2 leads for both polarizations $j=1,2$ to

$$S_{j,p}(x, \vartheta) = \sum_{n=1}^{\infty} \left(n + \frac{1}{2} \right) \left[\varepsilon_{3-j,p} \frac{J_1(u)}{u \cdot s} + \varepsilon_{j,p} J_1'(u) \right] \cdot u_0 \cdot u_i^p \cdot s^n \quad (3.12)$$

where for the forward direction $u = (n+1/2) \cdot \vartheta$ and $s=1$, while for the backward direction $u = (n+1/2)(\pi - \vartheta)$ and $s=-1$, and u_0 and u_i are given by Eqs.3.5 and 3.6.

The last three factors of Eq.3.12 may be rewritten as

$$u_0 \cdot u_i^p \cdot s^n = e^{-iG_n}, \quad G_n = 2(xf - px'f') + (p+1) \frac{\pi}{2} - L\pi n. \quad (3.13)$$

In the forward direction $L=0$ and in the backward direction $L=1$. The complex terms nearly cancel one another except near a value $n=n_0$ where $G_{n+1} - G_n + h \cdot 2\pi = 0$ is nearly satisfied. Replacing the difference with a derivative

$$\frac{d}{dn} = \frac{1}{x} \frac{d}{d \cos \tau} = \frac{-1}{x \sin \tau} \frac{d}{d\tau}$$

leads to the condition

$$G'_n + h \cdot 2\pi = -2\tau + 2p\tau' - L\pi + h \cdot 2\pi = 0 \quad (3.14)$$

for a forward or backward directed ray. The term $h \cdot 2\pi$ may be omitted if L is allowed to assume any even value in the forward direction and any uneven value in the backward direction. This condition determines the values of n_0 , τ and τ' . Multiplying this equation

with $n_0 + 1/2 = x \cos \tau = x' \cos \tau'$ and subtracting the product from G_n gives the following expression for the phase delay of such a ray

$$G_{no} = 2x \sin \tau - 2px' \sin \tau' + (p + 1 + L) \frac{\pi}{2} \quad (3.15)$$

For the summation around n_0 the first two factors of Eq.3.12 are quasi constant. Replacing the summation by an infinite integral and G_n by a second order approximation leads to the Fresnel integral

$$\int e^{-iG_{no} - i\frac{1}{2}(n-n_0)^2 G''_{no}} dn = \left(\frac{2\pi}{|G''_{no}|} \right)^{1/2} e^{-iG_{no} - i(\pi/4)s_A} \quad (3.16)$$

where

$$G''_{no} = \frac{-A}{x \cos \tau}, \quad A = \frac{2p}{\tan \tau'} - \frac{2}{\tan \tau}$$

and s_A is the sign of A . The resulting amplitude function is given by

$$S_{j,p}(x, \vartheta) = (x \cos \tau)^{3/2} \left(\frac{2\pi}{|A|} \right)^{1/2} \left[\varepsilon_{3-j,p} \frac{J_1(u)}{u \cdot s} + \varepsilon_{j,p} J_1'(u) \right] e^{-iG_{no} - i(\pi/4)s_A} \quad (3.17)$$

where $u = x \cos \tau \cdot \vartheta$ or $u = x \cos \tau (\pi - \vartheta)$ for the forward or backward direction respectively and τ is determined by Eq.3.14. The expression in square brackets corresponds with a virtual ring source with diameter $u/\vartheta = x \cos \tau$ as photographed by Langley and Marston³, who find a corresponding equation using ray optics and diffraction theory (Physical Optics approximation). Contrary to the GO amplitude functions (Eq.2.28) the PO amplitude functions depend on both transmission coefficients ε_1 en ε_2 .

For specific values of the relative refractive index $m > 1$ rainbow enhanced glory contributions occur, i.e. if both $A = 0$ and Eq.3.14 are satisfied. A third order approximation of G_n is then required, which is not detailed any further, because it does not apply to our experimental system of water drops in kerosene for which $m \approx 0.93$.

3.4. Edge functions from Mie solution

The edge rays are reflected in forward direction. If their contributions $S_{1,edg}$ and $S_{2,edg}$ to the total amplitude functions are assumed to be diffraction patterns that radiate from a circle around the sphere (dotted circle in Fig.2.2), then the angular dependence of the forward diffraction pattern is similar as for the glory contributions that have a virtual ring source. The factor in square brackets in Eq.3.17 is used to represent this forward ($s = 1$) angular dependence,

$$\frac{S_{j,edg}(x, z)}{2x} = T_{3-j}(x) \frac{J_1(z)}{z} + T_j(x) J_1'(z), \quad (3.18)$$

where $z = x \cdot \sin \vartheta \approx x \cdot \vartheta$ and the amplitude transmission coefficients $\varepsilon_{j,p}$ are replaced by two unknown edge functions T_j and the factor $2x$ in the left-hand sides corresponds with

the definition of the edge functions by van de Hulst¹ (Chap.17). The edge functions are assumed independent of the scattering angle ϑ .

The same angular dependence is also found by considering the virtual ring source for glory contributions, or the ring-shaped reflected wave front at the edge of the sphere, where for all azimuth angles the incident wave leads to two components in the plane of the ring, a component parallel and a component perpendicular to the plane of incidence. These components are transmitted (glory) or reflected (edge) according to the transmission coefficients ε_j or reflection coefficients r_j . Decomposition of the two resulting amplitudes to the incident and perpendicular polarization direction, and calculating the resulting diffraction pattern of both components by integration over the azimuth angle also leads to the angular dependence of Eq.18. (van de Hulst¹, Chap.11)

The width of the relevant wave front is neglected in the assumption of Eqs.18. The actual relevant edge domain is given by a specific value of the angle τ (Fig.2.7) that depends on the size parameter x : $\tau_{\text{edg}} = x^{-1/3}$ (van de Hulst¹, Chap.17). The width of the relevant part of the incident wave front is thus given by $x(1 - \cos\tau_{\text{edg}}) \approx x^{1/3}/2$ which is for large values of x small compared to the circumference of the circle.

In the following sections the edge contributions $S_{j,\text{edg}}$ are calculated by subtracting from the exact 'Mie' solution, the Fraunhofer pattern and one or more contributions ($p=1,2,\dots$) calculated using the asymptotic approximation (leading to the GO and PO approximation) presented by van de Hulst. The resulting difference should have an angular dependence corresponding with Eq.18 and the edge functions T_j , $j=1,2$ follow directly from the first null point in $J_1'(z_a) = 0$, $z_a=1.84,\dots$ (referred to as method a),

$$T_{j,a}(x) = \frac{S_{3-j,\text{edg}}(x, z_a)}{2x \cdot J_1(z_a)/z_a}, \quad (3.19)$$

and also from the first null point in $J_1(z_b) = 0$, $z_b=3.83,\dots$ (referred to as method b),

$$T_{j,b}(x) = \frac{S_{j,\text{edg}}(x, z_b)}{2x \cdot J_1'(z_b)} \quad (3.20)$$

If the considered amplitude functions $S_{j,\text{edg}}$ indeed radiates from the circle at the edge of the sphere then both methods should give identical edge functions: $T_{j,a} = T_{j,b}$. Due to the actual ratio of the width of the relevant wave front to the diameter of the circle around the sphere, given by $x^{1/3}/x = x^{-2/3}$, the differences $T_{j,a} - T_{j,b}$ will be smaller for larger values of x . Using $J_0(0) = 1$ and $J_2(0) = 0$ the following relations must also be true:

$$S_{j,\text{edg}}(x, 0) \approx x(T_{1,a} + T_{2,a}) \approx x(T_{1,b} + T_{2,b})$$

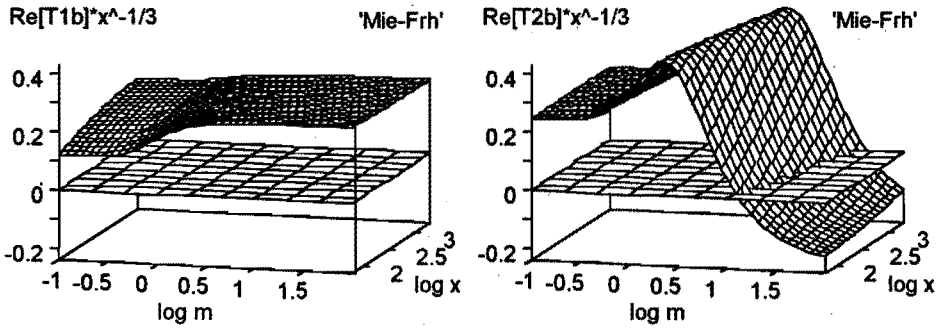


Figure 3.1. Real part of the edge functions T_1 and T_2 multiplied by $x^{-1/3}$, calculated using method b for $0.1 < m < 100$, $\text{Im}[m] = \text{Re}[m]$ and $64 < x < 2048$.

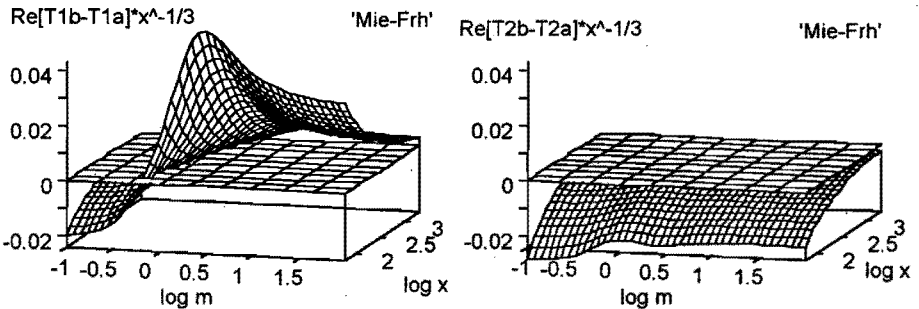


Figure 3.2. Difference between the edge functions from Fig. 3.1 and the corresponding edge functions calculated using method a.

The amplitude functions $S_{1,\text{edg}}$ and $S_{2,\text{edg}}$ are calculated by subtracting from the exact Mie solution different approximations in different ranges of the complex relative refractive index m .

3.5. Absorbing sphere

The simplest case for determining the edge functions according to the previous section is a value of m with large imaginary part so all $p > 0$ contributions are absorbed and only the Fraunhofer diffraction and edge contribution are important for the forward scattering pattern: $S_{j,\text{edg}} = S_{j,\text{Mie}} - S_{\text{Frh}}$. For such a subtraction a short notation of the type 'Mie-Frh' will be used. Figure 3.1 shows the resulting real part of edge functions T_1 and T_2 according to method b for $64 < x < 2048$, $0.1 < m < 100$ and $\text{Im}[m] = \text{Re}[m]$. Figure 3.2 shows that the differences $T_{j,a} - T_{j,b}$ between the results from method a and method b for $x = 64$ is an order of magnitude smaller than $T_{j,b}$, while for larger values of x the difference decreases as $x^{-2/3}$. This result shows that it is indeed possible to deduce the edge functions from the exact Mie solution, and that including these edge functions in the approximation will decrease its error significantly.

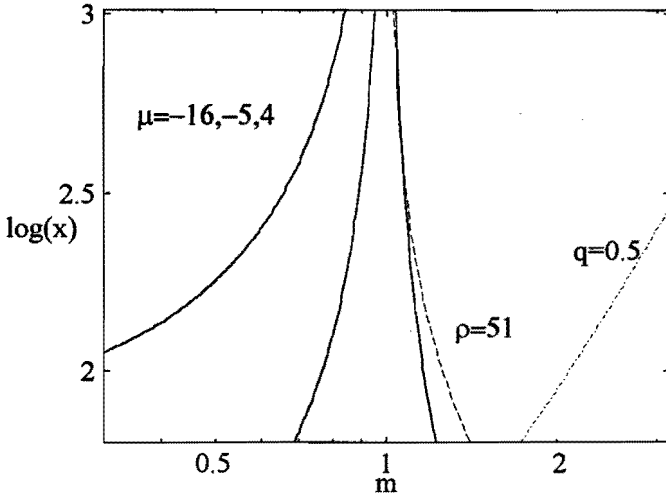


Figure 3.3. The m - x area for $0.3 < m < 3$ and $64 < x < 1024$, divided in areas bounded by indicated conditions for μ , ρ and q .

It was found from the comparison of the differences $S_{1,\text{edg}}(x, 0) - x(T_{1,a} + T_{2,a})$ and $S_{1,\text{edg}}(x, 0) - x(T_{1,b} + T_{2,b})$ that method b gives a slightly better approximation in the exact forward direction than does method a.

3.6. Transparent sphere

The largest contribution to forward scattering besides the Fraunhofer diffraction and the edge reflection for real values of m is the twice refracted $p=1$ ray, leading to the definition

$$S_{j,\text{GO}} = S_{\text{Frh}} + S_{j,p=1}$$

where $S_{j,p=1}$ is calculated according to GO. The $p > 1$ contributions to S_{Mie} are diminished by averaging $S_{j,\text{Mie}} - S_{j,\text{GO}}$ over a size range $\Delta x \approx x/8$ leading to a scattering amplitude that results from the edge $S_{j,\text{edg}} = \overline{S_{j,\text{Mie}} - S_{j,\text{GO}}}$.

This is true for the largest part of the m - x range shown in Fig.3.3 but not for the area around $m=1$ bounded by $\mu = -16$ and $\rho = 2x(m-1) = 51$. The parameter μ is defined here as $\mu = (m-1) \cdot x^{2/3} \approx (\tau_{\text{crit}} / \tau_{\text{edg}})^2$, giving a measure for the critical angle position in the edge domain.

For $-16 < \mu < -5$ the glory rays of the type as discussed in section 2 are not sufficiently diminished by averaging and are included in the definition

$$S_{j,\text{PO}} = S_{j,\text{GO}} + S_{j,p=2,9}$$

where the second term is the sum of the glory contributions according to the PO approximation for $p = 2$ to $p = 9$ with $L = 0$. In this range the averaged difference with the exact solution is found to result from the edge $S_{j, \text{edg}} = \overline{S_{j, \text{Mie}} - S_{j, \text{PO}}}$.

In the remaining range for $-5 < \mu$ and $\rho < 51$ the difference between the exact solution $S_{j, \text{Mie}}$ and the asymptotic approximation of Eq.3.11 including the Fraunhofer diffraction, referred to as $S_{j, \text{AF}}$, also leads to a scattering amplitude resulting from the edge $S_{j, \text{edg}} = \overline{S_{j, \text{Mie}} - S_{j, \text{AF}}}$. Figure 3.4 shows for the range $-4 < \mu < 4$ the resulting edge function $T_{1, b}$ (Eq.3.19) and the difference $T_{1, a} - T_{1, b}$, that is much smaller than $T_{1, b}$, indicating that in this range $T_{1, b}$ for 'Mie-AF' may indeed be interpreted as an edge function.

The edge functions, multiplied by $x^{-1/3}$, are in this range a function of parameter μ and hardly a function of x . Right below $\mu=0$ the Goose Hanchen effect^{1,7,11} probably causes the deep dip in the edge function, while the rest of the fluctuations may be interpreted as the result of continuous diffraction interaction between incident, reflected and inside waves in the edge domain.

For $|\rho| < 0.01$ the Rayleigh-Gans¹ approximation is used. In the presented figures only the $m = 1$ line corresponds to this case.

For $m > 1$ the reflection coefficient r_2 changes sign at the Brewster angle τ_{Brw} where $\tau + \tau' = \pi/2$. A parameter q is defined here that gives the inverse of the relative position of the Brewster angle in the edge domain $q = (1 + m^2)^{1/2} \cdot x^{-1/3} = \tau_{\text{edg}} / \sin \tau_{\text{Brw}}$. Figure 3.5 shows the functions $T_{1, b}$ and $T_{2, b}$ as function of this parameter q calculated for $S_{j, \text{edg}} = \overline{S_{j, \text{Mie}} - S_{j, \text{GO}}}$. The remaining ripple in Fig.3.5 is due to rays with $p > 1$ and may be diminished with a better averaging method. Near $q = 0.1$ and $x = 64$ the refractive index m would be less than 1 according to the definition of q , so the edge function is simply set to 0. The flat region is calculated for a refractive index with a small imaginary component ($\text{Im}[m]/\text{Re}[m] < 10^{-4}$) without averaging.

For $64 < x < 1024$ different polynomials of the functions $T_{1, b} \cdot x^{-1/3}$ and $T_{2, b} \cdot x^{-1/3}$ as function of x and one of the real parameters m , μ or q are determined. It seems not to difficult to extend the polynomials to complex values of m .

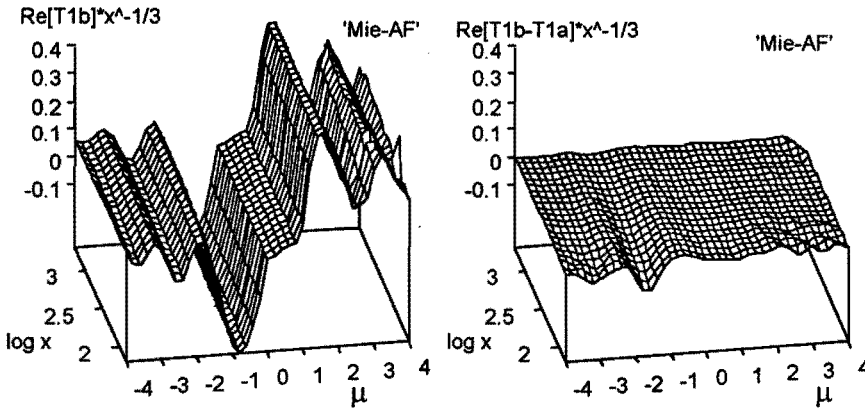


Figure 3.4. Real part of the edge function T_1 multiplied by $x^{-1/3}$, calculated according to method b (upper figure) for $-4 < \mu < 4$ and $64 < x < 2048$, and the difference with the corresponding function calculated according to method a (lower figure).

The edge functions lead through Eq.3.18 back to the forward scattering pattern resulting from the edge that may be added to the appropriate averaged approximation (GO, PO or AF) for the forward scattering pattern, thereby improving its accuracy significantly. The next section discusses the resulting accuracy for the exact forward direction ($\vartheta = 0$) compared to the accuracy of an approximation resulting from the CAM approach⁷.

The calculation time required for the GO and PO approximation including the edge contribution, using a polynomial fit, is approximately a factor x lower than time required for the exact Mie solution⁴. The calculation time required for the AF depends strongly in the number of terms used for numerical evaluation of Eq.3.11, but is for the mentioned number of terms approximately a factor $x^{1/3}$ faster than the exact solution. Only the size parameter range $64 < x < 2048$ and calculation for a specific x value is considered here. For calculation of scattering matrix elements, where adding of intensities of different contributions for large enough values of x is allowed, the time to be gained for the GO and PO approximation will be larger.

3.7. Comparison with CAM extinction efficiency.

The approximation presented here is compared to the CAM approximation presented by Nussenzveig⁷ for the extinction efficiency $Q_{\text{ext}} = 4 \cdot S(0) / x^2$, $64 < x < 1024$ and $1.1 < m < 2.5$. For the major part of this m - x area both approximations are equally good⁷. The CAM approximation is near $\mu = 4$ (Fig.3.3) better, due to an improved $p=1$ contribution. For $\mu < 4$ and $q > 0.5$, using the AF and GO respectively, the method presented here is better. The CAM approximation neglects penetration of outside complex surface waves into the sphere⁵ leading to the condition $|m-1|^{1/2} x^{1/3} =$

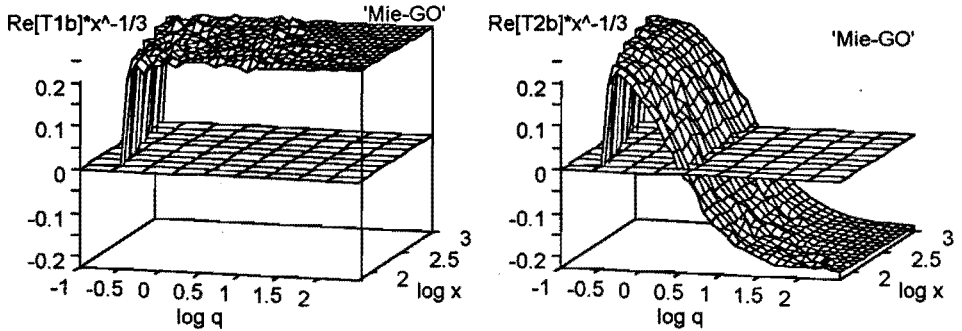


*Figure 3.5. Real part of the edge functions T_1 and T_2 multiplied by $x^{-1/3}$, calculated using method *b* for $0.1 < q < 316$, $Im[m]=0$ and $64 < x < 1024$.*

$\mu^{1/2} \gg 1$. If the Brewster angle approaches the edge ($q > 0.5$, section 3.5) transmission into the sphere for polarization 2 is probably not negligible, leading to less accurate CAM results. For smaller values of x the width of the edge domain is larger, so the method presented here leads to worse results.

3.8. Summary

It has been shown that the edge functions T_1 and T_2 as used by Van de Hulst¹ can be determined through the rigorous Mie solution by subtracting appropriate approximations. The relative error of the edge functions determined this way is approximately 10% for size parameter $x = 64$ and decreases as $x^{-2/3}$ for higher values of x . Adding the edge contributions significantly improves the approximate methods to calculate forward scattering patterns. The presented method does not give a physical explanation for the resulting edge functions, but leads for some cases to a better approximation for the extinction efficiency, and probably also the near forward scattering, than an earlier presented approximation of the powerful CAM approach.

References

1. H. C. van de Hulst, *Light Scattering by Small Particles*, (Wiley, New York, 1957)2.
2. D. S. Langley and P. L. Marston, "Forward Glory Scattering From Bubbles," *Appl. Opt.* **30**, 3452-3458 (1991).
3. D. S. Langley and M. J. Morrell, "Rainbow Enhanced Forward and Backward Glory Scattering," *Appl. Opt.* **30**, 3459-3467.
4. G. F. Bohren and D. R. Huffman, *Absorption and Scattering by Small Particles*, (Wiley, New York, 1983), Chap. 4, p.82.
5. H. M. Nussenzveig, "High-Frequency Scattering by a Transparent Sphere," *J.Math.Phys.* **10**, 82-125 (1969)
6. H. M. Nussenzveig, "Complex Angular Momentum Theory of the Rainbow and the Glory," *J.Opt.Soc.Am.* **69**, 1068-1079 (1979).
7. H. M. Nussenzveig, *Diffraction Effects in Semiclassical Scattering*, (Cambridge University Press, 1992).
8. T. W. Chen, "High Energy Light Scattering in the Generalized Eikonal Approximation," *Appl. Opt.* **28**, 4096-4102 (1989).
9. T. W. Chen, "Modified P-Q of Light Scattering for Large Size Parameters," *Opt. Lett.* **15**, 461-462 (1990).
10. S. K. Sharma, "On the Validity of the Anomalous Diffraction Approximation," *J. Mod. Opt.* **39**, 2355-2361 (1992).
11. J. Petykiewicz, *Wave Optics*, (Kluwer Academic Publishers, 1992), Chap. 2, p. 53.

Chapter 4. Scattering matrix

4.1. Introduction.

Different particle sizes can be distinguished using the scattering properties of the particles. In a commonly used set-up (Fig.5.1) a parallel laser beam is partly scattered by a large number of particles, contained by a transparent cell. A so called Fourier lens focuses the undisturbed beam on a central detector and the scattered light on the surrounding semi-circular detector elements. A specific direction before the lens corresponds with a specific position on the detector that is located in the focal plane of the lens. The forward or small angle scattering pattern is measured by a number of detectors and may be represented by a vector \mathbf{b} , where each element b_n represents the signal of one detector. The considered size range is divided in a number of size classes, so the required size distribution is also represented by a vector \mathbf{x} , not to be confused with the size parameter x . If it is assumed that the scattered intensities of all individual particles may simply be added, then the discrete size distribution \mathbf{x} and the scattering pattern \mathbf{b} are linearly related via a scattering matrix \mathbf{A}

$$\mathbf{Ax} = \mathbf{b} \quad (4.1)$$

where the columns of \mathbf{A} consist of the discrete scattering patterns of the different size classes. This assumption requires that the light scattered by a particle is not scattered again significantly by other particles, i.e. multiple scattering must be negligible. At the same time the signal/noise ratio for the measured scattering pattern must be high enough. Another requirement for the mentioned assumption is a random relative position for the different scattering particles, so their scattered e.m. fields are incoherent and intensities may be added. The calculated matrix \mathbf{A} and the measured scattering pattern \mathbf{b} lead to the required size distribution \mathbf{x} . In this chapter averaging requirements for the calculation of a scattering matrix are derived by considering the largest contributions to the forward scattering pattern as discussed in Chapter 2.

4.2. Calculation of scattering matrix.

The apparatus used in this work is the "Malvern particle sizer 2600". Its detector consists of $N=31$ semi-rings with diameters approximately divided equidistant on a logarithmic scale, i.e. neighbouring ring diameters differ an approximately constant factor f_n . The n^{th} detector with inner and outer radii R_{ni} and R_{no} receives the light scattered by a particle into a solid angle bounded by $R_{ni} < FL \cdot \sin \vartheta < R_{no}$ and $0 < \varphi < \pi$, where FL is the focal length of the lens. For the calculation of a scattering matrix the total azimuth angle range $0 < \varphi < 2\pi$ is used, and for multiple scattering

calculations the scattering angle intervals are defined to include the insensitive zones between the detectors, because all power must be accounted for.

One column of a scattering matrix A is defined to contain the averaged discrete scattering pattern of a number P of particle sizes for the considered size class. All columns are scaled so they represent scattering patterns of equal geometric cross sections, leading to similar maximum values in each column and an optimal inversion according to Hirleman¹. The n^{th} component of the discrete scattering pattern a of a specific size is given by the integral of the intensity function $i(x, \vartheta) = (i_1 + i_2)/2$, $i_j = |S_j|^2$ for one particle over the solid angle corresponding to the n^{th} detector area divided by the relative geometric cross section πx^2 .

$$a_n(x) = \int_{\vartheta_{ni}}^{\vartheta_{no}} \int_0^{2\pi} \frac{i(x, \vartheta)}{\pi x^2} \sin \vartheta d\varphi d\vartheta, \quad (4.2)$$

where the angle ϑ_{ni} is given by $m_{\text{cell}} \cdot \sin \vartheta_{ni} = \sin(R_{ni}/FL)$, and ϑ_{no} by a corresponding relation, where m_{cell} gives the refractive index of the medium containing the particle relative to the medium outside the cell.

This integral gives the n^{th} component of the discrete scattering vector $c(x)$ for size parameter x . The integration with respect to the azimuth angle φ gives for unpolarized light a factor 2π . An analytical expression for the intensity as function of the angle ϑ is not available for the exact Mie solution, so integration is carried out numerically as follows, using a logarithmic angle scale with K intervals, evaluated at their logarithmic center.

$$a_n(x) = 2 \left(f_n^{1/2K} - f_n^{-1/2K} \right) \sum_{k=1}^K \frac{i(x, \vartheta_k)}{x^2} \vartheta_k \sin \vartheta_k \quad (4.3)$$

where $\vartheta_k = \vartheta_{ni} \cdot f_n^{(k-1/2)/K}$ and $f_n = \vartheta_{no} / \vartheta_{ni}$. For $K=1$ the difference in Eq.4.3 gives the relative angle width for the n^{th} detector $W_n = f_n^{1/2} - f_n^{-1/2} = (\vartheta_{no} - \vartheta_{ni}) / \vartheta_n$ where $\vartheta_n = (\vartheta_{ni} \vartheta_{no})^{1/2}$ is the logarithmic center scattering angle for the n^{th} detector.

The considered size range is divided in $C=45$ size classes with center size values x_c equidistant on a logarithmic scale with subsequent size classes differing a factor $f_x = x_c / x_{c-1}$. Within the range of each size class a discrete scattering pattern b is calculated for a number P of particle sizes, also chosen equidistant on the same logarithmic size scale. The patterns of the sizes in one class are averaged to give the

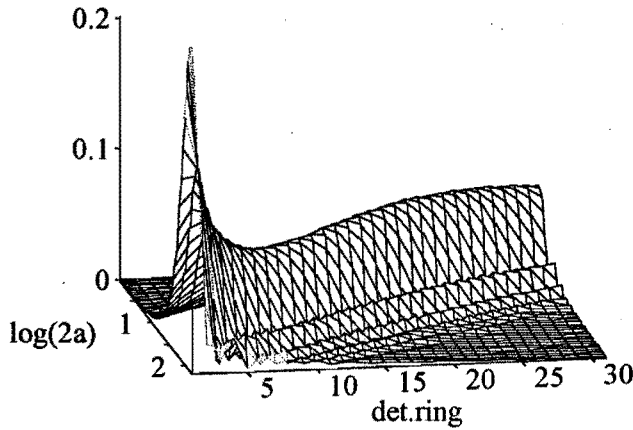


Figure 4.1. Scattering matrix for the detector of the Malvern 2600 with Focal Length = 63mm, considering only Fraunhofer diffraction.

scattering vector of that class, i.e. a column in matrix A . Matrix element A_{cn} for class c from $x = f_x^{-1/2}x_c$ to $x = f_x^{1/2}x_c$ and detector element n is thus calculated according to

$$A_{cn} = \frac{1}{P} \sum_{p=1}^P a_n \left(x_c \cdot f_x^{-1/2 + (p-1/2)/P} \right) \quad (4.4)$$

The values P and K leading to a specified accuracy depend on the ratio of the contributions that are quasi constant or rapidly fluctuating as function of the size parameter x and angle ϑ , as discussed in the following section. Similar to the relative angle width a relative size class width is defined as $W_x = f_x^{1/2} - f_x^{-1/2}$.

4.3. Fraunhofer diffraction

Figure 4.1 shows a scattering matrix for perfectly absorbing particles, i.e. only Fraunhofer diffraction contributes to the scattering pattern. The discrete pattern over 31 detector elements is calculated for $C=45$ classes. The similar scattering pattern for different sizes follows directly by substituting $i = S_{Fth}^2$ (Eq.2.13), $K=1$, $P=1$ and $\sin\vartheta_n = \vartheta_n$ in Eqs.4.3 and 4.4:

$$A_{cn} \cong 2W_n \frac{\vartheta_n^2}{x_c^2} \left(x_c^2 \frac{J_1(x_c \vartheta_n)}{x_c \vartheta_n} \right)^2 = 2W_n J_1^2(x_c \vartheta_n) \quad (4.5)$$

The parameter W_n has for all 31 detectors approximately the same value $W_n=0.12$. For different size parameters x_c the maximum value $J_1^2(1.84)=0.338$ is positioned at different angles ϑ_n , leading to the maximum value $A_{max} = 2W_n J_{1max}^2 \cong 0.08$ on a diagonal of the matrix. Due to the fact that the relative width W_n of the inner circular detectors

deviates from the relative width of the other detectors, the corresponding matrix elements are larger.

4.4. Averaging requirements.

In this section it is shown that the numbers K and P (Eqs.4.3 and 4.4) may be determined by requiring for each matrix element a maximum deviation Err from the exact result for $P \rightarrow \infty$, $K \rightarrow \infty$. Whether the required accuracy is indeed obtained depends on the value of Err and the refractive index as explained at the end of this section.

The difference Err between the exact average of the function $A \sin \omega$ in a small interval $\Delta\omega < \pi$ and the average of N equidistant evaluations ω_i in this interval is limited by $Err < A(\Delta\omega / N)^2 / 24$. For an interval $\Delta\omega > \pi$ the contribution to the difference changes sign if ω increases π , leading to the following error for any interval $\Delta\omega$ and $N > \Delta\omega / \pi$, i.e. every period is evaluated at least twice,

$$Err < \frac{A \cdot \Delta\omega \cdot \text{Min}(\Delta\omega, \pi)}{24 \cdot N^2} \quad (4.6)$$

where the function Min gives the minimum of two values. In order to use this accuracy relation, the different contributions to the scattering pattern are written as the product of a quasi constant and a rapid fluctuating function of x and ϑ .

For the following order of magnitude consideration the Fraunhofer and edge contribution and the two largest GO contributions are considered. The total amplitude function is in two angular regions approximated by

$$\vartheta \ll \gamma: S_{j,\text{tot}} = S_{\text{Frh}} + S_{j,\text{edg}} + S_{j,p=1} \quad (4.7)$$

$$\vartheta \gg \gamma: S_{j,\text{tot}} = S_{\text{Frh}} + S_{j,p=0} + S_{j,p=1} \quad (4.8)$$

where $j=1,2$. The angle γ defined by Nussenzveig³

$$\gamma = (2/x)^{1/3} \quad (4.9)$$

separates the near forward scattering range in a penumbra region $1/x < \vartheta < \gamma$ where the diffraction contribution is larger and a complementary region $\vartheta > \gamma$ where the GO reflection is larger. Near this angle the three amplitude functions S_{Frh} , $S_{j,\text{edg}}$ and $S_{j,p=0}$ have nearly the same magnitude. Both the edge diffraction and the geometrical reflection are less accurate approximations close to this angle. The CAM theory provides better, but more complicated, approximations. For the purpose of this section the small angle approximation is sufficient.

The angle range that is relevant for the dimensions of the mentioned detector lies mainly in the penumbra region, so the intensity function $i(x, \vartheta) = (i_1 + i_2)/2$ is assumed to consist of the following contributions

$$i_j = \text{Re} \left[S_{j,\text{dif}} S_{j,\text{dif}}^* + 2S_{j,\text{dif}} S_{j,p=1}^* \right] + S_{j,p=1} S_{j,p=1}^* \quad (4.10)$$

where

$$S_{j,\text{dif}} = x^2 \frac{J_1(x\vartheta)}{x\vartheta} + 2x \left(T_{3-j} \frac{J_1(x\vartheta)}{x\vartheta} + T_j J_1'(x\vartheta) \right) \quad (4.11)$$

is the sum of the Fraunhofer and the edge diffraction. The difference between polarizations $j=1,2$ is in the rest of this section neglected.

For $x\vartheta > 2.5$ the Bessel function in the combined diffraction amplitude is approximated as $J_1(z) \cong (2/(\pi z))^{1/2} \sin(z - \pi/4)$, containing a quasi constant factor and a rapidly fluctuating factor as function of $z=x\vartheta$. The edge function T is always limited by $|T| < x^{1/3}$ (Chapter 3) leading to the following approximation of the combined diffraction amplitude function

$$S_{\text{dif}} \cong \frac{x}{\vartheta} E \sin(x\vartheta) \quad (4.12)$$

where

$$E(x, \vartheta) = \left(1 + 2 \left(\frac{1}{x} + \vartheta \right) x^{1/3} \right) \cdot \text{Min} \left(0.6, \left(\frac{2}{\pi x \vartheta} \right)^{1/2} \right) \quad (4.13)$$

gives an approximate envelope function and the $\sin(x\vartheta)$ describes the rapidly fluctuating behavior. A constant phase term that is independent of x and ϑ and different for the approximate Bessel function J_1 and its derivative J_1' , is irrelevant for the purpose of this section and is therefore omitted.

The GO $p=1$ contribution is similarly written as the product of a quasi constant and rapidly fluctuating function of x and ϑ ,

$$S_{p=1}(x, \vartheta) = x \cdot G(\vartheta) \cdot e^{i\rho'} \quad (4.14)$$

where $i = \sqrt{-1}$ and a constant phase term in the imaginary exponent is omitted. The function

$$\rho'(x, \vartheta) = 2x \left(1 + m_r^2 - 2m_r \cos(\vartheta/2) \right)^{1/2} \quad (4.15)$$

gives the absolute value of the angle dependent phase delay, i.e. $\rho'(x, 0) = |\rho| = 2x|m-1|$, $m_r = \text{Re}[m]$ and $G(\vartheta) = |S_{p=1}|/x$ is for $\vartheta=0$ given by

$$G(0) = \frac{2 \cdot m^2}{(1+m)^2(m-1)} e^{-\text{Im}[\rho]} \quad (4.16)$$

For $0.525 < m < 3.38$ and $\text{Im}[m]=0$ this small angle transmission $|S_{p=1}|$ is larger than the small angle GO reflection $|S_{p=0}|=x/2$, otherwise the reflection is larger. The three terms of Eq.4.10 lead to the following contributions to a specific scattering matrix element

$$A_{cn} = W_n \cdot i \cdot \vartheta_n^2 x^{-2}$$

$$A_{cn}(\text{dif,dif}) < W_n \cdot E^2(x_c, \vartheta_n) \cdot \frac{1}{2} (1 - \overline{\cos(2x\vartheta)}) \quad (4.17)$$

$$A_{cn}(\text{dif,p=1}) < W_n 2 \cdot E(x_c, \vartheta_n) G(\vartheta_n) \vartheta_n \cdot \overline{\sin(x\vartheta)} e^{i\rho'} \quad (4.18)$$

$$A_{cn}(p=1,p=1) = W_n G^2(\vartheta_n) \vartheta_n^2 \quad (4.19)$$

where the slowly varying functions E and G are both evaluated at the angle ϑ_n for the considered detector and size x_c for the considered size class. The rapidly fluctuating functions need to be properly averaged. The interference contribution will contain sine functions with parameters $x\vartheta + \rho'$ and $x\vartheta - \rho'$. The GO $p=1$ intensity is quasi constant and does not lead to any requirements.

Allowing a maximum deviation Err for the calculation of a matrix element A_{cn} leads according to Eq.4.6 and Eqs.4.17 and 4.18 to the following requirements of P

$$P^2 < \frac{W_n E^2 \cdot \Delta\omega \cdot \text{Min}(\Delta\omega, \pi)}{24 \cdot \text{Err}} \quad (4.20)$$

where $\Delta\omega = 2x_c \vartheta_n W_x$ and $P > \Delta\omega / \pi$ must also be satisfied, and

$$P^2 < \frac{W_n 2 \cdot E \cdot G \cdot \Delta\omega \cdot \text{Min}(\Delta\omega, \pi)}{24 \cdot \text{Err}} \quad (4.21)$$

where $\Delta\omega = (x_c \vartheta_n + \rho') W_x$ and $P > \Delta\omega / \pi$ must also be satisfied. In a Mie algorithm the entire scattering pattern for a specific size parameter x is usually determined at once, so the largest number P resulting from Eqs.4.20 and 4.21 for all detector elements is used to calculate the matrix elements A_{cn} for all detectors $n=1-N$.

The averaging requirement for the number of angles K per detector is found by replacing in Eqs. 4.20 and 4.21 P is by K and using in these equations phase differences $\Delta\omega = 2x_c \vartheta_n W_n$ and $\Delta\omega = (x_c \vartheta_n + d\rho'/d\vartheta) W_n = (1 + (m_r / \rho')) \sin(\vartheta_n / 2) x_c \vartheta_n W_n$, respectively.

For $m \rightarrow 1$ the $p=1$ contribution will become higher and less wide, being exactly opposite to the Fraunhofer peak for $m=1$, i.e. the GO approximation that gives for $m=1$ a delta peak cannot be used. The $p=1$ contribution is significantly diffracted for $|\rho| < 1$ and the resulting matrix elements are found to be limited by

$$A_{cn} < W_n \cdot \rho \left(\frac{x_c \vartheta_n}{3} + E(x_c, \vartheta_n) \right)^2 \frac{1}{2} (1 - \overline{\cos(2x\vartheta)}) \quad (4.22)$$

The first term results from the small angle Rayleigh-Gans scattering or the imaginary component of the Anomalous Diffraction⁴, that is valid for $\rho \rightarrow 0$. The second term accounts for the substantial Fraunhofer and edge diffraction for $\rho = 1$ that becomes smaller for decreasing ρ due to the opposite phase of the $\rho = 1$ diffraction. This is really the only motivation for Eq.4.22. A more severe limitation for $\rho \cong 0$ could be formulated by using the series for $\rho < 1$ and $\rho > 1$ by van de Hulst⁴ for the Anomalous Diffraction.

The glory contributions are not included in this section. This may lead to less accurate calculation of the scattering matrix then according to Eqs. 4.20 and 4.21. The resulting deviation depends on the amplitude and the fluctuating behavior of these glory contributions as function of the size parameter x . For $m < 1$ the largest forward glory contributions do not cross the symmetry axis ($L = 0$) and travel only a relative short distance through the sphere, i.e. their phases change only slowly as function of x , and their contributions are evaluated sufficiently by Eqs. 4.20 and 4.21. The forward glory rays that cross the axis twice or more ($L = 2, 4, \dots$) travel a relatively large distance through the sphere. The resulting rapid fluctuations as function of x are not sufficiently evaluated by Eqs. 4.20 and 4.21. The resulting intensity contribution are however very small, and the values P and K as given by Eqs. 4.20 and 4.21 lead for $m < 1$ to the indicated maximum deviation if $\text{Err} > A_{\max} 10^{-5}$.

For $m > 1$ only glory rays exist for $L > 0$ that contrary to $m < 1$ may also have a rainbow condition (section 3.3), leading to a relatively large amplitude. For $m > 1$ the deviation for a matrix calculated using the given values for P and K and the exact Mie solution only remains below the chosen maximum deviation if $\text{Err} > A_{\max} 10^{-2}$. To obtain a better scattering matrix, larger values of P and K should be used, or better, the approximation for these rays may be incorporated in the requirements for P and K .

The intensity of a glory ray doesn't lead to large errors, the errors are mainly due to coincidental evaluations at x, ϑ values where positive interference of a glory ray and either the Fraunhofer or the GO $\rho = 1$ contribution occurs.

4.5. GO approximation.

For large enough size parameter x the GO approximation (Eq.4.10) may lead to a sufficiently accurate intensity function $i = (S_1^2 + S_2^2) / 2$ and scattering matrix A , using the already given numbers P and K for sufficient evaluations. For $m < 1$ the glory contributions for $L = 0$ must be included. For $m > 1$ it is advantageous to omit the glory contribution for the reason mentioned in the previous section. Rainbow enhanced glory

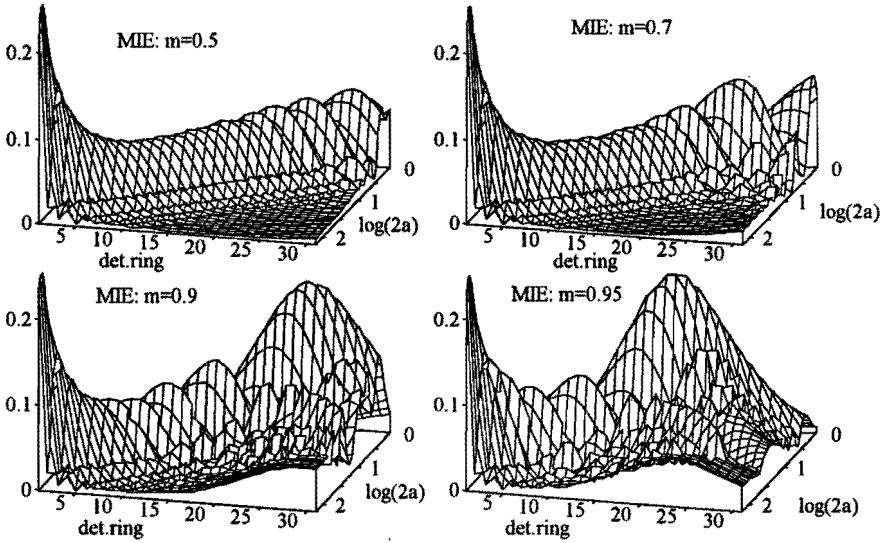


Figure 4.2. For m approaching 1 the $p=1$ contribution becomes increasingly important, leading to larger deviations from the Fraunhofer scattering matrix (Fig.1)

contribution⁵ that occur for $m=1.250$, $m=1.465$ and less important ones for other specific values of m , are exceptions and require better approximations. For moderate values of x near forward rainbows for m close to both mentioned values are also important due to diffraction³.

For cases ($m > 1$) where glory contributions are not important the following conditions lead to a very fast calculation of the scattering matrix elements. Equation 4.17 indicates that for the condition

$$\frac{W_n E^2}{x_c \vartheta_n \text{Min}(W_x, W_n)} < \text{Err} \tag{4.23}$$

the fluctuating part of the diffraction contribution may be neglected. Equation 4.18 shows similarly that the interference of the diffraction and the GO $p=1$ ray may be neglected if

$$\frac{W_n 2 \cdot E \cdot G \cdot \vartheta_n}{\text{Min}((x_c \vartheta_n + \rho') W_x, (x_c + d\rho'/d\vartheta) \vartheta_n W_n)} < \text{Err} \tag{4.24}$$

If both conditions are satisfied then the scattering matrix element A_{cn} may be approximated by

$$\frac{A_{cn}}{W_n} = \frac{1}{\pi x_c \vartheta_n} \left(1 + 4 \frac{\text{Re}[T_1 + T_2]}{x_c} + 4 \vartheta_n^2 (|T_1|^2 + |T_2|^2) \right) + G^2 \vartheta_n^2 \tag{4.25}$$

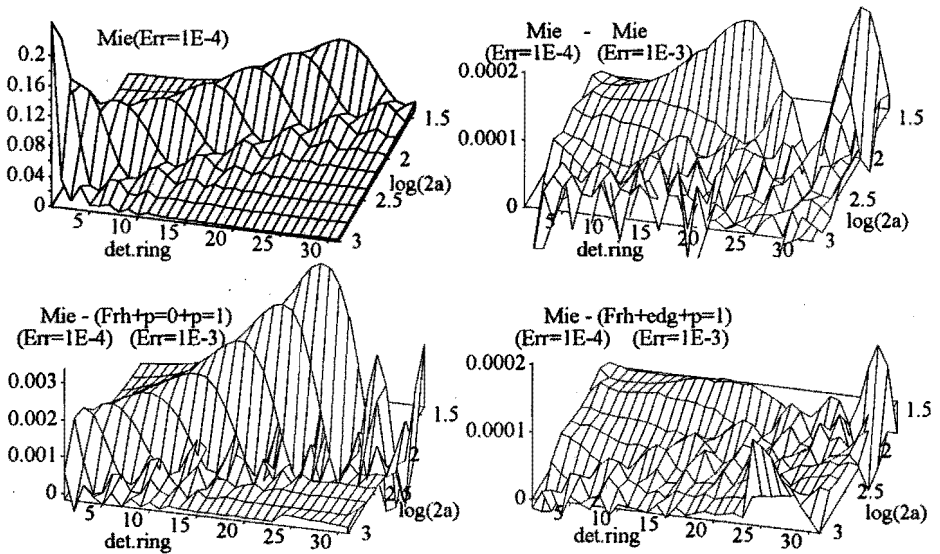


Figure 4.3. Comparison between matrices calculated for the Malvern 2600 detector, $m=1.33$ and Focal Length=300mm.

where the smallest contributions are neglected. This approximation is only accurate for very large size parameters x .

4.6. Results.

Figure 4.2 shows the effect of the $p=1$ contribution on the Fraunhofer dominated scattering matrix for $m \rightarrow 1$. The matrices are calculated using the Mie algorithm by Bohren and Huffman⁵ and P and K values according to Eqs.4.20 and 4.21 with $\text{Err} = 10^{-2}$. For $m=0.5$ the $p=1$ contribution is smaller than the reflection, leading approximately to the Fraunhofer matrix with a small large angle contribution due to both edge reflection and $p=1$ contribution and an x dependent maximum value due to interference of the Fraunhofer and the $p=1$ contribution. For $m=0.7$ and $m=0.9$ both effects are increased, while for $m=0.95$ the width of the $p=1$ contribution is approaching the width of the detector. The large oscillations at the largest angles are due to the glory contributions. For $m > 1$ a similar effect of the $p=1$ contribution occurs with less oscillations at large angles for m near 1.

Figure 4.3 shows an "exact" matrix for $m=1.33$, Focal Length=300 (for measuring larger particles) calculated using the Mie algorithm and P and K values according to Eqs. 4.20 and 4.21. with $\text{Err} = 10^{-4}$, and the difference with three other matrices. Only scattering patterns for one out of four size classes is calculated and only $2a > 31\mu\text{m}$ ($\lambda = 0.6328\mu\text{m}, x > 150$) is considered. The required calculation times on a MS-DOS

486DX 33Mhz computer are for the Mie calculation and $\text{Err} = 10^{-4}$ 20 hours, for the Mie calculation and $\text{Err} = 10^{-3}$ 5 hours, while the approximation with $\text{Err} = 10^{-3}$ with or without the edge contribution only requires 2 minutes. In the lower left matrix of Fig.4.3 the edge contribution is not subtracted from the 'exact' matrix, and can be seen to decrease as x increases. In the considered size range it significantly improves the accuracy for calculating forward scattering patterns using the GO approximation.

For $m < 1$, including also the largest glory contributions in Eq.4.10, the accuracies for the approximation as shown in Fig.4.3 are only obtained well inside the penumbra region, i.e. $\vartheta \ll \gamma$. The assumption of an edge contribution coming from an infinitely small edge range is for $m < 1$ and $\vartheta \geq \gamma$ probably insufficient due to the Goose Hanchen effect or inaccurate glory contributions. The calculation times for sufficiently accurate Mie calculations are smaller then required for $m > 1$.

references

1. Hirleman, E. D., p.135 and 159 in *Optical particle sizing/ Theory and Practice, Proceedings of an international symposium* ,Eds. Gouesbet, G. and Grehan, G., (Plenum Press New York 1988).
2. Bayvel, L. P. idem p.311.
3. H. M. Nussenzveig, *Diffraction Effects in Semiclassical Scattering*, (Cambridge University Press, 1992).
4. H. C. van de Hulst, *Light Scattering by Small Particles*, (Wiley New York 1957).
5. D. S. Langley and M. J. Morrell, "Rainbow Enhanced Forward and Backward Glory Scattering," *Appl. Opt.* **30**, 3459-3467 (1991).
6. Bohren, C. F. and Huffman, D. R., *Absorption and scattering of light by small particles*. (Wiley, New York 1983).

Chapter 5. Particle sizing

An experimental method is presented to determine drop size distributions (2-100 μm) in a water-in-oil emulsion during electric field enhanced coalescence. A standard small angle or forward scattering measurement set-up is equipped with a special cell allowing an electric field up to 3.6 kV/cm. Tested emulsions are free from surfactants and contain only a small fraction of the electrically conducting dispersed phase. Drop size distributions are calculated accounting for multiple scattering using a series of thin single scattering slabs, which each linearly redistribute a discrete axisymmetric forward scattering pattern. An estimated single scattering pattern and the resulting size distribution are modified until the calculated multiple scattering pattern is nearly equal to the measured scattering pattern.

5.1. Introduction.

In order to verify the calculated evolution of a drop size distribution during electrostatic coalescence as presented in Chapter 7, a commonly used forward scattering measurement set-up (Malvern particle sizer model 2600) is equipped with a special transparent cell to measure drop size distributions of water in kerosene emulsions (Fig.5.1). The content of the cell may be submitted to an electric field up to 3.6 kV/cm. An unpolarized parallel laser beam is partly scattered by water drops in the emulsion, and the small angle or forward scattering pattern is measured by 31 coaxial semi-circular detector elements. Earlier results for the measurement of size distributions during electric field enhanced coalescence were presented by Williams and Bailey¹ and van den Bosch².

In this work multiple scattering accounts for light that is scattered more than once and only the far field solution for scattering by spheres is used. The scattering medium is divided into a number of thin slabs perpendicular to the laser beam, so in each slab multiple scattering is negligible. The discrete scattering pattern leaving a slab is linearly related to the entering scattering pattern by a redistribution matrix. The scattering pattern entering the cell is modified by each slab, leading to the multiple scattering pattern at the end of the cell. The single scattering pattern for one slab, and thus also the redistribution matrix is adjusted until the calculated multiple scattering pattern matches the measured scattering pattern.

Other authors have presented inversion methods for multiple scattering data. Hirleman³ uses the same discrete axisymmetric scattering angles, referred to as discrete ordinates, but like van de Hulst⁴ he considers scattering orders, instead of a

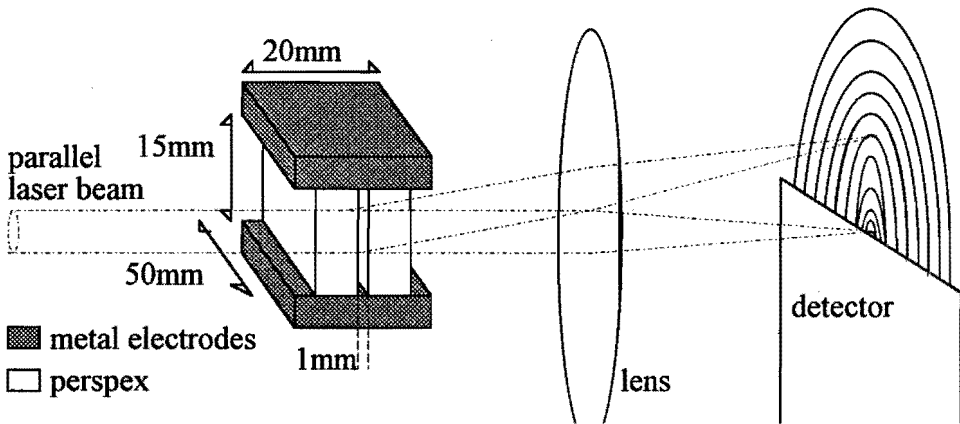


Figure 5.1. Schematic drawing of experimental set-up. The sample cell may be rotated around the optical axis, so both a vertical and a horizontal electric field may be applied.

series of thin single scattering slabs. Besides a suggestion for an iterative scheme as used in this work, Hirleman⁵ also proposes a much more extended measuring method to obtain the total redistribution matrix. More independent scattering properties are measured and a higher degree of multiple scattering may probably still be inverted to a reliable size distribution. Gomi⁶ uses a discrete ordinate approach and a series of single scattering slabs, as is done in this work, but he only considers very large particles allowing a Fraunhofer approximation. Both Hirleman and Gomi use a small angle approximation for the relations between incident solid angles, scattering solid angles, and resulting solid angles, whereas this work allows all angles for these geometrical relations. Schnablegger⁷ uses a multiple scattering order method presented by Hartel⁸ to obtain submicron-size distributions from large angle multiple scattering data, measured in a cylindrical sample cell. This method uses the expansion of a single scattering pattern in Legendre polynomials, leading to an analytical relation for multiple scattering. Although this method could be used for the situation presented here, it would require a relatively huge calculation capacity due to the large considered size range.

5.2. Experimental set-up

The apparatus used for the light scattering measurements is a Malvern particle sizer model 2600. It consists of a 2 mW He-Ne laser source ($\lambda = 632.8\text{nm}$), a beam expander (leading to a beam width of 8mm), a sample cell containing the scattering particles and a lens to focus the undisturbed laser beam onto a central detector and the scattered light onto 31 concentric semi-circular detectors (Fig.5.1), with radii on an approximately logarithmic scale³. The detector dimensions and the focal length of the

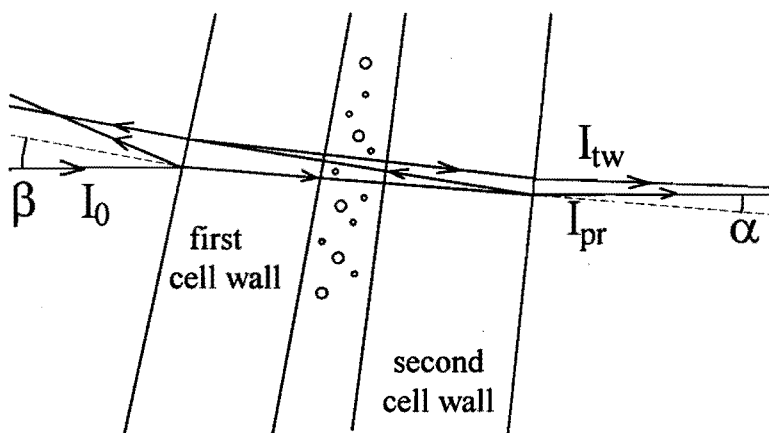


Figure 5.2. If the angle β between the incident beam I_0 and the normal to the first cell wall is larger than the angle α between the transmitted beam I_{pr} and the normal to the second cell wall, then the twice reflected ray I_{tw} is directed downwards relative to the directly transmitted ray I_{pr} . The angles are exaggerated.

lens (63mm) allow particles with radii ranging from $a \approx 0.7$ to $a \approx 70$ to be distinguished. The sample cell consists of two thick metal plates serving as electrodes, and two side walls for the laser beam to pass through. The two small remaining walls are also made of perspex. The dimensions of the cell content are $1 \times 15 \times 40 \text{ mm}^3$. To limit the amount of multiple scattering, the illuminated length is only $d = 1 \text{ mm}$ ($\pm 2\%$), i.e. the laser beam only travels through 1mm of emulsion. The electrodes are 20 mm wide and the distance d between the electrodes is 15 mm. This configuration gives an acceptable parallel electric field inside the cell. The maximum allowed voltage $V_{\text{eff}} = 5.5 \text{ kV}$ (a.c. 50Hz) leads to an effective electric field $E_{\text{eff}} = V_{\text{eff}} / d = 3.6 \text{ kV/cm}$.

The kerosene was first contacted with water in order to remove surfactants and left to settle. The emulsions used for the experiments were prepared by mixing this "cleaned" kerosene with 0.1% demi water in an ultrasonic bath. After some minutes, during which the largest drops settled a certain distance, the remaining upper layer could be introduced into the sample cell using a pipet. Microscopic video-recordings of the same cell and an a.c. field showed that for this case approaching drops coalesced instantaneously at contact. If the surfactant Span 80 was added, chain formation as observed earlier could be seen. A problem of this experimental set-up is the attachment of drops to the transparent side walls, resulting in an unwanted scattering pattern. Perspex is used because unlike glass it is hydrophobic in a kerosene environment, so less drops attach to the wall. Microscopic video-recordings of the same cell with a d.c.

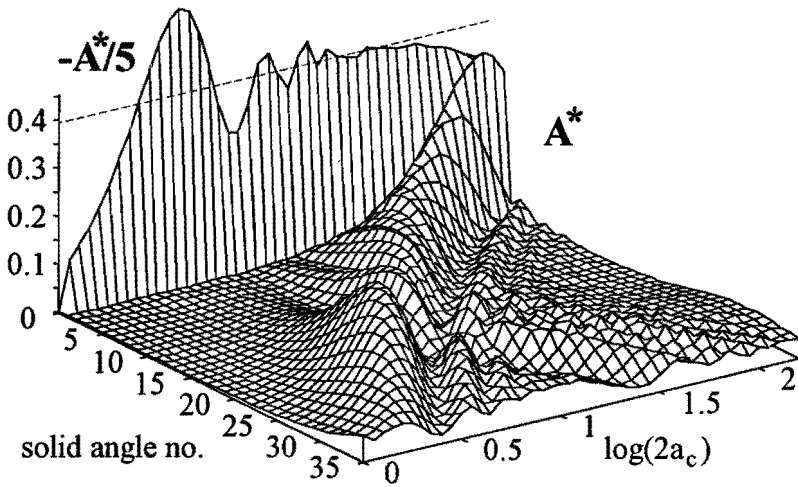


Figure 5.3. Scattering matrix A^ for water drops ($n = 1.333$) in kerosene ($n = 1.43$). The discrete solid angles correspond with the values in table 1, and the drop radii range from $a_1 = 1\mu\text{m}$ to $a_{45} \approx 160\mu\text{m}$. For solid angle no. 0 $-A^*_{0,i}/5$ instead of $A^*_{0,i}$ is shown.*

field instead of an a.c. field show that lots of probably charged drops attach to the perspex walls, making usable light scattering experiments impossible for the d.c. field case.

The angles of the cell walls with respect to the laser beam must be as indicated in Fig.5.2. The central detector is the focus point for all unscattered laser light and will act as a secondary light source. The second cell wall should not reflect the light of this secondary source upwards, to one of the semi-circular detectors, and is thus inclined with the indicated angle α . The reflection by the second cell wall of the primary beam is therefor necessarily upward. To prevent the subsequent reflection by the first cell wall from reaching one of the semi-circular detectors, the first cell wall must be inclined as indicated with $\beta > \alpha$. Both angles of the cell walls can be determined using the reflections of the primary beam on the laser source housing, and were set to approximately $\alpha = 0.02\text{rad}$. and $\beta = 0.04\text{rad}$. The angle between the sides of one cell wall is usually much smaller. Moreover, the reflection by the interface between air and perspex wall with relative refractive index 1.5 is much larger than the reflection by the interface between wall and kerosene with relative refractive index $1.5/1.43$. The latter reflection is neglected.

The intensity of the undisturbed twice reflected beam, traveling towards the detector, is given by $I_{\text{tw}} = I_{\text{pr}} \cdot |r|^4$, where $I_{\text{pr}} = I_0 \cdot (1 - |r|^2)^2$ is the intensity of the undisturbed primary beam beyond the cell, and $r = (m_w - 1)/(m_w + 1)$ is the reflection coefficient

for the interface between air and the cell wall. For $m_w=1.5$ this leads to $I_{tw} \cong I_{pr} \cdot 10^{-3}$. This twice reflected beam travels three times through the scattering medium and, contrary to the beam itself, the corresponding scattered light does reach the detectors. The intensity of this scattered light is approximately $3 \cdot I_{tw} / I_{pr} \approx 0.005$ times the direct scattering pattern for single scattering and has the same angle deviation as the secondary beam. This contribution is very small compared to direct scattering, and is also neglected.

If for a specific plane of incidence the laser beam makes an angle α_0 with the normal to the second cell wall, then the relation of the scattering angle ϑ inside the cell and the corresponding angle ϑ_0 outside the cell in this plane is given by:

$$m_{cel} \sin(\alpha + \vartheta) = \sin(\alpha_0 + \vartheta_0),$$

where $m_{cel} \cdot \sin \alpha = \sin \alpha_0$ and $m_{cel} = n_i / n_o$ is the refractive index ratio of the inside and outside medium, and the second cell wall interfaces are assumed to be parallel. For the matrix calculation of chapter 3 the scattering angle ϑ' that corresponds with the outside angle ϑ_0 is calculated according to $m_{cel} \sin \vartheta' = \sin \vartheta_0$ leading to a small error. The relative error $1 - \vartheta'/\vartheta$ in the considered plane of incidence is for the outer detector of the order of 10^{-3} and is negligible compared to the multiple scattering error. For the normal plane the value of $1 - \vartheta'/\vartheta$ is even smaller.

5.3. Single scattering inversion

If multiple scattering is neglected, a discrete size distribution \mathbf{x} may be derived from a discrete measured scattering pattern \mathbf{b} and a known scattering matrix \mathbf{A} as calculated in Chapter 4 by minimizing the expression

$$\begin{bmatrix} \mathbf{A} \\ \alpha \mathbf{H} \end{bmatrix} \mathbf{x} - \begin{bmatrix} \mathbf{b} \\ \mathbf{0} \end{bmatrix} \approx \mathbf{0} \quad (5.1)$$

where the scalar α and matrix

$$\mathbf{H} = \begin{bmatrix} -1 & 2 & -1 & 0 & \dots & 0 \\ 0 & -1 & 2 & -1 & \dots & \dots \\ \dots & \dots & \dots & \dots & \dots & 0 \\ 0 & \dots & 0 & -1 & 2 & -1 \end{bmatrix}$$

provide an adjustable smoothing constraint. An algorithm by Lawson and Hanson⁹ is used to determine \mathbf{x} constrained by $x_c \geq 0$. The dimensionless size distribution \mathbf{x} gives the relative cross section per size category $x_c = n_c d \pi a_c^2$, where n_c is the number density, d is the illuminated length and a_c is the drop radius. Matrix element $A_{i,d}$ gives the fraction of the incident power scattered towards a solid angle i corresponding with detector number i for $x_c = \delta_{cd}$ (Kronecker delta). The element b_i gives the fraction of the incident power scattered to solid angle i by the entire size distribution. The central

solid angle corresponding with the central detector is not used in the inversion according to Eq.5.1. In commercial measurement set-ups like this, the vector \mathbf{b} contains a constant that depends on the reflections by the cell walls, that are used for a specific measurement. The central detector signal is used to measure the obscuration of the central beam due to the scattering particles. This obscuration is used after the inversion to scale the size distribution \mathbf{x} .

If both terms of Eq.5.1 are multiplied by the transpose of the combined matrix of the first term, a smaller inversion is found (Twomey¹⁰). Due to the rather complex nature of the scattering matrix required for our system (fig.5.3), better results are obtained if this latter step is omitted.

The number of size categories used in this work is 45, the center value for the first category is $a_1 = 1\mu\text{m}$ while $a_c = a_{c-1} \cdot 10^{1/20}$, i.e. 20 categories per decade are defined. The scattering matrix is calculated according to the exact Mie solution for scattering by spheres using an algorithm by Bohren and Huffman¹¹ and sufficient averaging ($\text{Err} = 10^{-4}$, Chapter 3).

5.4. Redistribution matrix

The near forward angle range is divided in a number of discrete intervals. All intervals, i.e. solid angles, are separated by axisymmetrical conical surfaces around the beam axis, at angles on an approximately logarithmic scale. The intervals 1-31 correspond with the detectors of the Malvern particle sizer 2600, using a lens with a focal length of 63mm, and taking into account the refractive index of the cell fluid. On a logarithmic scale the insensitive zone between two detectors is equally divided between the adjacent intervals, while intervals 1 and 31 are similarly extended on both sides. Eight extra intervals are added at the large angle side, on a logarithmic scale equal to interval 31, and the central interval 0 is the remainder below interval 1. This amounts for our system to $1+31+8=40$ discrete angular intervals, covering the entire central angle range $\vartheta < 0.39$. Light scattered towards larger angles and then scattered back into the considered angle range is neglected. Table 1 shows all upper angles θ_i , while the (logarithmic) center angles are given by $\vartheta_i = \sqrt{\theta_{i-1}\theta_i}$, except for interval 0 for which center angle $\vartheta_0 = 0$. It is pointless to define more than one interval below interval 1, because the laser beam is only focussed well enough to satisfy $\vartheta < \theta_0$. Equation 5.1 only considers solid angles 1-31.

0	0.00152	10	0.0144	20	0.0499	30	0.155
1	0.00260	11	0.0163	21	0.0563	31	0.172
2	0.00370	12	0.0185	22	0.0635	32	0.191
3	0.00480	13	0.0209	23	0.0715	33	0.211
4	0.00592	14	0.0237	24	0.0804	34	0.234
5	0.00710	15	0.0269	25	0.0902	35	0.259
6	0.00834	16	0.0304	26	0.1011	36	0.287
7	0.00967	17	0.0344	27	0.1130	37	0.318
8	0.01110	18	0.0390	28	0.1261	38	0.352
9	0.01267	19	0.0441	29	0.1403	39	0.390

Table 5.1. The upper angles θ_i of the 40 considered axisymmetric solid angles. The angles 0-31 are based on the detector of the Malvern particle sizer 2600, and a lens with a focal length of 63mm.

Multiple scattering leads to a pattern that scatters more light on the outer detectors than the corresponding single scattering pattern. The maximum value in a specific single scattering pattern is shifted towards larger angles, and if multiple scattering is not accounted for in the inversion of a measured pattern the measured particle sizes are shifted towards smaller values.

If multiple scattering is not negligible then the scattering medium is divided in a number of single scattering slabs, parallel to the transparent cell walls, that one after another redistribute a forward directed scattering pattern. The unscattered incident laser beam is represented by a vector $\mathbf{b}_0 = [1, 0, \dots, 0]$, i.e. all power is incident at the central solid angle $\vartheta < \theta_0$. A single scattering slab redistributes the incident power over all considered solid angles, i.e. vector \mathbf{b}_0 is redistributed to vector \mathbf{b}_1 , for which $\sum_j b_{1,j} \leq 1$ because some power is scattered outside the outer solid angle. The resulting power vector \mathbf{b}_1 is by the following single scattering slab redistributed to a vector \mathbf{b}_2 . This second redistribution is more complicated because \mathbf{b}_1 contains non-zero power fractions in off-axis solid angles, etc. The linear redistribution from \mathbf{b}_0 to \mathbf{b}_1 by the first single scattering slab, containing a size distribution \mathbf{x} , is given by

$$\mathbf{b}_1 = \mathbf{b}_0 + \mathbf{b}_s \quad (5.2)$$

$$b_{s,j} = \sum_c A^*_{j,c} x_c \quad A^*_{j,c} = A_{j,c} - \delta_{0,j} Q_{\text{ext},c} \quad (5.3)$$

where $\delta_{i,j}$ is the Kronecker delta. Matrix \mathbf{A} and the vectors \mathbf{b} consider power scattered to all solid angles 0-39. In Eq.5.1 the same matrix is used, but only the elements corresponding with the solid angles 1-31. Matrix \mathbf{A}^* also accounts for the extinction efficiency $Q_{\text{ext},c}$, so $A^*_{0,c} < 0$, $b_{s,0} < 0$. A simple check for the matrix elements is

possible for the theoretical case size that for a class c only Fraunhofer diffraction contributes and all power remains completely in the considered angular range, then $\sum_j A_{j,c} = 1$ or $\sum_j A_{j,c}^* = -1$. If reflection and/or transmission also contribute significantly then the scattering patterns for larger particles satisfy $\sum_j A_{j,c+1}^* \approx \sum_j A_{j,c}^*$. Figure 5.3 shows the scattering matrix A^* for water drops in kerosene as used in the experiments. The first column is for small particles virtually equal to $-Q_{\text{ext},c}$, while due to the relative large scattering towards interval 0 for larger particles $-A_{0,c}^*$ may be interpreted as a decreased measurable extinction efficiency. The linear modification \mathbf{b}_s of the incident power vector \mathbf{b}_0 is equal to \mathbf{b}_1 for all off-axis solid angles, and may be considered as the result of single scattering if $|\mathbf{b}_s| \ll 1$ i.e. $|\mathbf{x}| \ll 1$.

A single scattering slab m redistributes the entering light power vector \mathbf{b}_{m-1} linearly to a vector \mathbf{b}_m as follows

$$\mathbf{b}_{m,k} = \sum_i R_{k,i} \mathbf{b}_{m-1,i} \quad (5.4)$$

The redistribution matrix \mathbf{R} is given by

$$R_{k,i} = \delta_{k,i} + \sum_j \left(\frac{G_{i,j,k} b_{s,j}}{\cos \vartheta_i} \right) \quad (5.5)$$

which depends on the linear effects of one slab, given by \mathbf{b}_s , and a function G which relates incident, scattering and resulting solid angles (indices i,j,k , respectively) as shown in the appendix. The factor $\cos \vartheta_i$ accounts for the longer path in a slab of already scattered light. Using $b_{0,i} = \delta_{0,i}$ and $G_{0,j,k} = \delta_{j,k}$ (appendix) it may be verified that $\mathbf{b}_{1,k} = \sum_i R_{k,i} b_{0,i}$ correctly leads to $\mathbf{b}_{1,k} = R_{k,0} = \delta_{k,0} + b_{s,k}$ in accordance with Eq.5.2.

5.5. Iterative multiple scattering inversion

Two scattering vectors are separately measured to determine a particle size distribution. First a background signal, proportional to \mathbf{b}_{bg} , is measured while the sample cell only contains the continuous phase without scattering particles, and is mainly due to scattering of the laser beam by scratches on the cell walls. Then the particles are introduced into the cell and a scattering signal, proportional to \mathbf{b}_{sc} , is measured. Both measured vectors are enlarged to account for the power scattered towards the insensitive zones between the detectors. The relative increase is not exactly the same for all detectors or solid angles. Background contributions that do not originate from the laser source are simply subtracted from both measurements, and are not considered here. Due to imperfect focusing of the laser beam, the components

$b_{bg,0}$ and $b_{sc,0}$ are used separately from the rest of the vectors \mathbf{b}_{bg} and \mathbf{b}_{sc} . If in this section a deviating equation applies for the central solid angle, this should be obvious.

Both cell walls are assumed to contribute equally to the background signal, and scattering by one cell wall is assumed to be accurately described by a single scattering vector $\mathbf{b}_w = \mathbf{b}_{bg} / 2$. The values for the outer angular solid angles $j > 31$ are chosen equal to the last measured value $b_{w,j} = b_{w,31}$. The scattering on the first arbitrarily chosen 25 rings is assumed to be due to Fraunhofer diffraction, leading to a removal of twice this power from the central laser beam, $b_{w,0} = -2\sum_{j=1}^{25} b_{w,j}$

The scattering medium is divided in M single scattering slabs for which multiple scattering is negligible, and a first estimate for the single scattering pattern (1-31) is given by

$$\mathbf{b}_s = \frac{\mathbf{b}_{sc} - \mathbf{b}_{bg} b_{sc,0}/b_{bg,0}}{M} \quad (5.6)$$

The measured background pattern is not subtracted entirely from the measured total scattering pattern, but only a fraction $b_{sc,0}/b_{bg,0}$, because it is assumed that the background contribution during the measurement of the scattering pattern is diminished as the central beam. The number of slabs M is chosen such that the transmittance (<1) for one slab satisfies

$$1 + b_{s,0} = \left(\frac{b_{sc,0}}{b_{bg,0}} \right)^{1/M} > 0.99. \quad (5.7)$$

i.e. $-0.01 < b_{s,0} < 0$. The size distribution \mathbf{x}_s may be derived from \mathbf{b}_s according to Eq.5.1, using only the elements of \mathbf{b}_s and \mathbf{A} corresponding with solid angles 1-31. If the measured vectors \mathbf{b}_{sc} and \mathbf{b}_{bg} are not scaled according to section 5.3 then the equation describing the transmittance for one slab

$$1 + b_{s,0} = \exp \sum_c \mathbf{A}_{0,c}^* \mathbf{x}_{s,c} \quad (5.8)$$

is used to scale \mathbf{x}_s and accordingly the vectors \mathbf{b}_{sc} , \mathbf{b}_{bg} and \mathbf{b}_w . In our continuous measurement series this is only necessary for the first measurement, while the following measured vectors \mathbf{b}_{sc} are scaled with the same factor. The value of \mathbf{x}_s leads to a scattering pattern $\mathbf{b}_x = \mathbf{A}^* \mathbf{x}_s$ (0-39), and to a redistribution matrix \mathbf{R}_x using $\mathbf{b}_s = \mathbf{b}_x$ and Eq.5.5. Scattering pattern \mathbf{b}_w leads similarly to a redistribution matrix \mathbf{R}_w . A fraction $1/M$ of the (smoothed) difference between the scaled measured scattering pattern and the pattern according to the $1+M+1$ redistributions of the incident scattering pattern $\mathbf{b}_0 = [1, 0, \dots, 0]$

$$\Delta \mathbf{b} = \mathbf{b}_{sc} - \mathbf{R}_w \mathbf{R}_x^M \mathbf{R}_w \mathbf{b}_0 \quad (5.9)$$

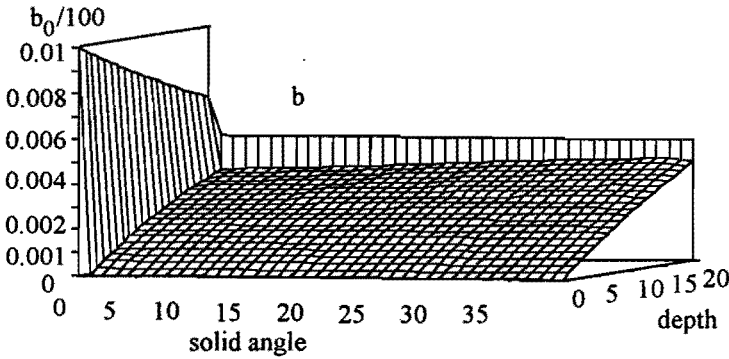


Figure 5.4. Development of multiple scattering pattern b for 20 redistributions of a flat single scattering pattern. The total single scattering pattern is also shown. The center value b_0 is divided by 100.

is added to the estimated single scattering pattern b_s , leading to a new size distribution x_s , a new scaling, new redistribution matrices and new Δb . This procedure may be repeated until $|\Delta b|/|b_{sc}|$ is small enough or minimal. For transmittances below 0.8 a larger fraction of Δb or other modifications of the estimated single scattering may be used. The resulting volume fraction for each size class is given by $v_c = n_c 4\pi a_c^3 / 3 = (4/3)x_c a_c M/d$, using the illuminated length per slab d/M . The size distribution may be represented as a function $g(\ln a_c) = v_c / \ln(a_c/a_{c-1})$ according to Rogers and Davis¹² that is independent of the discretization and satisfies

$$\int_0^{\infty} g(\ln a) d \ln a = \phi, \quad (5.10)$$

where ϕ is the total fraction of water.

Figure 5.4 shows an example of the development of a multiple scattering pattern, for 20 redistributions of a flat single scattering pattern and total extinction $Q_{ext}=0.3$, i.e. $b_{1,0}=\exp(\ln(0.7)/20)$. It is assumed that 70% of the scattered power is equally divided among the 39 non-central solid angles, i.e. $b_{1,j>0}=0.7(1-b_{1,0})/39$. Scattering by cell walls is not considered in this example. Multiple scattering pattern leads to more large angle scattering than the corresponding single scattering pattern. If multiple scattering is neglected a larger single scattering pattern is found due to the fact that extinction of the scattered light is not accounted for. The outer multiple scattering signal is slightly diminished due to the fact that light scattered outside and then back into the considered angle range is neglected.

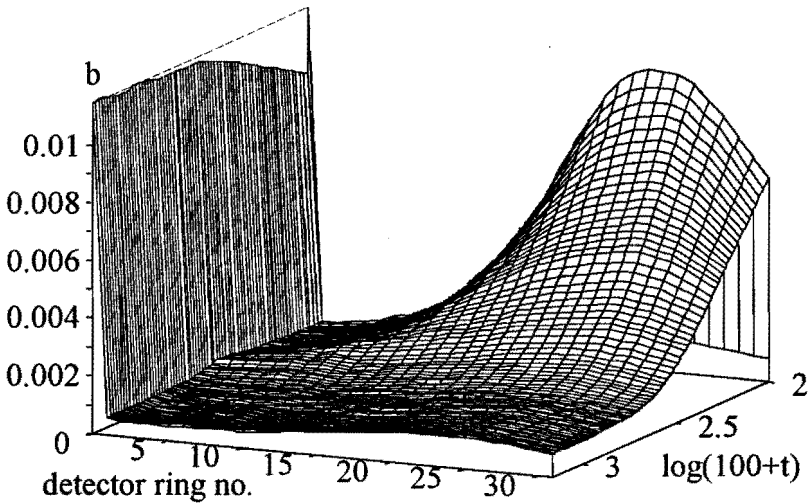


Figure 5.5. Measured discrete light scattering patterns as function of $\log(100+t)$, where t gives the time in seconds from the start of the coalescence process. This time scale distributes the relative changes better over the corresponding axis. The patterns are not scaled to represent fraction of the incident power.

5.6. Results

Figure 5.5 shows an example of the measured discrete scattering pattern of water drops in kerosene as function of time if a horizontal effective electric field of 3kV/cm is applied. One measurement is the average signal over two seconds. The pattern, including the central detector signal, is not scaled according to section 5.3. The power of our laser source fluctuated slowly with a few per cent amplitude and a period of approximately 3 minutes, as shown by the last part of the central detector signal in Fig.5.5.

The last shown pattern b_{end} is nearly equal to the background pattern b_{bg} , partly visible in Fig.5.5, which was measured before the emulsion was entered into the cell while the cell contained clear kerosene. If corrected for the laser instability the difference is given by $|b_{\text{end}} - b_{\text{bg}}| / |b_{\text{bg}}| < 10^{-2}$. The time required for removing the clear kerosene and entering the emulsion was less than 5 seconds. Turning on the electric potential and starting the measurement series was done within a second. The change of the laser power during the time between background and first measurement is neglected. These times are relatively short compared to the entire monitored process and it is assumed that the process starts with a homogeneous emulsion. Because the background pattern contributes significantly to the total, measured scattering pattern, it is not simply subtracted but accounted for in the redistribution scheme in section 5. The absolute scaling of the detector signals 1-31 according to section 3 is done for the

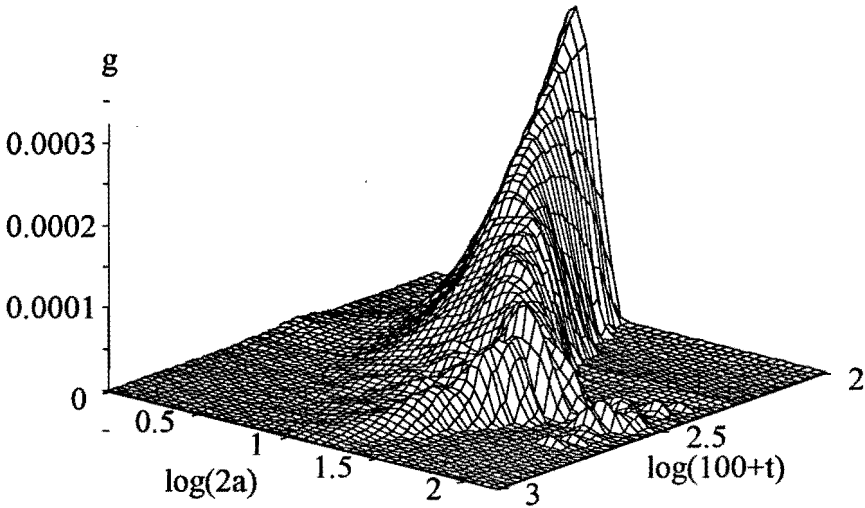


Figure 5.6. Evolution of size distribution g during electric field enhanced coalescence. The sphere radius a is given in μm and the time t in seconds. The total initial fraction of water in kerosene is $3.2 \cdot 10^{-4}$

first measurement according to Eq.5.8, while for the remaining measurements Eq.5.8 is used to correct for the laser power fluctuations.

Figure 5.6 shows the resulting evolution of the size distribution g . For the single scattering inversion (Eq.5.1) in the iterative scheme in section 5 a smoothing constant $\alpha = 0.2$ is used. The relative remaining error $|\Delta\mathbf{b}|/|\mathbf{b}_{\text{sc}}|$ increases from initially 0.003 to approximately 0.01 at the end of the measurement. Initially the maximum drop size increases until the largest drops have settled to a position beneath the laser beam due to the limited cell height, and the maximum drop size decreases again. If only the single scattering inversion is used, the initial distributions have a larger fraction of smaller drops. In Chapter 7 this evolution of the size distribution is compared with a calculated evolution.

If a similar initial size distribution is monitored without an electric field, then the size distribution remains constant, while the total fraction dispersed phase decreases slowly.

Numerical tests of the proposed multiple scattering inversion were done for cases similar to the experimental one, i.e. for the given scattering matrix, transmittances above 0.8, multiplicative noise, leading to corresponding remaining relative errors $|\Delta\mathbf{b}|/|\mathbf{b}_{\text{sc}}|$, and size distributions similar to the ones calculated from measured data. The test results were good, i.e. $|\Delta\mathbf{x}|/|\mathbf{x}| < 10^{-2}$. Other numerical tests using a relative

refractive index of $m=1.333$, similar size distributions but less multiplicative noise lead to good results for transmittances as low as 0.1.

5.7. Conclusion

It is shown that it is possible to measure drop size distributions during electric field enhanced coalescence of a w/o emulsion, using forward light scattering. The exact knowledge of the scattering behaviour of the drops allows a more accurate calculation of the size distribution than normally is the case for particle sizing using forward light scattering measurements. An iterative multiple scattering inversion scheme, using a series of thin single scattering slabs, is applied to improve the calculated size distributions for transmittances not very close to one.

Appendix

The function $G_{i,j,k}$ that relates incident, scattering and resulting axisymmetric solid angles is calculated as follows. Figure 5.7 shows two angular intervals j and k offset an angle ϑ_i , which should be depicted as ring-shaped areas on a unit sphere. The power incident at angle ϑ_i , i.e. within the solid angle i , and scattered by the slab towards solid angle j relative to the angle of incidence, is divided among several solid angles relative to the optical axis, and a fraction $G_{i,j,k}$ is scattered towards solid angle k . The condition $\vartheta_i + \theta_j < \theta_{\max}$ leads to $\sum_k G_{i,j,k} = 1$. For power not yet scattered prior to the considered slab, i.e. $i = 0$, the scattering intervals in the slab correspond exactly to the resulting angular intervals, so $G_{0,j,k} = \delta_{j,k}$, while similarly $G_{i,0,k} = \delta_{i,k}$. For

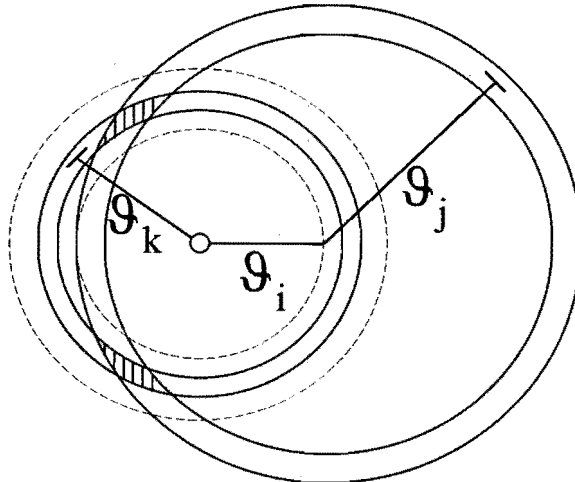


Figure 5.7. Common solid angle for solid angle k and solid angle j that is offset an angle ϑ_i relative to the laser beam direction $\vartheta = 0$, in the small angle approach.

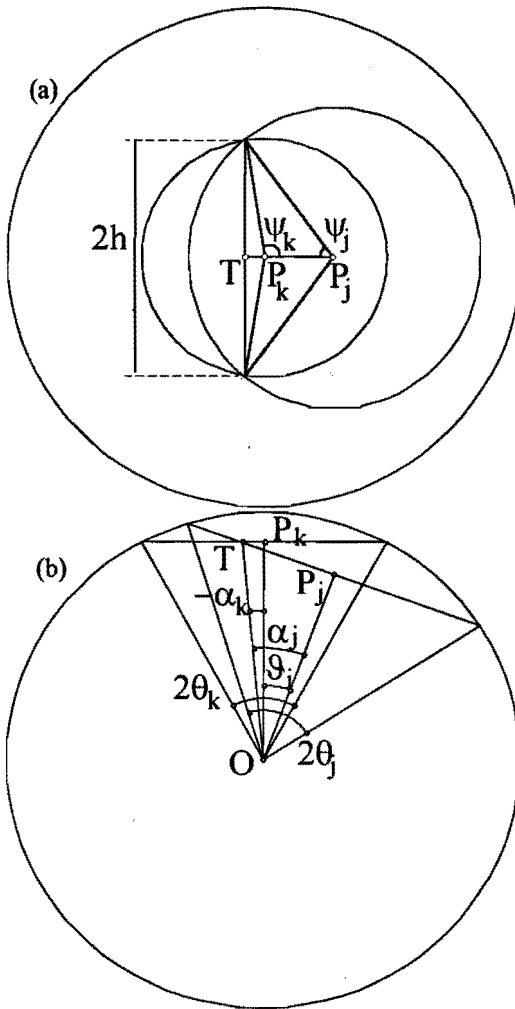


Figure 5.8. Two circles on a unit sphere with centers P_j and P_k , radii $\sin\theta_j$ and $\sin\theta_k$, (a) front view, (b) top view. The areas bounded by these circles are given by $2\pi(1-\cos\theta_j)$ and $2\pi(1-\cos\theta_k)$, while the common area also depends on the offset angle S_i .

$i > 0 \wedge j > 0$ the fraction $G_{i,j,k}$ is given by the ratio of the area shared by both rings in Fig.5.7 and the total area of the ring j :

$$G_{i,j,k} = \frac{S_{i,j,k} - S_{i,j-1,k} - S_{i,j,k-1} + S_{i,j-1,k-1}}{2\pi(\cos\theta_{j-1} - \cos\theta_j)} \quad (5.11)$$

where

$$S_{i,j,k} = 2\psi_j(1 - \cos\theta_j) - \frac{2h}{\sin\alpha_j}(1 - \cos\alpha_j) + 2\psi_k(1 - \cos\theta_k) - \frac{2h}{\sin\alpha_k}(1 - \cos\alpha_k) \quad (5.12)$$

is the common part of the two solid angles represented in Fig.5.8 as two circular areas on a unit sphere with radii $\sin\theta_j$, $\sin\theta_k$, centers P_j and P_k , areas $\pi(1-\cos\theta_j)$ and $\pi(1-\cos\theta_k)$ offset an angle ϑ_i . The angles α_j and ψ_j are given by

$$-\frac{\pi}{2} < \alpha_j = \arctan \frac{P_j T}{\cos \vartheta_j} < \frac{\pi}{2}, \quad P_j T = \frac{\cos \theta_k - \cos \theta_j \cos \vartheta_i}{\sin \vartheta_i},$$

$$0 \leq \psi_j = \arctan \frac{h}{\sin \alpha_j} < \pi, \quad h^2 = \sin^2 \theta_j - (P_j T)^2$$

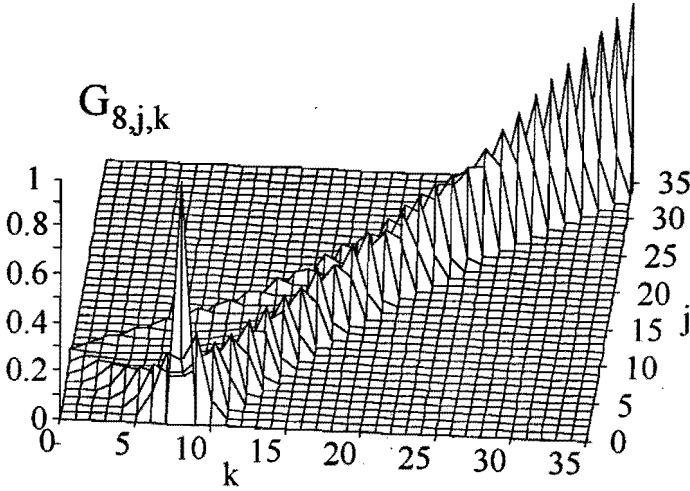


Figure 5.9. Part of the function G for incident scattering solid angle $i = 8$.

and α_k and ψ_k are found if j and k are interchanged in the four equations above. The first and third term of Eq.5.12 are positive pie-shaped fractions ψ_j/π and ψ_k/π of the circular areas (centers P_j and P_k) on the unit sphere, while the second and fourth term are corresponding triangular areas with two sides corresponding with the two straight sides of the "pies" and the curved side replaced by the vertical line with length $2h$ through point T , which due to the sign of angle α may be positive or negative. The angles must satisfy $\alpha_j + \alpha_k = \vartheta_i$ and calculation of h using index j or index k should lead to the same value. For the example in Fig.5.8 $\alpha_j > 0$ and $\alpha_k < 0$. The function $G_{i,j,k}$ as given by Eq.5.11 must be averaged over the angle of incidence, i.e. the offset angle $\theta_{i-1} < \vartheta_i < \theta_i$. The factor $\cos \vartheta_i$ in Eq.5.5 should be included in this averaging, leading to negligibly deviating values for $\overline{G_{i,j,k} / \cos \vartheta_i} \approx \overline{G_{i,j,k}} / \cos \vartheta_i$. Figure 5.9 shows $G_{8,j,k}$ for $j, k \in [0, 35]$, giving the resulting light fractions in solid angle k that were incident in solid angle 8 and scattered by the slab within a solid angle j . For small angles these relations correspond with the approximation of Hirleman⁵ and Gomi⁶.

references

- ¹T. J. Williams and A. G. Bailey, *J. Coll. Int. Sci.* **5**, 286 (1980).
- ²H. F. M. van den Bosch, Preprints AIChE First Separations Division Topical Conference, Miami Beach, p.259 (Nov. 1992).
- ³E. D. Hirleman, *Optical particle sizing/ Theory and Practice*, Eds. G. Gouesbet and G. Grehan, p.135 and 159 (Plenum Press New York 1988).
- ⁴H.C. van de Hulst, *Multiple light scattering*, (Academic press, Inc. 1980).
- ⁵E. D. Hirleman, *Appl. Opt.* **30**, 4832 (1991).
- ⁶H. Gomi, *Appl. Opt.* **25**, 3552 (1986).
- ⁷H. Schnablegger and O. Glatter, *Appl. Opt.* **34**, 4389 (1995).
- ⁸W. Hartel, *Licht* **10**, 141 (1940).
- ⁹C. L. Lawson and R. J. Hanson, *Solving Least Squares Problems*. (Prentice Hall 1974).
- ¹⁰S. J. Twomey, *J. Ass. Comput. Mach.* **10**, 97 (1963).
- ¹¹C. F. Bohren and D. R. Huffman, *Absorption and scattering of light by small particles*. (Wiley, New York 1983).
- ¹²J. R. Rogers and R. H. Davis, *J. Atmos. Sci.* **47**, 1057 (1990).

Chapter 6. Two conducting spheres in a parallel electric field

A method is presented to calculate the force exerted on a conducting sphere by another conducting sphere in a parallel electric field. The method allows any size ratio, distance, electric charge and field angle. It uses a number of electric charge images and dipole images, depending on the required accuracy and the distance between the spheres.

6.1. Introduction

Electrostatic coalescence, i.e. the merging of two small drops into a larger one due to an electric field, has been used in the petrochemical industry for more than fifty years to enhance the separation of water-in-oil emulsions. One of the requirements in modeling the behavior of this system of small spherical water drops in a non-conducting fluid is knowledge of the forces acting on two electrically conducting spheres in an electrical field.

The field outside a polarizable sphere, having any dielectric permittivity, in a uniform electric field is exactly represented by the field of a dipole image at the centre of the sphere. The value of this dipole depends on the field strength, sphere size and the relative permittivity. For two spheres it is possible to calculate the central image dipole for each sphere taking mutual induction into account, but this is not exact. This paper shows that for conducting spheres it is possible to calculate more electric images, both charges and dipoles, inside both spheres leading to a field description with any required accuracy. The force exerted by one sphere on the other is calculated by summing the forces between all electric images.

This image method is verified by calculating the electric potential at several points on the surface of one sphere due to the uniform field and all images. For a conducting sphere these potentials should be equal. The calculated forces are compared to results of other authors.

Davis¹ presented earlier a complete analytical solution using bispherical coordinates for two conducting spheres and the same general conditions, i.e any size ratio, distance (>0), electric charge and field angle. His solution contains infinite series that require significantly more programming than the image method presented here. Lebedev and Skal'skaya² used degenerate bispherical coordinates to find an analytical solution for the force between two conducting equal touching spheres.

Arp and Mason³ evaluated the infinite series by Davis to obtain simple expressions for large and small distances between two equal conducting spheres. Clercx and Bossis⁴ presented results for two equal polarizable spheres, obtained by a method using multipoles, and found a perfect match with results from Arp and Mason. They also presented results concerning two different configurations with three spheres. Their main interest, however, was in many body electrostatics.

Another equally valid image method was presented by Jones⁵. He used pairs of image charges to represent the electrostatics of two unequal conducting spheres. He did not calculate the interparticle force but the effective dipole moment and resulting torque. He also presented results concerning chains of more than two spheres⁶ and intersecting spheres⁷.

Lindell¹¹ and Sten¹² also present a method using images. Besides point images they also use line images and consider besides conducting spheres also dielectric spheres.

6.2. Dipole image

A conducting earthed sphere with radius a is placed at the origin in the electric potential of a source charge q_s at position \mathbf{r}_s . A surface charge on the sphere is induced, while the electric potential on the surface of the sphere remains zero. The electric potential caused by this surface charge may be represented by the potential of an image charge^{8,9}

$$q_i = -f \cdot q_s \quad , \quad f = \frac{a}{|\mathbf{r}_s|} \quad (6.1)$$

at position

$$\mathbf{r}_i = f^2 \cdot \mathbf{r}_s \quad (6.2)$$

For the same conducting earthed sphere placed in the electric potential of a source dipole \mathbf{p}_s at \mathbf{r}_s , the potential of the induced surface charge may also be represented by the potential of electric images inside the sphere.

The source dipole $\mathbf{p}_s = (p_{s,x}, p_{s,y}, p_{s,z})$ is placed on the x-axis at $\mathbf{r}_s = (x_s, 0, 0)$ and may be described by a charge q_s at \mathbf{r}_s and a charge $-q_s$ at $\mathbf{r}_s - \mathbf{r}_d$, where $\mathbf{p}_s = q_s \mathbf{r}_d$ in the limit $r_d \rightarrow 0$ (Fig. 6.1). The images of this dipole consist of an image charge q_i at \mathbf{r}_i (Eqs. 6.1 and 6.2) and an image charge $q_i' = -q_i(1 + x_d / x_s)$ at position $\mathbf{r}_i + f^2(x_d, -y_d, -z_d)$, leading to an image dipole

$$\mathbf{p}_i = f^3 \begin{pmatrix} p_{s,x} \\ -p_{s,y} \\ -p_{s,z} \end{pmatrix} \quad (6.3)$$

and an image charge $q_{i,p} = q_i + q_i'$

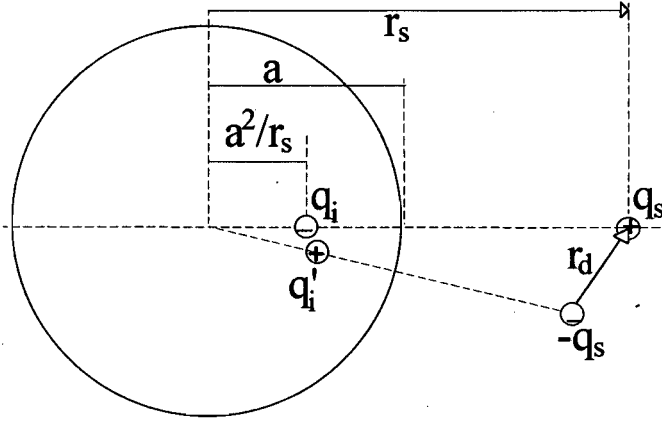


Figure 6.1. Relative positions for a pair of source charges and their induced images.

$$q_{i,p} = f^2 \frac{p_{s,x}}{a} = \frac{p_{i,x}}{f \cdot a} \quad (6.4)$$

both at position r_i . In this derivation, squares of x_d , y_d and z_d are neglected. The charge image induced by an outside dipole is positive if the source dipole and the image dipole point away from the spheres centre, otherwise the charge image is negative.

The potential due to the surface charge induced by a dipole on a earthed conducting sphere is thus exactly represented by an image dipole and an image charge. If the conducting sphere is isolated, the total charge on the sphere remains unchanged, and any induced charge is compensated by an extra opposite image charge located at the centre of the sphere.

6.3. Two spheres

Consider two spheres A and B with radii a_A and a_B placed at r_A and r_B in a parallel electric field E_0 with arbitrary orientation (Fig.6.2). The dielectric permittivities of the continuous phase and the particles are given by ϵ and ϵ_p , respectively. The field may be decomposed in a component parallel and a component perpendicular to the distance vector d ($d = r_B - r_A$) given by $E_{0\parallel} = |E_0| \cos \vartheta$ and $E_{0\perp} = |E_0| \sin \vartheta$, where ϑ is the angle between the field direction and the distance vector. Two unit vectors e_{\parallel} and e_{\perp} are defined to give $E_0 = E_{0\parallel} \cdot e_{\parallel} + E_{0\perp} \cdot e_{\perp}$. The first-order dipole images $p_{A,1}$ and $p_{B,1}$ at the centres of the spheres have components parallel and normal to the distance vector d given by^{8,9}

$$p_{A,\parallel} = 4\pi\epsilon\beta \cdot a_A^3 \cdot E_{0\parallel} \quad p_{A,\perp} = 4\pi\epsilon\beta \cdot a_A^3 \cdot E_{0\perp} \quad (6.5)$$

$$p_{B,\parallel} = 4\pi\epsilon\beta \cdot a_B^3 \cdot E_{0\parallel} \quad p_{B,\perp} = 4\pi\epsilon\beta \cdot a_B^3 \cdot E_{0\perp} \quad (6.6)$$

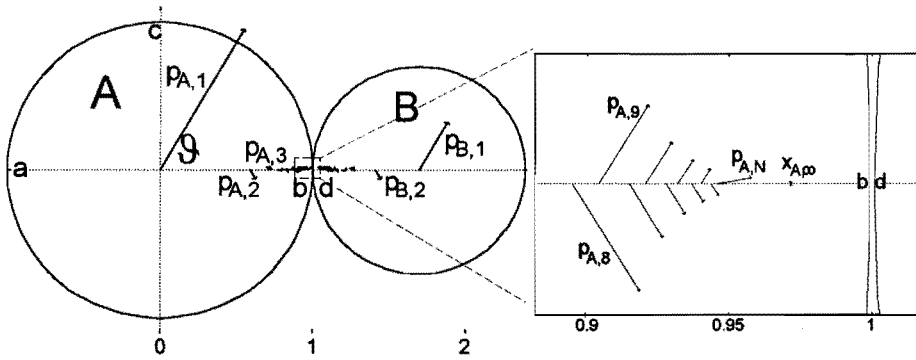


Figure 6.2. Dipole images inside two different spheres induced by an external electric field. The radii are a_A and $a_B=0.7 \cdot a_A$, the distance is $h = d - a_A - a_B = 0.001 \cdot a_A$ and the field makes an angle $\vartheta = \pi/3$ with the drawn axis. A close-up shows the deviating N^{th} dipole and the mutual inversion point $x_{A,\infty}$

where $\beta = (\epsilon_p - \epsilon) / (\epsilon_p + 2\epsilon)$. For large distances between the spheres these first order dipoles give a good approximation for the electrostatics. A better approximation, that takes mutual induction into account, is treated in the next section. The remainder of the paper describes an 'exact' method, using multiple image positions, that is valid only for conducting spheres ($\beta = 1$).

Two extra conditions must be imposed upon the system. Two possible ways for choosing these conditions are discussed in this thesis:

case 1: The potentials V_A and V_B of both spheres are separately fixed. With $V_A=V_B=0$, this case is equal to the "grounded" sphere constraint of ref.6.

case 2: For isolated spheres, the charges q_A and q_B may be separately fixed to any value. With $q_A=q_B=0$, this case is equal to the "isolated" sphere constraint of ref.6.

Another realisable set of conditions, not discussed in this paper, is a fixed total charge and a fixed potential difference. This case was treated by Jones⁵ for two conducting unequal touching spheres with $q_A+q_B=0$ and $V_A-V_B=0$. Other physically motivated sets of conditions may be envisioned.

In case 1 (imposed potentials), the first-order charge images induced by those potentials and the external applied field are given by

$$q_{A,1} = 4\pi\epsilon(V_A + \mathbf{E}_0 \cdot \mathbf{r}_A)a_A \tag{6.7}$$

$$q_{B,1} = 4\pi\epsilon(V_B + \mathbf{E}_0 \cdot \mathbf{r}_B)a_B \tag{6.8}$$

where V_A and V_B are the imposed potentials relative to the potential at $r = 0$. In case 2 (isolated spheres), the first-order charges are not defined.

6.4. One image position

The central images in both spheres may be calculated taking mutual induction into account. This gives at moderate distances a better approximation than the first order dipoles. The dipoles \mathbf{p}_A and \mathbf{p}_B are partly induced by the external field, leading to the first-order dipoles $\mathbf{p}_{A,1}$ and $\mathbf{p}_{B,1}$ (Eqs.6.5 and 6.6), and partly by the dipole image in the other sphere. The components parallel and normal to the distance vector are again considered separately. In case 1 (imposed potentials ($\beta=1$)) the dipoles are given by

$$\mathbf{p}_{A\parallel} = \mathbf{p}_{A,1\parallel} + f_A^3 \mathbf{p}_{B\parallel} \quad \mathbf{p}_{A\perp} = \mathbf{p}_{A,1\perp} - f_A^3 \mathbf{p}_{B\perp} \quad (6.9)$$

$$\mathbf{p}_{B\parallel} = \mathbf{p}_{B,1\parallel} + f_B^3 \mathbf{p}_{A\parallel} \quad \mathbf{p}_{B\perp} = \mathbf{p}_{B,1\perp} - f_B^3 \mathbf{p}_{A\perp} \quad (6.10)$$

where $f_A = a_A/d$ and $f_B = a_B/d$ with $d = |\mathbf{d}|$. As will frequently occur in the rest of this paper, the solutions of these pairs of equations are found by substitution and are not presented. Similarly, the charge images are partly induced by both imposed voltage and field, leading to the first-order charges $q_{A,1}$ and $q_{B,1}$ (Eqs.6.7 and 6.8), and partly by the charge and dipole image in the other sphere

$$q_A = q_{A,1} - f_A \cdot q_B + \frac{f_A}{d} \mathbf{p}_{B\parallel} \quad (6.11)$$

$$q_B = q_{B,1} - f_B \cdot q_A - \frac{f_B}{d} \mathbf{p}_{A\parallel} \quad (6.12)$$

A positive parallel dipole image in sphere B points away from sphere A and induces a positive charge in sphere A. A positive parallel dipole image in sphere A points towards sphere B and induces a negative charge in sphere B.

Case 2 (isolated spheres), with given charges q_A and q_B , is treated for any value of β . The parallel dipole image $\mathbf{p}_{A\parallel}$ is induced by three field contributions

$$\frac{\mathbf{p}_{A\parallel}}{4\pi\epsilon\beta \cdot a_A^3} = E_{0\parallel} + \frac{2\mathbf{p}_{B\parallel}}{4\pi\epsilon \cdot d^3} - \frac{q_B}{4\pi\epsilon \cdot d^2}$$

The corresponding relations for $\mathbf{p}_{B\parallel}$ and the normal components lead for both directions again to two equations with two unknowns. For neutral spheres these equations lead to the following dipole images

$$\mathbf{p}_{A\parallel} = \frac{1 + 2\beta \cdot f_B^3}{1 - 4\beta^2 f_A^3 f_B^3} \cdot \mathbf{p}_{A,1\parallel} \quad \mathbf{p}_{A\perp} = \frac{1 - \beta \cdot f_B^3}{1 - \beta^2 f_A^3 f_B^3} \cdot \mathbf{p}_{A,1\perp} \quad (6.13)$$

$$\mathbf{p}_{B\parallel} = \frac{1 + 2\beta \cdot f_A^3}{1 - 4\beta^2 f_A^3 f_B^3} \cdot \mathbf{p}_{B,1\parallel} \quad \mathbf{p}_{B\perp} = \frac{1 - \beta \cdot f_A^3}{1 - \beta^2 f_A^3 f_B^3} \cdot \mathbf{p}_{B,1\perp} \quad (6.14)$$

where $f_A = a_A/d$ and $f_B = a_B/d$. The parallel dipole components are enlarged by the mutual induction, while the normal components are diminished. For very large distances the

dipoles are equal to the first-order dipoles. For charged spheres, the parallel components also depend on both charges.

6.5. Multiple image positions

For conducting spheres ($\beta = 1$) more images at different positions may be used to represent the electrostatics, leading to any required accuracy. The x -axis is taken through the centres of the spheres so $r_A = 0$ and $r_B = (d, 0, 0)$ with $d > 0$. All images are located inside the two spheres on the line connecting their centres, i.e. on the x -axis (Fig.6.2). The positions of the first images are given by: $x_{A,1} = 0$ and $x_{B,1} = d$. The positions of all other images $k > 1$ are given by

$$x_{A,k} = f_{A,k} \cdot a_A \quad f_{A,k} = \frac{a_A}{x_{B,k-1}} \quad (6.15)$$

$$x_{B,k} = d - f_{B,k} \cdot a_B \quad f_{B,k} = \frac{a_B}{d - x_{A,k-1}} \quad (6.16)$$

All factors $f_{A,k}$ and $f_{B,k}$ are positive, and for equal spheres $f_{A,k} = f_{B,k}$. For large values of k the positions of the images are very close to one another. The limit for the image positions is given by the mutual image positions found by rewriting Eqs.15 and 16 as

$$x_{A,\infty} = \frac{a_A^2}{x_{B,\infty}} \quad (6.17)$$

$$x_{B,\infty} = d - \frac{a_B^2}{d - x_{A,\infty}} \quad (6.18)$$

These mutual image positions correspond to the two centres ($\mu = -\infty, +\infty$) of the bispherical coordinate system used by Davis¹.

To obtain a distance independent accuracy for all distances the value N for the last image included in the calculation is determined by its smallest value for which

$$\frac{x_{A,\infty} - x_{A,N}}{x_{B,\infty} - x_{A,\infty}} < \xi \quad (6.19)$$

where ξ may be set to any value $\xi < 1$. To obtain a distance independent accuracy for $\xi < 10^{-3}$ and $h > 10^{-6}$ the denominator in Eq.6.19 may be replaced with the smallest sphere radius a_B . Other criteria for determining N are also possible.

6.6. Image dipoles

The values of the dipole images may be calculated with recurrent relations for both cases mentioned in section 6.3. The first-order dipoles are given by Eqs.6.5 and 6.6.

Using Eqs.3, 15 and 16 the higher-order dipoles $k > 1$ are given by

$$p_{A,k\parallel} = f_{A,k}^3 p_{B,k-1\parallel} \quad p_{A,k\perp} = -f_{A,k}^3 p_{B,k-1\perp} \quad (6.20)$$

$$p_{B,k\parallel} = f_{B,k}^3 p_{A,k-1\parallel} \quad p_{B,k\perp} = -f_{B,k}^3 p_{A,k-1\perp} \quad (6.21)$$

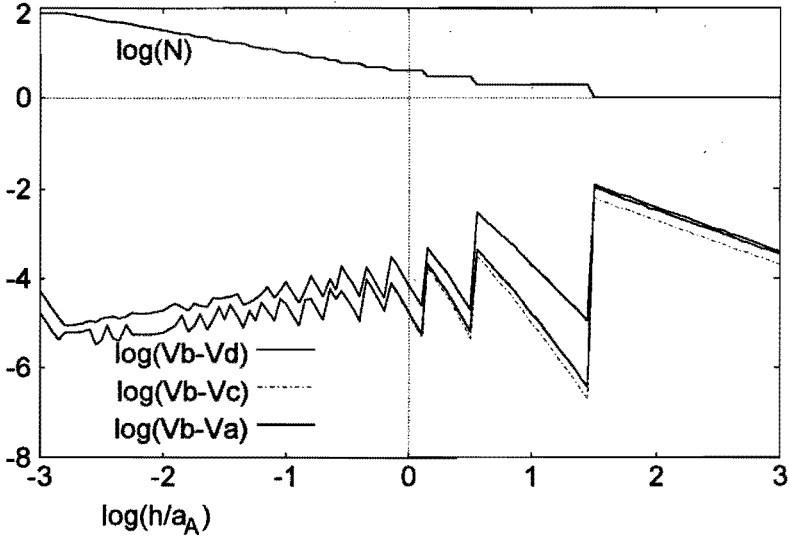


Figure 6.3. Number of images N ($\xi = 1e-3$, Eq.19) used to calculate the potentials for the situation given in Fig.6.2 with $E=1V/a_A$ and both spheres kept at potential $V=0$ as function of the distance $h=d-a_A-a_B$, and also the reached accuracy expressed in the remaining potential differences between the points b and resp. a , c and d (see Fig.2).

The last dipoles $\mathbf{p}_{A,N}$ and $\mathbf{p}_{B,N}$ may be defined to contain all dipoles for $k \geq N$. This is achieved by assuming that the last dipole in one sphere is the image of the last two dipoles in the other sphere

$$\begin{aligned} \mathbf{p}_{A,N\parallel} &= f_{A,N}^3 (\mathbf{p}_{B,N-1\parallel} + \mathbf{p}_{B,N\parallel}) & \mathbf{p}_{A,N\perp} &= -f_{A,N}^3 (\mathbf{p}_{B,N-1\perp} + \mathbf{p}_{B,N\perp}) \\ & & & (6.22) \end{aligned}$$

$$\begin{aligned} \mathbf{p}_{B,N\parallel} &= f_{B,N}^3 (\mathbf{p}_{A,N-1\parallel} + \mathbf{p}_{A,N\parallel}) & \mathbf{p}_{B,N\perp} &= -f_{B,N}^3 (\mathbf{p}_{A,N-1\perp} + \mathbf{p}_{A,N\perp}) \\ & & & (6.23) \end{aligned}$$

The induced charge images are located at the same positions as the dipole images. Their values depend on the imposed potentials or on the given total charges of the spheres. The multiple images case of imposed potentials for both spheres is treated in section 6.7, the case of given total charges is treated in section 6.8.

6.7. Imposed electric potentials

For two spheres kept at potentials V_A and V_B the image charges can be calculated with recurrent relations. The first-order charge images are given in Eqs.6.7 and 6.8. All images in one sphere are electric sources for higher-order images in the other sphere.

For an imposed potential on both spheres the charge images are given by Eqs.6.1 and 6.4, which leads to the following recurrent relations for $k > 1$

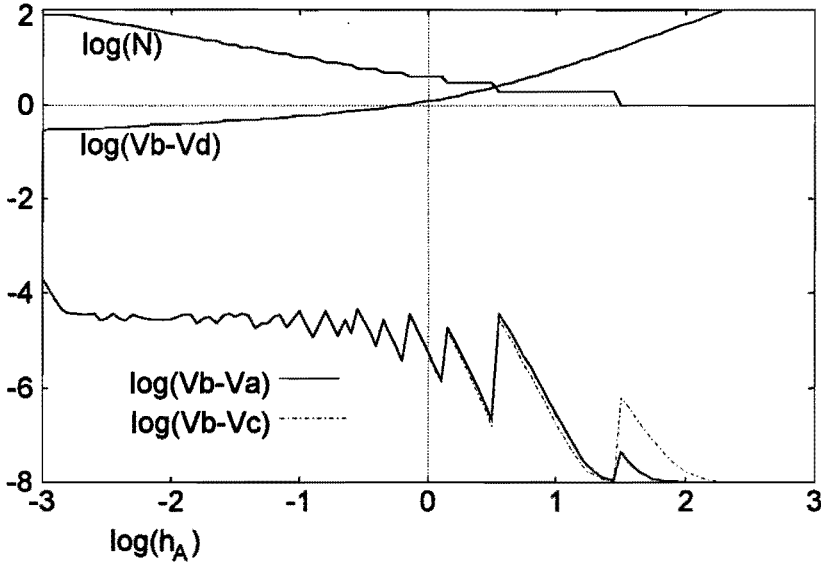


Figure 6.4. As Fig.6.3, but for two isolated neutral spheres.

$$q_{A,k} = \frac{p_{A,k} \parallel}{f_{A,k} a_A} - f_{A,k} q_{B,k-1} \quad (6.24)$$

$$q_{B,k} = -\frac{p_{B,k} \parallel}{f_{B,k} a_B} - f_{B,k} q_{A,k-1} \quad (6.25)$$

The last charge image in a sphere is again the image of the last two images in the other sphere and is found by solving the following two equations

$$q_{A,N} = \frac{p_{A,N} \parallel}{f_{A,N} a_A} - f_{A,N} (q_{B,N} + q_{B,N-1}) \quad (6.26)$$

$$q_{B,N} = -\frac{p_{B,N} \parallel}{f_{B,N} a_B} - f_{B,N} (q_{A,N} + q_{A,N-1}) \quad (6.27)$$

The accuracy of the method can be found by calculating the electric potential for different points on the surface of a sphere (see section 9, Fig.3).

6.8. Isolated spheres

For an isolated sphere, every induced charge image is compensated by an extra opposite charge image at the centre of the sphere. Every higher-order correction modifies the central charge images and by that also all lower-order charge images are modified. It is possible to modify all charge images using recurrent relations. A more direct approach, leading to a faster algorithm, is described in this section.

Considering only the charges induced by the image dipoles (Eq.6.4) leads for $k \geq 2$ to

$$q'_{A,k} = \frac{P_{A,k}}{f_{A,k} \cdot a_A} \quad q'_{B,k} = \frac{-P_{B,k}}{f_{B,k} \cdot a_B} \quad (6.28)$$

The central image charges are then given by

$$q'_{A,1} = q_A - \sum_{k=2}^N q'_{A,k} \quad q'_{B,1} = q_B - \sum_{k=2}^N q'_{B,k} \quad (6.29)$$

The different sets of the aligned components of the image dipoles and image charges located at the positions given in section 6.5 are represented as vectors $\mathbf{P}_A = [P_{A,1}, \dots, P_{A,N}]$, \mathbf{P}_B , $\mathbf{Q}'_A = [q'_{A,1}, \dots, q'_{A,N}]$, \mathbf{Q}'_B , $\mathbf{Q}_A = [q_{A,1}, \dots, q_{A,N}]$ and \mathbf{Q}_B . The normal components of the image dipoles have no effect on the image charges.

The contributions to the image charges inside one sphere induced by image charges in the other sphere are simply added as follows

$$\mathbf{Q}_A = \mathbf{Q}'_A + \mathbf{F}_A \mathbf{Q}_B \quad (6.30)$$

$$\mathbf{Q}_B = \mathbf{Q}'_B + \mathbf{F}_B \mathbf{Q}_A \quad (6.31)$$

where \mathbf{Q}_A and \mathbf{Q}_B are unknown. An image charge $q_{B,k}$ at $x_{B,k}$ in sphere B induces an image charge $-f_{A,k+1}q_{B,k}$ at $x_{A,k+1}$ and an opposite image charge at the centre $x_{A,1}$ of sphere A. Matrix \mathbf{F}_A is thus given by

$$\mathbf{F}_A = \begin{bmatrix} f_{A,2} & f_{A,3} & & f_{A,N-1} & f_{A,N} & f_{A,N} \\ -f_{A,2} & & & & & \\ & -f_{A,3} & & & & \\ & & & & 0 & \\ & & & & & \\ & 0 & & -f_{A,N-1} & & \\ & & & & -f_{A,N} & -f_{A,N} \end{bmatrix} \quad (6.32)$$

where the last two image charges in sphere B contribute in the same way to the last image charge in sphere A. Matrix \mathbf{F}_B is similar to \mathbf{F}_A with $f_{B,k}$ instead of $f_{A,k}$. Substituting Eq.31 in Eq.30 gives

$$(\mathbf{I} - \mathbf{F}_A \mathbf{F}_B) \mathbf{Q}_A = \mathbf{Q}'_A + \mathbf{F}_A \mathbf{Q}'_B \quad (33)$$

with \mathbf{I} the identity matrix: $I_{ij} = \delta_{ij}$. The matrix $\mathbf{I} - \mathbf{F}_A \mathbf{F}_B$ and the right-hand side of this equation are known. The charge vector \mathbf{Q}_A is solved by Crout's algorithm (LU-decomposition) for general matrix inversion.

For the symmetric case, i.e. $a_B = a_A$, $q_B = -q_A$, $\mathbf{P}_B = \mathbf{P}_A$, $\mathbf{Q}'_B = -\mathbf{Q}'_A$, $\mathbf{Q}_B = -\mathbf{Q}_A$ and $\mathbf{F}_B = \mathbf{F}_A$, only one matrix equation is left, leading to

$$(\mathbf{I} + \mathbf{F}_A) \mathbf{Q}_A = \mathbf{Q}'_A \quad (6.34)$$

For the inversion of the matrix equation (6.34) a much faster algorithm, allowing much more images, is made to find Q_A . For an equal number of images the result is not as accurate as Crout's algorithm because no pivoting is used.

The accuracy can again be found by calculating the electric potential for different points on the surface of a sphere (see section 6.9 and Fig.6.4).

6.9. Potentials

The method presented in this paper is verified by calculating the potentials on several points on the surface of the spheres. All points on a conducting sphere should have the same potential. The sum of the potentials by the applied field and all calculated images for both spheres is given by

$$V(\mathbf{r}) = -\mathbf{E} \cdot \mathbf{r} + \frac{1}{4\pi\epsilon} \sum_{A \in (A,B)} \sum_{i=1}^N \left(\frac{q_{A,i}}{|\mathbf{r} - \mathbf{r}_{A,i}|} + \frac{\mathbf{p}_{A,i} \cdot (\mathbf{r} - \mathbf{r}_{A,i})}{|\mathbf{r} - \mathbf{r}_{A,i}|^3} \right) \quad (6.35)$$

For the case of two equal earthed spheres ($V_A = V_B = 0$) and two isolated neutral spheres, respectively, Figs.6.3 and 6.4 show the potential differences between point b and the points a, c and d (Fig.6.2) according to Eq.6.35. The number of images N is determined by Eq.6.19 for $\xi = 1e-3$. Both Figs.6.3 and 6.4 show that for a stepwise increase of N the remaining potential differences decrease stepwise, i.e. including an extra image makes the calculation more accurate. The accuracy is limited by the maximum number of images and the precision of the variable types used. For the results shown the maximum value for N was set at 80, causing an increase of the remaining potential differences at the smallest distance.

For two isolated spheres it follows from Fig.6.4 that the potential difference between both spheres ($V_b - V_d$) hardly changes for small values of h . For decreasing distance h the electric field between two isolated spheres, given by $(V_b - V_d)/h$, may reach any value³. Since any isolating material will only allow a certain field, electric breakdown will decrease the field between the spheres. The electric forces in the high field area may also cause mechanical deformations, i.e. the spherical shape that is required for this calculation method is then distorted.

6.10. Sphere - sphere force

The total force exerted on sphere B consists of a force due to the external field and a force due to the surface charge on sphere A, i.e. the mutual force. Using known force relations^{8,9} between charges and dipoles, this mutual force is found by a double summation. The motivation for the three separate rows is given below.

$$\mathbf{F}_{B,mut} = \frac{1}{4\pi\epsilon} \sum_{i=1}^N \sum_{j=1}^N \left(\begin{array}{l} \left(\frac{q_{A,i} \cdot q_{B,j}}{d_{ij}^2} + 2 \frac{p_{A,i||} q_{B,j} - q_{A,i} p_{B,j||}}{d_{ij}^3} - 6 \frac{p_{A,i||} p_{B,j||}}{d_{ij}^4} \right) \cdot \mathbf{e}_{||} \\ + 3 \frac{p_{A,i\perp} p_{B,j\perp}}{d_{ij}^4} \\ + \left(\frac{q_{A,i} p_{B,j\perp} - p_{A,i\perp} q_{B,j}}{d_{ij}^3} + 3 \frac{p_{A,i||} p_{B,j\perp} + p_{A,i\perp} p_{B,j||}}{d_{ij}^4} \right) \cdot \mathbf{e}_{\perp} \end{array} \right) \quad (6.36)$$

where $d_{ij} = x_{B,j} - x_{A,i}$. The force $\mathbf{F}_{B,mut}$ is opposite to the force exerted on sphere A by sphere B, i.e. $\mathbf{F}_{A,mut} = -\mathbf{F}_{B,mut}$, so the total force exerted on each sphere is given by

$$\mathbf{F}_A = q_A \mathbf{E}_0 - \mathbf{F}_{B,mut} \quad (6.37)$$

$$\mathbf{F}_B = q_B \mathbf{E}_0 + \mathbf{F}_{B,mut} \quad (6.38)$$

For two isolated neutral spheres ($q_A = q_B = 0$) both the parallel image dipoles and image charges are proportional to $E_{0||}$, while the normal image dipoles are proportional to $E_{0\perp}$. The total field consists thus of a contribution due to $E_{0||}$ and a contribution due to $E_{0\perp}$. The total force, that is equal to the mutual force, consists correspondingly of three contributions. The first row of Eq.6.36 is proportional to $E_{0||}^2$, the second row to $E_{0\perp}^2$, and the third row to $2E_{0||}E_{0\perp}$. Divided by these field products and by $4\pi\epsilon a_A^2$, the three rows of Eq.6.36 correspond to the force functions F_1 , F_2 and F_8 , respectively, as defined by Davis¹. These functions only depend on the relative geometry of the problem, i.e. a_B/a_A and h/a_A . Dividing the three rows of Eq.6.36 by the corresponding expressions for the first-order dipoles only, i.e. $-6p_{A,i||}p_{B,i||}d^{-4}$, $3p_{A,i\perp}p_{B,i\perp}d^{-4}$ and $3(p_{A,i||}p_{B,i\perp} + p_{A,i\perp}p_{B,i||})d^{-4}$ leads to three positive dimensionless forces $f_{||}$, f_{\perp} and f_r , respectively, all approaching one for large distances, as used by Klingenberg¹⁰ and Clercx and Bossis⁴. Once these three dimensionless forces are known, as function of size ratio and distance, the total force acting on sphere B is directly given by

$$\mathbf{F}_B = -24\pi\epsilon E_0^2 a_A^3 a_B^3 d^{-4} \left[\left(f_{||} \cos^2 \vartheta - \frac{f_{\perp}}{2} \sin^2 \vartheta \right) \cdot \mathbf{e}_{||} - \frac{f_r}{2} \sin 2\vartheta \cdot \mathbf{e}_{\perp} \right] \quad (6.39)$$

Our results for these dimensionless forces for two equal conducting spheres ($a_A = a_B = a$) correspond exactly to the values tabulated for $h/a \geq 2 \cdot 10^{-4}$ by Clercx and Bossis⁴ and by Arp and Mason³ (expressed as F_1, F_2 and F_8). For smaller values of h/a our results approach the analytical expressions valid for $h/a \ll 1$, derived by Arp and Mason³ from the infinite series by Davis¹. This was verified for $h/a \geq 3 \cdot 10^{-7}$ using the faster inversion algorithm for Eq.34 and 8000 image positions.

Figures 6.5, 6.6 and 6.7 show the dimensionless forces $f_{||}$, f_{\perp} and f_r as function of size ratio $a_A/a_B > 1$ and relative distance h/a_B . At the elevated flat region of the surface plot for $f_{||}$ at larger size ratios, only the polarization of the small sphere is affected by

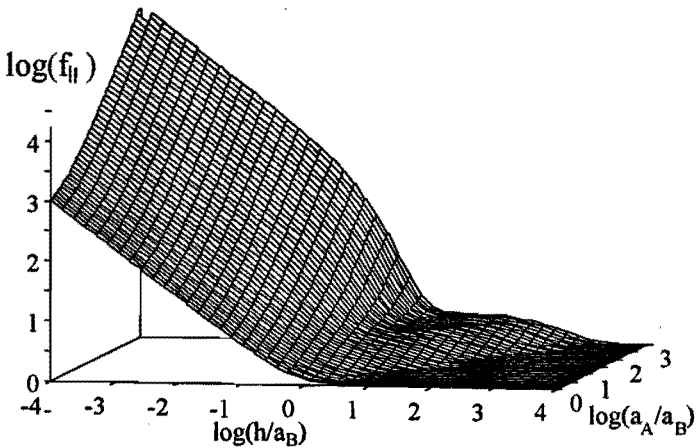


Figure 6.5. The dimensionless force $f_{||}$ as function of size ratio

$$1 \leq a_A / a_B \leq 10^3 \text{ and relative distance } 10^{-4} \leq h / a_B \leq 10^4.$$

mutual induction leading to $f_{||} \approx 3$ ($\log(f_{||}) \approx 1/2$). The relatively steep region at a slightly smaller distance corresponds with the strong distance dependence of the central image charge in the large sphere at that distance.

For two charged isolated spheres, the total field is a superposition of four independent contributions due to $E_{0||}$, $E_{0\perp}$, q_A and q_B , leading to ten different field products contributing to the force F_B . Davis¹ defined ten corresponding force functions depending only on sphere ratio and distance to give the total force. To determine these ten force functions with the method presented here requires calculation of three pairs of charge vectors Q_A and Q_B induced separately by $E_{0||}$, q_A and q_B , respectively. The normal field component $E_{0\perp}$ does not induce any charges.

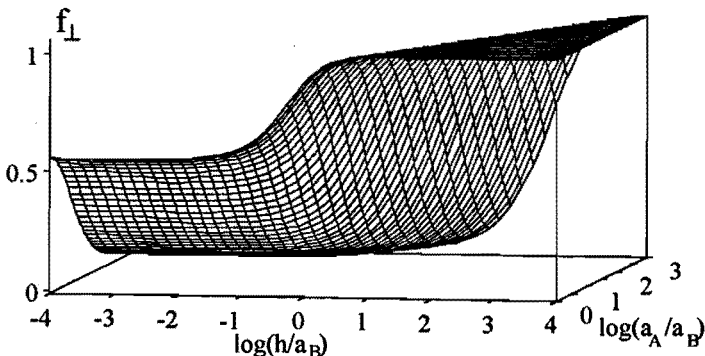


Figure 6.6. Dimensionless force $f_{\perp}(a_A/a_B, h/a_B)$ (see Fig. 6.5).

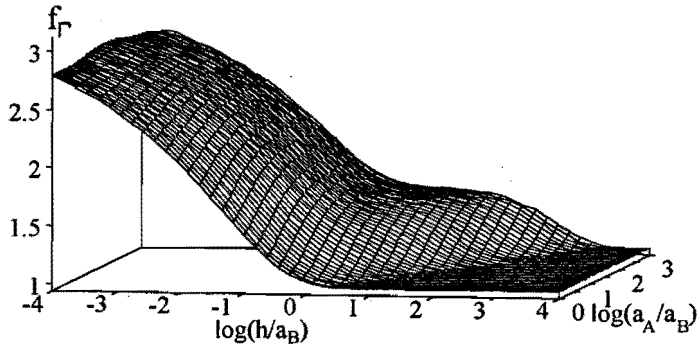


Figure 6.7. Dimensionless force $f_r(a_A/a_B, h/a_B)$ (see Fig. 6.5).

For two earthed spheres with $\mathbf{r}_A \parallel \mathbf{r}_B$, the induced charges are proportional to the parallel field component, and a similar approach as for isolated neutral spheres is possible, i.e. there are only two independent field contributions proportional to $E_{0\parallel}$ and $E_{0\perp}$.

6.11. Equal earthed contacting spheres

Two equal earthed contacting spheres ($a_A = a_B = a$, $h = 0$, $V_A = V_B = 0$) lead to the following simple set of images for sphere B

$$x_k = \frac{a}{k} \quad q_k = \frac{p_{\parallel}}{ak^2} \quad p_{k\parallel} = \frac{p_{\parallel}}{k^3} \quad p_{k\perp} = \frac{p_{\perp}}{k^3} (-1)^{k-1} \quad (6.40)$$

where $p_{\parallel} = 4\pi\epsilon E_{0\parallel} a^3$. The positions are now given relative to the contact point. For sphere A the positions and charges have opposite signs while the dipoles are the same. This leads to the same equations for the net charge $q = 4\pi\epsilon E_{0\parallel} a^2 \zeta(2)$ on sphere B and the effective dipole moments $p_{\parallel} = 16\pi\epsilon E_{0\parallel} a^3 \zeta(3)$ and $p_{\perp} = 6\pi\epsilon E_{0\perp} a^3 \zeta(3)$ of both spheres, as presented earlier by Jones⁵, where the following relations for Riemann's zeta function $\zeta(s)$ are used

$$\zeta(s) = \sum_{k=1}^{\infty} \frac{1}{k^s} \quad \sum_{k=1}^{\infty} \frac{(-1)^{k-1}}{k^s} = (1 - 2^{1-s}) \zeta(s)$$

The images also give the correct potential at the contact point $V=0$. The field near the contact point of the two earthed spheres may be expected to be very low. In a small area proportional to N^{-2} around the contact point, however, the images lead to a parallel field up to $E_{\parallel} = E_{0\parallel} - 2N \cdot E_{0\parallel}$, where N is the number of included images. This error may be corrected as follows.

For two touching spheres Eq. 6.19 cannot be satisfied. Instead of last images defined according to section 6.6, the images $k > N$ positioned from $x = -a/(N+1)$ to $x = a/(N+1)$ are replaced with a continuous line charge $q' = p_{\parallel}/a^2$, a continuous line

dipole $p' = p_{\parallel} \cdot x / a^2$ from $x=0$ to $x_m = a / (N + 1/2)$, and opposite line images from $x = -x_m$ to $x=0$. These line images lead to the following contribution to the parallel field between the spheres at a distance δ from the axis

$$E_{\text{line}\parallel}(N, \delta) = \frac{2p_{\parallel}}{4\pi\epsilon a^2} \int_0^{x_m} \frac{x(x^2 - 2\delta^2)}{(x^2 + \delta^2)^{5/2}} dx = \frac{2E_{0\parallel} \cdot a \cdot x_m^2}{(x_m^2 + \delta^2)^{3/2}} \quad (6.41)$$

Near the contact point the sum of the inducing field $E_{0\parallel}$ and the field of both the point and line images leads correctly to $E_{\parallel} = 0$.

The series for the alternating normal dipoles leads in a small area proportional to N^{-2} around the contact point to a normal field between the spheres given by $E_{\perp} = \pm E_{0\perp}$. This is of no importance for N large enough.

The images of Eq.6.40 that are proportional to the parallel field, i.e. charges and parallel dipoles, lead to the following contribution to the mutual force (first row in Eq.6.36)

$$F_{\text{mut}\parallel} = 4\pi\epsilon E^2 a^2 \sum_{i=1}^N \sum_{j=1}^N \frac{(i+j)^2 - 6 \cdot i \cdot j}{(i+j)^4} \quad (6.42)$$

as was also presented earlier by Jones⁷. Performing the summation in two triangular regions in the i, j plane separated by the diagonal $i+j=N$ leads for N large enough (see Appendix) to

$$F_{\text{mut}\parallel} = 4\pi\epsilon E^2 a^2 \left(\zeta(3) - \zeta(2) - \frac{1}{12} \right) \quad (6.43)$$

In this force the line images q' and p' are not included. Neglecting these line images leads to a non-zero field $-E_{\text{line}\parallel}$ near the contact point, and thus introduces a force error given by

$$F_{\text{err}\parallel} = \int_0^{\infty} \frac{\epsilon}{2} \left(E_{\text{line}\parallel}(\delta) \right)^2 2\pi\delta d\delta = \pi\epsilon E_{0\parallel}^2 a^2 \quad (6.44)$$

independent of N . The total parallel dimensionless force is thus given by

$$F_{\parallel} = qE_{0\parallel} + F_{\text{mut}\parallel} + F_{\text{err}\parallel} = 4\pi\epsilon E_{0\parallel}^2 a^2 \left(\zeta(3) + \frac{1}{6} \right) \quad (6.45)$$

which is equal to the result of Lebedev and Skal'skaya⁵, and Arp and Mason³ (F^0_1).

The double summation of Eq.42 is not absolutely convergent and the result depends on the way the sum is taken. In the Appendix already two possible ways are shown. Whether the second triangular region ($i \leq N, j \leq N, i+j > N$) is included or not, both cases lead to a finite result for $N \rightarrow \infty$. During computations a curious summation result was found. Including only terms with $i \cdot j \leq k^2$ in the summation of Eq.6.42 leads

numerically (for $k > 10^3$ with 6 significant figures) to the correct mutual force, i.e. $F_{\text{mut}} + F_{\text{err}}$ as given in Eqs. 6.43 and 6.44. An explanation for this result is not found.

The dimensionless force of Eq. 6.45 is given by $f_{\parallel} = -(8/3)(\zeta(3) + 1/6)$. Contrary to the first-order dipoles, the spheres repel one another. The second and third row of Eq. 6.36 lead with the images of Eq. 6.40 and the net charge to the dimensionless forces

$$f_{\perp} = 16 \sum_{i=1}^{\infty} \sum_{j=1}^{\infty} \frac{(-1)^{i+j} \cdot i \cdot j}{(i+j)^4} = 2\zeta(3) - \frac{8}{3} \ln 2 \quad (6.46)$$

$$f_{\Gamma} = \frac{8}{3} \left[\zeta(2) + \sum_{i=1}^{\infty} \sum_{j=1}^{\infty} \left(\frac{i \cdot (-1)^j + j(-1)^i}{(i+j)^3} - 3 \frac{i \cdot j \cdot ((-1)^j + (-1)^i)}{(i+j)^4} \right) \right] = \frac{10}{3} \zeta(3) \quad (6.47)$$

where only the first part ($i+j \leq N$) of the summation method in the Appendix contributes. The force function f_{Γ} only contains the first power of the parallel field error near the contact point, resulting in a force error equal to zero for N large enough. The values match the corresponding results of Arp and Mason³ (F°_2 and F°_8).

6.12. Conclusion

It is shown that the potential due to a surface charge, induced by an external dipole source on a conducting sphere, is equal to the potential of an image dipole and an image charge at the usual image location. For two conducting spheres in a uniform electrical field, a large number of mutually induced charge and dipole images may be calculated, leading to an accurate potential description. The resulting force acting on both spheres may also be calculated with any required accuracy.

A fit for the dimensionless forces, or related expressions, as function of size ratio and distance, not presented here, will allow fast retrieval of the results, useful for simulating the behavior of two conducting spheres in a parallel electric field.

For simulations concerning more than two conducting particles, the dipole image method leads to a more extended image distribution, but may lead to relatively fast force calculations with a simply adjustable accuracy.

It should be noted that the dipole image method using multiple image positions is restricted to conducting spheres. Accurate calculations for polarizable spheres, having any permittivity ϵ_p , are possible with the multipole method, as used by Clercx and Bossis⁴ or possibly by a method using also line charges presented by Lindell¹¹ and Sten¹².

Appendix

The double summation of Eq.6.42 is solved analytically by dividing the square region $(i,j)=(1..N,1..N)$ into two triangular regions separated by the diagonal $i+j=N$. With $k=i+j$ the summation of the terms $i + j \leq N$ is written as

$$\sum_{k=2}^N \left(\frac{1}{k^4} \sum_{i=1}^{k-1} (k^2 - 6ki + 6i^2) \right)$$

Summation of the different powers of i leads to

$$\sum_{k=2}^N \left(\frac{k^2(k-1) - 6k \frac{1}{2} k(k-1) + k(k-1)(2k-1)}{k^4} \right) = \sum_{k=1}^N k^{-3} - \sum_{k=1}^N k^{-2}$$

With $k=i+j$ the summation of the terms $i + j > N$, $i \leq N$ and $j \leq N$ is written as

$$\sum_{k=N+1}^{2N} \left(\frac{1}{k^4} \sum_{i=k-N}^N (k^2 - 6ki + 6i^2) \right)$$

Reversing the summation order of the summation over i leads with $m=N-i$ to

$$= \sum_{k=N+1}^{2N} \left(\frac{1}{k^4} \sum_{m=i}^{2N-k} \left((k^2 - 6kN + 6N^2) + 6(k-2N)m + 6m^2 \right) \right)$$

The summation over the different powers of m leads to

$$= \sum_{k=N+1}^{2N} \left(\frac{2N}{k^2} + \frac{1-6N^2}{k^3} + \frac{4N^3+2N}{k^4} \right)$$

For N large enough the summation may be replaced with an integration with respect to k leading to

$$= \left. \frac{2N}{k} - \frac{1-6N^2}{2k^2} - \frac{4N^3+2N}{3k^3} \right|_{k=N}^{2N} \xrightarrow{N \rightarrow \infty} -\frac{1}{12}$$

References

- ¹M.H. Davis, *Quart.J.Mech.Appl.Math.* **17**, 499 (1964).
- ²N.N. Lebedev and I.P. Skal'skaya, *Sov. Phys. -Techn. Phys.* **7**, 268 (1962).
[translated from *Zh. Tek. Fiz.* **32**, 375 (1961)].
- ³P.A. Arp and S.G. Mason, *Colloid Polym.Sci.* **255**, 566 (1977).
- ⁴H.J.H. Clercx and G. Bossis, *Phys.Rev. E* **48**, 2721 (1993).
- ⁵T.B. Jones, *J.of Electrostatics* **21**, 121 (1988).
- ⁶T.B. Jones, *J.Appl.Phys.* **60**, 2226 (1986).
- ⁷T.B. Jones, *J.Appl.Phys.* **62**, 362 (1987).
- ⁸J.A. Stratton, *Electromagnetic Theory*, (McGraw-Hill, New York, 1941).
- ⁹W.R. Smythe, *Static and Dynamic Electricity*, (McGraw-Hill, New York, 1968).
- ¹⁰D.J. Klingenberg and J.F. Brady, *J.Chem.Phys.* **96**, 2183 (1992).
- ¹¹I.V. Lindell and J.C-E. Sten, *Radio Science* **28**, 319 (1993)
- ¹²J.C-E. Sten and K.I. Nikoskinen, *J. of Electrostatics* **35**, 267 (1995).

Chapter 7. Electrostatic coalescence

1. Introduction.

Relative trajectories are calculated for two spherical electrically conducting neutral drops due to gravity, an applied electric field, the van der Waals interaction, and hydrodynamic interaction in an electrically insulating continuous phase. The relative trajectories lead to collision efficiencies and collision rates. A model is presented to predict the change of a given size distribution, based on gravity induced settling of the drops, and electric field dependent collision cross sections for all pairs of drops. The resulting height-dependent evolution of an initially homogeneous size distribution is compared to an experimentally determined evolution, as presented in Chapter 5.

To describe the hydrodynamic interaction between two fluid spheres, an exact solution for motion along the line of centers and an asymptotic solution for motion normal to the line of centers, both by Haber and Hetsroni^{1,2}, are used. Zhang and Davis³ presented a thorough comparison of these and other exact and asymptotic solutions for the hydrodynamic interaction between two fluid spheres, expressed as relative mobility functions according to Batchelor⁴. The electrostatic interaction is calculated according to the image method presented in Chapter 6.

Zhang⁵ presented calculations using the exact hydrodynamic interaction, while he used for the electrostatic interaction a method by Davis⁶. Zhang did not consider the asymmetry in the horizontal field case, i.e. if the electric field is perpendicular to gravity. He found much higher collision efficiencies for the horizontal field case than for the vertical field case, while in this work both cases lead to similar efficiencies.

Sadek and Hendricks presented measurements⁷ and a model⁸ for electric field enhanced coalescence in a d.c. field, where oppositely charged drops are assumed to travel in opposite directions from one electrode to the other.

7.2. Relative velocities

Interactions between drops in the considered dilute dispersions is restricted to binary interaction, i.e. the movement of two interacting drops will rarely be influenced by a third drop. For the considered system Stokesian hydrodynamics are assumed and deviations from the spherical shape (see section 7.6), surface tension gradients, and Brownian motion are neglected.

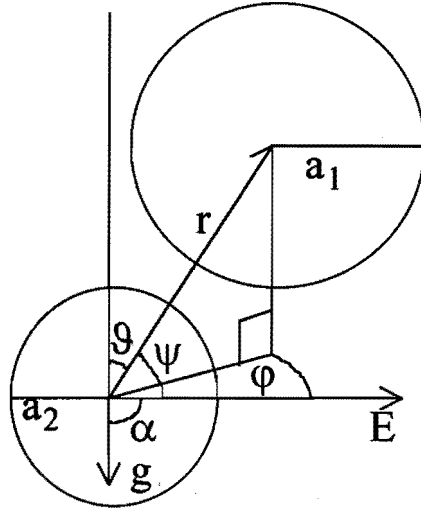


Fig.7.1. Drop radii, angles and fields for the case $\alpha = \pi/2$. The azimuth angle ϕ is the angle between $\mathbf{r} \times \mathbf{g}$ and $\mathbf{E} \times \mathbf{g}$, i.e. between the planes built by these vectors.

Consider two spherical, electrically conducting neutral drops with radii a_1 and a_2 at a relative position $\mathbf{r} = |\mathbf{r}_1 - \mathbf{r}_2| = (r, \vartheta, \phi)$ in spherical coordinates (fig.7.1). Gravity \mathbf{g} is directed along the $\vartheta = \pi$ axis and an electric field \mathbf{E} is directed along $\vartheta = \pi - \alpha$, $\phi = 0$. If hydrodynamic and electric interaction between the spheres is neglected and the sphere velocities \mathbf{v}_1 and \mathbf{v}_2 are deduced using the Hadamard-Rybczynski relation $\mathbf{F} = 6\pi\mu_c\chi a v$, where $\chi = (\mu^* + 2/3)/(\mu^* + 1)$ and $\mu^* = \mu_d/\mu_c$ is the ratio of the viscosities of the dispersed and continuous phase, the resulting relative velocities $|\mathbf{v}_1 - \mathbf{v}_2|$ due to gravity ($\mathbf{F}_g = \rho\mathbf{g} \cdot 4\pi a^3/3$), an aligned electric field (Eq.6.39 $\mathbf{F}_E = 24\pi\epsilon_c E^2 a_1^3 a_2^3 r^{-4}$) and van der Waals interaction (see Appendix) are given by

$$v_g = \frac{2\rho g}{9\mu_c\chi} a_1^2 (1 - \lambda^2), \quad (7.1)$$

$$v_E = \frac{4\epsilon_c E^2}{\mu_c\chi} a_1 \frac{\lambda^2}{(1+\lambda)^3} \frac{2^4}{s^4}, \quad (7.2)$$

$$v_A = \frac{8A}{9\pi\mu_c\chi} \frac{1}{a_1^2} \frac{\lambda^2}{(1+\lambda)^2} \left(\frac{4}{s^2 - 4} - \frac{4}{s^2(1+\lambda)^2 - 4(1-\lambda)^2} \right)^2 s, \quad (7.3)$$

respectively. The size ratio is given by $\lambda = a_2/a_1$, $\rho = \rho_d - \rho_c$ is the density difference, ϵ_c is the dielectric permittivity of the continuous phase, $s = 2r/(a_1 + a_2)$ is the dimensionless distance and A is the Hamaker constant. Electromagnetic retardation is neglected in this work. Because the Navier-Stokes equation without inertial term gives a linear relation between velocities and forces the total position-dependent

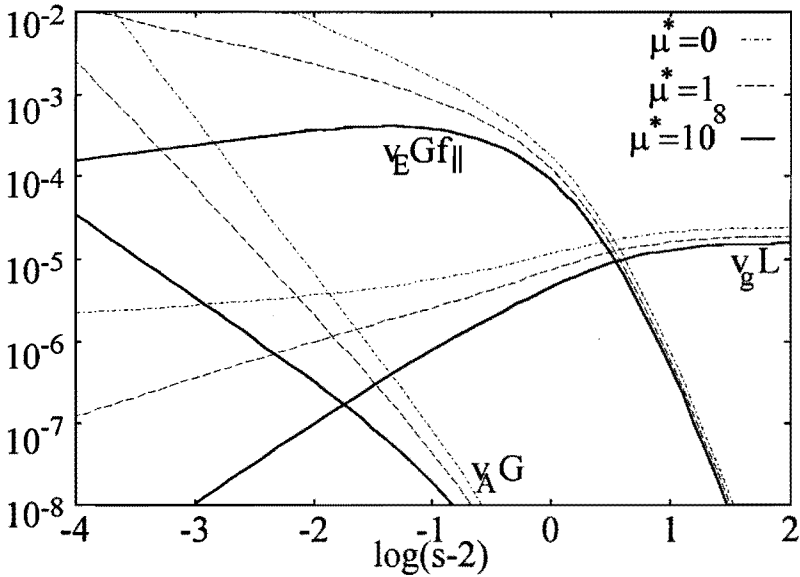


Fig.7.2. Relative velocities (m/s) due to gravity $\rho g = 980 \text{ Nm}^{-3}$, electric field $E = 10^5 \text{ V/m}$ ($\epsilon E^2 = 0.23 \text{ Nm}^{-2}$), van der Waals interaction ($A = 10^{-20} \text{ Nm}$) and continuous phase viscosity $\mu_c = 10^{-3} \text{ Nm}^{-2} \text{ s}$ as functions of the dimensionless distance s for drop radius $a_1 = 10 \mu\text{m}$, size ratio $\lambda = 0.5$ and three values of the relative viscosity $\mu^* = \mu_d / \mu_c$.

relative velocity $\mathbf{v}(s, \vartheta, \varphi) = \mathbf{v}_1 - \mathbf{v}_2$ may be written as the sum of all induced relative velocities^{3,4,5}, (Eq.6.39)

$$\mathbf{v} = v_g (-L \cos \vartheta \cdot \mathbf{e}_r + M \sin \vartheta \cdot \mathbf{e}_\vartheta) + v_E \left(-G(f_{\parallel} \cos^2 \psi - \frac{f_{\perp}}{2} \sin^2 \psi) \cdot \mathbf{e}_r + H \frac{f_{\Gamma}}{2} \sin 2\psi \cdot \mathbf{e}_\psi \right) - v_A G \cdot \mathbf{e}_r \quad (7.4)$$

where

$$\mathbf{e}_\psi = \frac{\partial \psi}{\partial \vartheta} \mathbf{e}_\vartheta + \frac{1}{\sin \vartheta} \frac{\partial \psi}{\partial \varphi} \mathbf{e}_\varphi,$$

$$\cos \psi = \sin \vartheta \cos \varphi \sin \alpha - \cos \vartheta \cos \alpha$$

and ψ gives the angle between the distance vector $\mathbf{r} = (r, \vartheta, \varphi)$ and the electric field $\mathbf{E} = (E, \alpha, 0)$. Hydrodynamic interaction is accounted for by four relative mobility functions L, M, G and H , which only depend on s , λ and μ^* , while electrostatic interaction, i.e. mutual electrical induction, is accounted for by three electric force functions f_{\parallel} , f_{\perp} and f_{Γ} which only depend on s and λ . All seven functions only depend on the relative geometry and not on the absolute size a_1 . They all approach 1 for large distances, the mobility functions and f_{\perp} are less than 1, f_{\parallel} and f_{Γ} are larger than 1. Figure 7.2 shows the resulting velocities $v_g L$, $v_E G f_{\parallel}$ and $v_A G$ for specified conditions. Their dependence on the absolute size a_1 is given by Eqs.7.1,7.2 and 7.3. The mobility

functions L and G for relative motion along the line of centers, defined by Batchelor⁴, are calculated according to the exact solution for the resistance functions by Haber and Hetsroni¹ using bispherical coordinates. (Instead of using the final results presented as coefficients δ_i , the 8 equations of their appendix B are reduced to 4 equations, and solved numerically. The last term of Equation B-8 and the exponent in this term have the wrong sign¹.) This exact solution accounts for the internal flow in the drops, but neglects surface tension gradients and deviations from the spherical shape. For our purposes the mobility functions M and H for relative motion normal to the line of centers are sufficiently accurately given by the far-field asymptotic expressions presented by Zhang and Davis³. These expressions were derived from the reflections-solution by Hetsroni and Haber², and were found to deviate less than 1% from the exact solution by Zinchenko¹⁰ for $\mu^* < 1$. For our experimental case $\mu^* = 0.63$ the deviation is even smaller. The electric force functions $f_{||}$, f_{\perp} and f_{Γ} for electrostatic interaction between two neutral conducting spheres are calculated according to Chapter 6. Zhang⁵ earlier presented a similar expression for the total relative velocity using three of ten electric force functions F_1 - F_{10} defined by Davis⁶, who used bispherical coordinates to calculate the electrostatic interaction between two conducting spheres. Zhang refers to them as F_1 , F_2 and F_3 but does not specifically state that he uses the force functions F_1 , F_2 and F_8 as referred to by Davis for interaction between neutral spheres. This is possibly the reason for the mentioned discrepancy between Zhang's results and the results presented in this thesis.

For a specific viscosity ratio μ^* , all required size ratios λ and 50 values of s in the range $-4 < \log(s-2) < 1$, the functions L , G , $f_{||}$, f_{\perp} and f_{Γ} are calculated prior to the trajectory analysis. Cubic spline interpolation allows fast retrieval of the function values at any point in this range of s with a relative error $< 10^{-5}$. For $s > 12$ all mobility functions are approximated by the far field asymptotic expressions presented by Zhang and Davis³ due to Hetsroni and Haber², and the electric force functions by the expressions resulting from the one image approximation (Eqs. 6.13 and 6.14)

$$f_{||} = p_{||} p_{2||} \quad , \quad f_{\perp} = p_{1\perp} p_{2\perp} \quad , \quad f_{\Gamma} = \frac{p_{1||} p_{2\perp} + p_{1\perp} p_{2||}}{2} \quad ,$$

where

$$p_{i||} = \frac{1 + 2a_{3-i}^3 r^{-3}}{1 - 4a_i^3 a_{3-i}^3 r^{-6}} \quad , \quad p_{i\perp} = \frac{1 - a_{3-i}^3 r^{-3}}{1 - a_i^3 a_{3-i}^3 r^{-6}} \quad .$$

7.3. Trajectories

Relative trajectories $\mathbf{s}(t) = (s, \vartheta, \varphi)(t)$ are calculated numerically using a very simple but effective near second order algorithm. Time is eliminated by defining a normalized

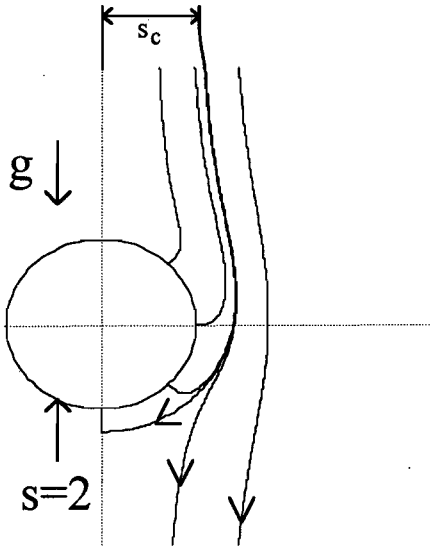


Fig.7.3. Relative trajectories for two spherical drops due to gravity and van der Waals interaction for $a_1 = 10^{-6}$ m, $\mu^* = 1$ and other conditions of Fig.7.2.

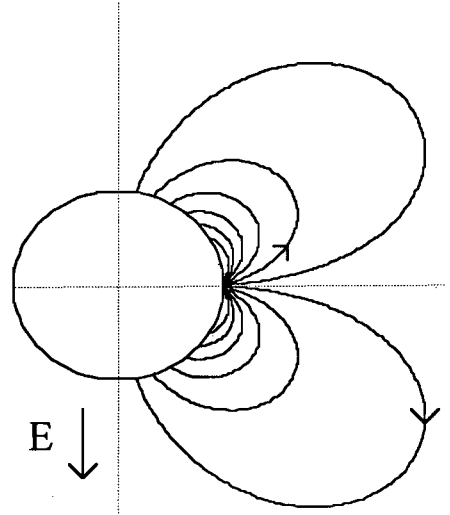


Fig.7.4. Relative trajectories for two spherical drops due to a vertical electric field ($\alpha = 0$) $a_1 = 10^{-5}$ m, $\mu^* = 1$ and other conditions of Fig.7.2.

velocity vector $\mathbf{v}^* = \mathbf{v}/|\mathbf{v}|$, $\mathbf{v} = (v_r, v_\vartheta, v_\varphi)$. Knowing velocity \mathbf{v}_1^* at s_1 , velocity \mathbf{v}_2^* is calculated at the estimated point $s_2 = s_1 + h \cdot \mathbf{v}_1^*$. If the condition $|\mathbf{v}_2^* - \mathbf{v}_1^*| < \kappa$ is true, where κ will be called the trajectory accuracy, then a step is taken according to $s_2 = s_1 + h \cdot (\mathbf{v}_1^* + \mathbf{v}_2^*)/2$, otherwise h is halved and new estimates for s_2 and \mathbf{v}_2 are calculated until the required condition is met. If $|\mathbf{v}_2^* - \mathbf{v}_1^*| < \kappa/2$, then h is doubled before the next step. Using the already calculated velocity \mathbf{v}_2 as \mathbf{v}_1 in the next step, leads to only one velocity calculation per step, as long as h is small enough. The step size h is given a minimal value of 10^{-6} , allowing very large curvatures. It should be realized that constant spherical velocity components allow large steps.

Figure 7.3 shows some relative trajectories induced by gravity and van der Waals interaction. At the indicated surface $s = 2r/(a_1 + a_2) = 2$ the considered drops touch one another. The critical dimensionless horizontal displacement $s_c = s \cdot \sin \vartheta$ for $s \rightarrow \infty$, which just leads to coalescence, is determined backwards from $s = (2, \pi', 0)$ to $s = \infty$, where $\pi' = \pi - 10^{-5}$ (large enough single precision offset). The trajectory from $s = (2, \pi', 0)$ to $s = (s_f, \vartheta_f, 0)$ is calculated numerically using Eq.7.4. Just below the $s=2$ surface the gravity and van der Waals interaction induced velocities compensate one another, leading to the 90° angle in the trajectory. The trajectory from $s = s_f \geq 9$ to $s = \infty$, where only gravity is important, may be calculated analytically using the large-distance mobility functions L and M presented by Zhang and Davis³

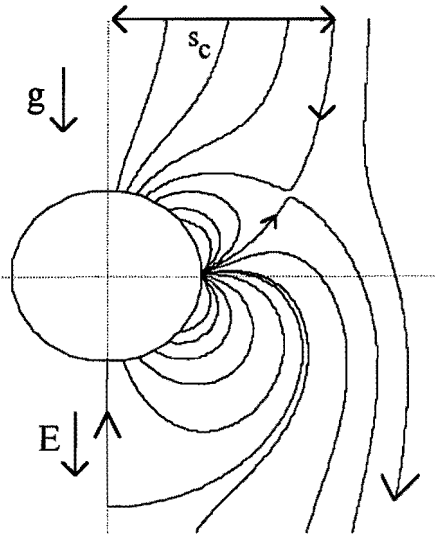


Fig.7.5. Relative trajectories for two spherical drops due to gravity and a vertical electric field ($\alpha=0$), $\mu^*=1$ and other conditions of Fig.7.2.

$$s_c = s_\infty \sin \vartheta_\infty = s_f \sin \vartheta_f \exp\left(\int_{s_f}^{\infty} \frac{L-M}{sL} ds\right) \\ \approx s_f \sin \vartheta_f L^{1/2}(s_f) \quad (7.5)$$

where the use of $L^{1/2}$ is only valid for the large distance case. The resulting relative accuracy of s_c was found to be approximately equal to the trajectory accuracy κ .

Figure 7.4 shows some relative trajectories for two drops induced by just a vertical electric field ($\alpha=0$). Arp and Mason¹¹ earlier presented similar trajectories for two equal, hard spheres. Figure 7.5 shows the relative trajectories for two drops due to gravity and a vertical electrical field. The contribution from the van der Waals interaction is insignificant in this case. For this case the critical horizontal displacement s_c cannot be determined backwards starting at $s=(2, \pi', 0)$. The value of s_c is now related to another point where the gravity- and electric field-induced velocities compensate one another, and is determined by forward trajectory analysis starting with a trial value for s_c at $s=\infty$ that is systematically varied. To reduce the calculation time a large initial value for the trajectory accuracy κ is chosen which is decreased along with the step size for the trial value s_c , using a factor $2/3$ instead of $1/2$ so less accurate initial trajectories may be overruled. The limiting value $s_f > 9$ for the analytical trajectory analysis is now chosen large enough so for $s > s_f$ the electric field induced velocity is negligible ($v_E(s_f) \ll v_g$).

7.4. Collision cross section

The collision cross section may be imagined as an area at infinity around the $\vartheta=0$ axis, for the axisymmetrical case ($\alpha=0$) given by a circle. In the asymmetrical case ($\alpha \neq 0$) the collision cross section is not circular and is calculated by determining first the values $x_{c,\pi}$ and $x_{c,0}$ for $\varphi=\pi$ and $\varphi=0$ and then a critical value y_c for several values of $x_{c,\pi} < x_c < x_{c,0}$, according to the already mentioned trial method. Both x_c and y_c are scaled the same as s_c . A trial value for the pair (x_c, y_c) leads to $s_c^2 = x_c^2 + y_c^2$, $\varphi = \arctan(y_c/x_c)$ and, using Eq.7.5 and the condition $v_E(s_f) \ll v_g$, to the starting point $(s_f, \vartheta_f, \varphi)$ for the numerical trajectory analysis

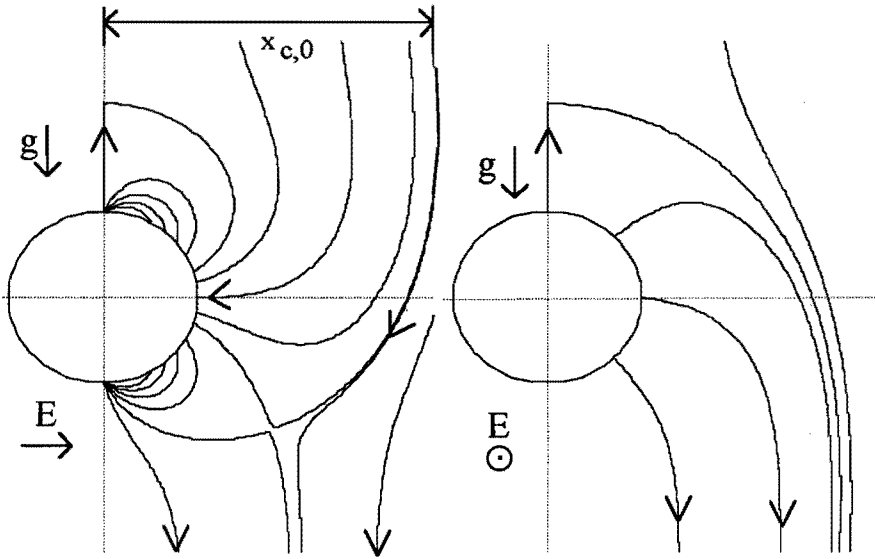


Fig.7.6. Relative trajectories for two spherical drops due to gravity and a horizontal electric field ($\alpha = \pi/2$) for azimuth angles $\varphi = 0, \varphi = \pi/2$, respectively, $\mu^* = 1$ and other conditions of Fig.7.2.

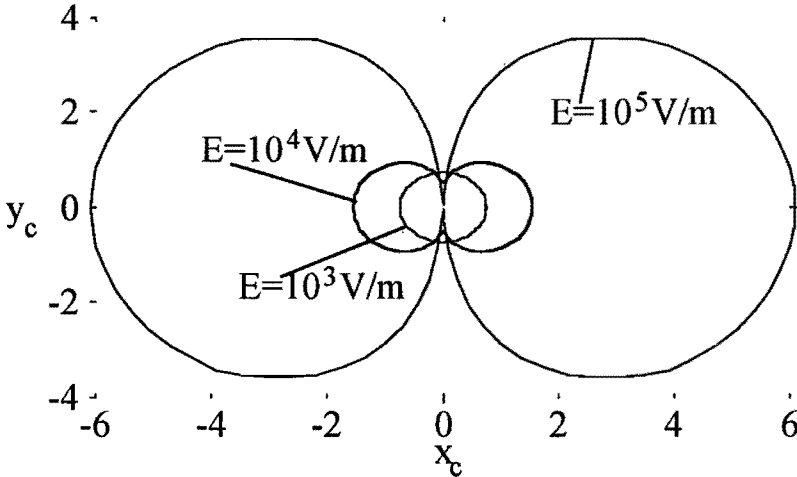


Fig.7.7. Dimensionless collision areas for three different horizontal electric fields and other conditions of Fig.7.2.

for $s < s_f$. Figure 7.6 show some trajectories in the planes $\varphi = 0$ and $\varphi = \pi/2$ for a horizontal electric field. The trajectories are obviously not symmetrical around the $\vartheta=0$ axis and for $0 < \varphi < \pi/2$ the azimuth velocity v_φ is unequal to zero. Figure 7.7 shows the resulting dimensionless collision cross section for three values of a horizontal field.

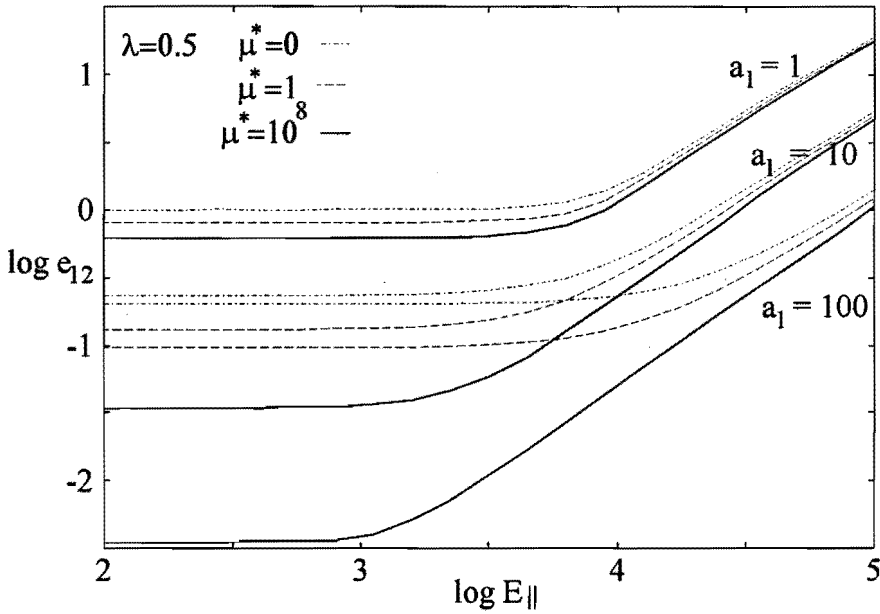


Fig.7.8 Collision efficiency e_{12} as function of a vertical electric field ($E_{\parallel}g$) for three viscosity ratios and three sizes (μm).

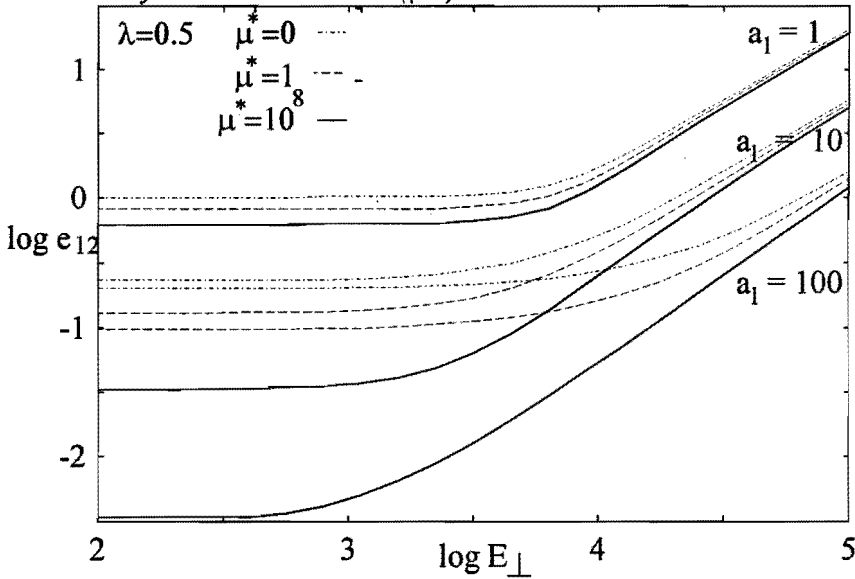


Fig.7.9 Collision efficiency e_{12} as function of a horizontal electric field ($E_{\perp}g$) for three viscosity ratios and three sizes (μm).

The collision efficiency e_{12} for drop 1 and 2 is defined as the ratio of the actual collision cross section and the collision cross section resulting from rectilinear approach³ $\pi(a_1 + a_2)^2$, and for $\alpha=0$ is given by $e_{12} = s_c^2 / 4$. For $\alpha \neq 0$ it is given by

$$e_{12} = \frac{1}{2\pi} \int_{x_{c\pi}}^{x_{c0}} y_c(x_c) dx_c \tag{7.6}$$

where the symmetry with respect to the plane $\varphi = 0$ is used. For $\alpha = \pi/2$ the collision cross section is also symmetrical with respect to $\varphi = \pi/2$, so $x_{c\pi} = -x_{c0}$. Equation 7.6 is then evaluated numerically from $x = 0$ to $x = x_{c0}$ using Gauss-Legendre integration.

Figures 7.8 and 7.9 show the collision efficiencies for three values of the viscosity ratio μ^* , and three values of the larger sphere size a_1 and $\lambda = 0.5$ as functions of the vertical electric field and the horizontal field respectively. For low values of the electric field the efficiencies are determined by the van der Waals interaction. Contrary to results presented earlier by Zhang⁵, all efficiencies increase similarly on the high field side for both field directions.

7.5. Height-dependent size distribution.

The gravity-induced collision rate⁵ $J_{ij} = n_i n_j \pi (a_i + a_j)^2 e_{ij} v_g$, where n_i is the number density, a_i the average radius for size category i , e_{ij} is the collision efficiency and v_g is the gravity induced relative velocity, leads to a changing drop size distribution which remains homogeneous. In a limited experimental cell however, an initially homogeneous drop size distribution will evolve into a height-dependent distribution, due to the rapid settling of large drops.

To predict the evolution of the drop distribution in a limited cell, the drops are not only divided in a discrete number of size categories, with drop radii a_i equidistant on a logarithmic scale, but also in a discrete number of linear height categories $h_n = n \cdot \Delta h$. Fig. 7.10 shows an example of 20 different categories, where each category represents the drops of a specific size category in a slab of thickness Δh at a specific height. Different height categories are geometrically separated, but different size categories at equal heights are located at the same position in space, unlike the schematic representation in fig. 7.10.

The relative dimensionless displacement s_i for drops of size category i during a time step Δt due to the gravity-induced velocity is given by

$$s_i = v_i \frac{\Delta t}{\Delta h}, \quad v_i = a_i^2 \frac{2g\rho}{9\mu_c \chi} \quad (7.7)$$

In the following considerations it is assumed that i represents the category of the smaller size, and j the category of the larger size: $i \leq j$, while k and m refer to the height categories. Collisions between slightly different drops within one size category $i = j$ are neglected. The number of collisions per unit volume for drops of the

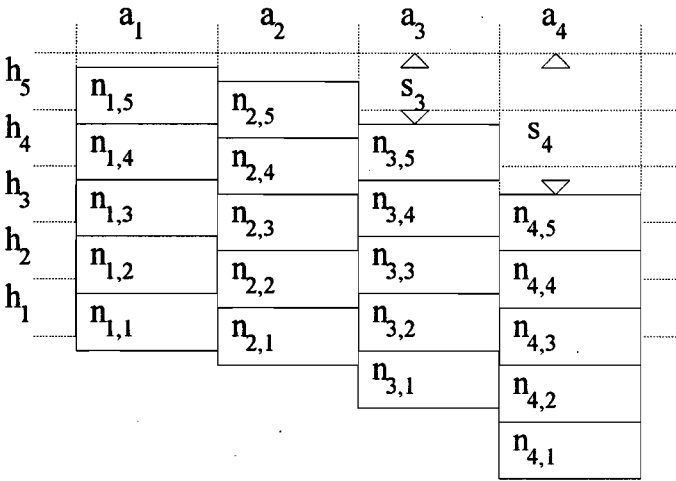


Fig. 7.10. Schematic representation of a small set of categories with different values for height h_k and size a_i . Before a time step the categories are located according to the dotted lines, i.e. $s_k=0$, after a time step all categories have settled over different distances s_k as shown.

categories $(i,k)(a_i,h_k)$ and $(j,m)(a_j,h_m)$ with the number densities $n_{i,k}$ and $n_{j,m}$ during a time step is given by

$$N_{i,k;j,m} = f_{i,k;j,m} n_{i,k} n_{j,m} e_{i,j} \pi (a_i + a_j)^2 \Delta h \quad (7.8)$$

where the factor $f_{i,k;j,m} \leq 1$ accounts for the fact that two categories have a specific changing space fraction in common during a time step. If category (j,m) moves from a position entirely above to a position entirely below category (i,k) , then $f_{i,k;j,m} = 1$. If the smaller drops are positioned higher ($k > m$) then $f_{i,k;j,m} = 0$. The values of $f_{i,k;j,m}$ for $k \leq m$ are shown in Table 7.1 as function of $p = s_{ij} \bmod 1$ ($0 < p < 1$),

Table 7.1. The third column gives the factor $f_{i,k;j,m}$ that is used in Eq.8 for collisions between categories (i,k) and (j,m) as function of $p = s_{ij} \bmod 1$ ($0 < p < 1$), where $s_{ij} = s_j - s_i$ is the relative displacement for size categories i and j according to Eq.7.

$k = m$	$s_{ij} < 1$	$p - p^2 / 2$
„	$1 < s_{ij}$	$1/2$
$k < m$	$s_{ij} < m - k - 1$	0
„	$m - k - 1 < s_{ij} < m - k$	$p^2 / 2$
„	$m - k < s_{ij} < m - k + 1$	$1/2 + p - p^2 / 2$
„	$m - k + 1 < s_{ij}$	1

where $s_{ij} = s_j - s_i$ is the relative displacement of two categories. Equation 7.8 is valid if the calculated number of collisions is relatively small compared to the number of drops in both categories. This is achieved by choosing Δt small enough. An accurate height dependence is obtained by choosing Δh small enough. The number of drops in category i, m with the smaller size decreases with the number of collisions $\Delta n_{i,k} = -N_{i,k;j,m}$, and their volume is taken over by category (j, m) . Due to the total volume fraction taken over by category (j, m) from all other categories during a time step, a number of drops is transferred to the next size category at the same height $(j+1, m)$

$$\Delta n_{j+1,m} = -\Delta n_{j,m} = \frac{\sum_{i < j} \left(\sum_{k \leq m} n_{i,k;j,m} a_i^3 \right)}{a_{j+1}^3 - a_j^3} \quad (7.9)$$

In the experimental data the categories for the largest size remain empty, so any transfer from these categories is irrelevant. During a time step categories (j, m) are modified as close as possible to the chronological order, i.e. starting with the largest value of j and for each j with the smallest value of m . After modifying all displaced categories during a time step, new categories are defined to contain two fractions p_i and $1-p_i$ according to the displacement s_i of two previous categories, e.g. the new categories n_{11}' and n_{15}' for the next time step in Fig.7.10 are given by $n_{11}' = 1/4 \cdot n_{12} + 3/4 \cdot n_{11}$ and $n_{15}' = 3/4 \cdot n_{15}$.

7.6. Results and discussion.

The presented model is compared to the measured evolution of the size distribution of water drops in kerosene during electrostatic coalescence (Fig.5.5). The relevant properties of the experimental system are the density difference, gravity constant,

$$\rho = 180 \text{ kg m}^{-3}, g = 9.8 \text{ ms}^{-2},$$

continuous phase dielectric permittivity, electric field strength,

$$\epsilon_c = 2.3 \cdot \epsilon_0, E_{\text{eff}} = 3 \cdot 10^5 \text{ V/m (a.c. 50Hz)},$$

the conductivities and the viscosities of the dispersed and continuous phase,

$$\sigma_d = 4 \cdot 10^{-6} \text{ mho/m}, \sigma_c = 10^{-11} \text{ mho/m}$$

$$\mu_d = 10^{-3} \text{ Pa s}, \mu_c = 1.6 \cdot 10^{-3} \text{ Pa s},$$

and the surface tension

$$\gamma = 0.05 \text{ N/m}$$

For the conductivity of the dispersed phase the value of pure water is given here, while actually demineralized water with a higher conductivity is used. The drops may be regarded as conducting spheres if the ratio $\beta = (\epsilon_d - \epsilon_c) / (\epsilon_d + 2\epsilon_c)$ in Eqs.6.5 and 6.6 is very close to one. The total dielectric permittivity of a medium

$$\varepsilon = \varepsilon_r \varepsilon_0 - 4\pi i \sigma / \omega \quad (10)$$

has a real part that depends on the relative dielectric permittivity ε_r , and an imaginary part that depends on the conductivity σ . For the continuous phase and $\omega / (2\pi) = 50\text{Hz}$ the second term in Eq.10 is relatively small and ε_c is real. The dispersed phase permittivity ε_d however, is completely determined by the second term, i.e. the conductivity σ_d , and is much larger than ε_c . This leads to a value for β that deviates less than 10^{-4} from $\beta = 1$, allowing the assumption of conducting spheres. At "optical" frequencies ($c/\lambda \approx 5 \cdot 10^{14}\text{Hz}$) the contribution from the second term in Eq.10 to ε_d may be neglected, allowing the use of a real refractive index $n_d = \sqrt{\varepsilon_d}$ in the calculation of the light scattering matrices.

For a typical drop radius $a = 30\mu\text{m}$ falling due to gravity the Reynolds number is given by $\text{Re} = v_g \cdot a \cdot \rho / \mu_c = 2a^3 \rho^2 g / (9\mu_c^2) \approx 2.8 \cdot 10^{-4}$. For two drops with radius $a_1 = 30\mu\text{m}$, $\lambda = 0.5$ at a relative distance $s-2 = 10^{-2}$ approaching due to an electric field (Fig.7.2) the Reynolds number for the near contact area is given by $\text{Re} = v_E G f_{ij} \cdot a_1 s \cdot \rho / \mu_c \approx 5 \cdot 10^{-3}$, i.e. the creeping flow condition are satisfied for the major part of the drops trajectories.

The validity of the assumption that a drop with radius $a = 30\mu\text{m}$ remains spherical depends on the ratio of the surface tension induced pressure $p = 2\gamma / a$ and the largest electrical pressure $p = \varepsilon_c E^2 / 2$ at the sphere surface, i.e. at $\psi = 0$. This ratio also appears in the expression of O'Konski¹² for the eccentricity of a drop in an electric field, where the drop is assumed to obtain a prolate shape with major axis a' and minor axis b , satisfying $a^3 = a'b^2$. The eccentricity e is given by $e^2 = 1 - b^2 / a'^2 = 3/2 \cdot \varepsilon E_0^2 a / \gamma \approx 0.002$, i.e. $a'/b = 1.001$. This small deformation was found for the surface tension and electric field induced pressures $2\gamma / a = 3000$ and $\varepsilon_c E^2 / 2 \approx 10$, where $E = 3 \cdot E_0$ at $\psi = 0$ is used. For two equal drops at relative distances $s-2 = 10^{-1}$ and $s-2 = 10^{-2}$ the field between the drops is approximately ten and hundred times (see appendix 3) the applied electrical field leading to $\varepsilon_c E^2 / 2 \approx 10^2$ and $\varepsilon_c E^2 / 2 \approx 10^4$. If the deformation is also presented as the ratio of major and minor axis it changes between the distances $s-2 = 10^{-1}$ and $s-2 = 10^{-2}$ from $a'/b = 1.01$ to an impossible value, i.e. from a small deformation to completely deformed. Because the time that two drops require to move from $s-2 = 10^{-1}$ to coalescence is very small the assumption of randomly oriented spheres during light scattering measurement and also for the electrostatic coalescence model is correct for the considered experimental situation.

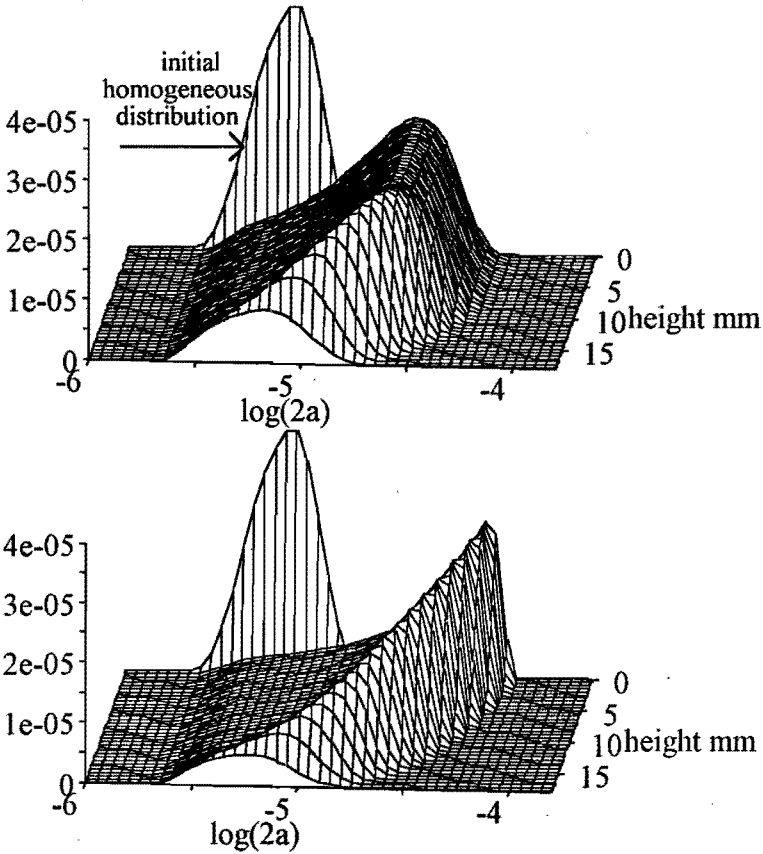


Fig.7.11. Calculated size-height distributions after 145 and 219 seconds for the also shown initial distribution, which is assumed homogeneous, i.e. independent of height. The z-axis gives the volume fraction per category. After 145 seconds the lower half is still homogeneous. The total initial water fraction is $3.2 \cdot 10^{-4}$.

The hydrodynamic pressure between the drops that may also be calculated exactly for spherical drops (Haber and Hetsroni^{1,2}) partially compensates the electric field induced deformation at small distances, extending the valid range a little. For the considered size range and the given electric field a realistic Hamaker constant has no influence on the collision efficiency (Fig. 7.9) and is of no importance in this case. The considered size range has 45 categories, 20 categories per decade, and center radii $a_{i+1} = 1.122 \cdot a_i$, $a_1 = 1 \mu\text{m}$, while 36 height categories with $\Delta h = 0.5 \text{mm}$ are considered.

Figures 7.12 and 7.13 show the total volume fraction ϕ and the values of d_{10} , d_{50} and d_{90} , i.e. the upper drop diameters for 10%, 50% and 90% of the total volume fraction, of a measured evolution of the drop size distribution, corresponding with Fig.4.5.

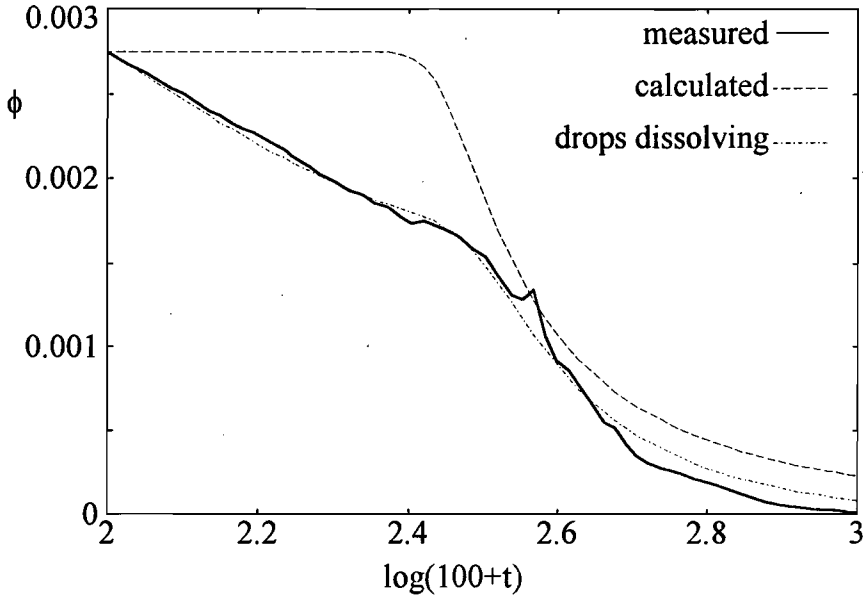


Fig.7.12. The total volume fraction of water in kerosene during electric field enhanced coalescence, both measured and calculated with and without accounting for slowly dissolving drops. The chosen logarithmic time scale for (t in seconds) shows the initial stage better.

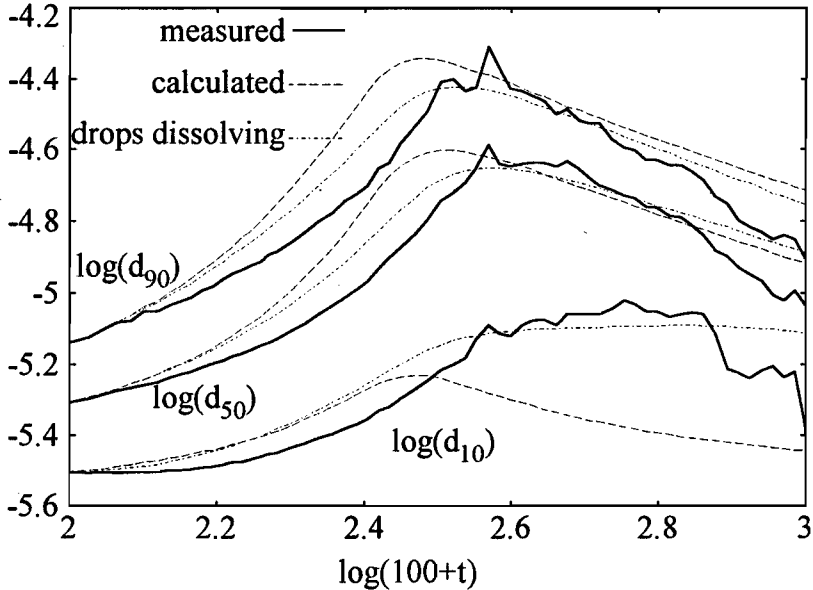


Fig.7.13. Upper diameters ($d=2a[m]$) d_{10} , d_{50} and d_{90} for 10%, 50% and 90% of the total volume fraction as shown in Fig.12.

These very low fractions of water allow the negligence of settling hindrance by other drops.

Figure 7.11 shows two examples of calculated size-height distributions using the corresponding initial size distribution. During the forward light scattering measurements only a circular part of the lower 8mm of the emulsion is monitored, and a corresponding part of the simulated settling distribution leads to a calculated size distribution as function of time. The thus calculated total volume fraction ϕ and diameters d_{10} , d_{50} and d_{90} are also shown in Figs.7.12 and 7.13. The relative size distribution is initially quite accurate but starts to deviate after $t=25$ seconds ($\log(100+t)=2.1$). The main difference, however, is between the measured and the calculated total fraction ϕ as function of time. The calculated fraction initially remains constant while the measured fraction decreases. This decrease may be explained by the assumption that, due to a higher solubility of water in kerosene in an electric field, the water drops slowly dissolve. If Fickian diffusion of water from the saturated kerosene at the drop surfaces into the bulk is assumed, then the calculated total fraction, and also the diameters d_{10} , d_{50} and d_{90} deviate less from the measured values. Quasi stationary diffusion in spherical coordinates leads to $4\pi a_i^2 (da_i / dt) = D\Delta C a_i$, where $D(\text{m}^2 / \text{s})$ is the diffusivity and $\Delta C (\text{m}^3 / \text{m}^3)$ is the concentration difference between the bulk and the drop surface. The best fit was found for $D\Delta C = 6 \cdot 10^{-14}$. The smallest drops dissolve completely during a time step. Some larger drops are transferred to smaller-size categories. The total water volume, both contained by drops and dissolved in the kerosene, remains unchanged. The measured decrease of d_{10} is also explained. This suggested explanation for the discrepancies between measured and calculated evolution of the size distribution should actually be verified with other experiments. Other possible depletion mechanisms, which accounts for drops being attracted towards images or actual drops on the electrodes, or Oswald ripening from drops towards the wetted electrodes, or position dependent shear initiated coalescence through electrohydrodynamic circulation in the cell, are not quantified.

7.7. Conclusion.

The calculation is presented of collision efficiencies and collision rates for conducting neutral spherical drops in an electric field in a limited experimental cell. Contrary to results presented earlier⁵, the horizontal and vertical field cases lead to similar collision efficiencies. The calculated evolution of the drop size distribution during electrostatic coalescence is compared to a measured evolution and agrees beyond expectation. A few not explained discrepancies, however, remain to be solved.

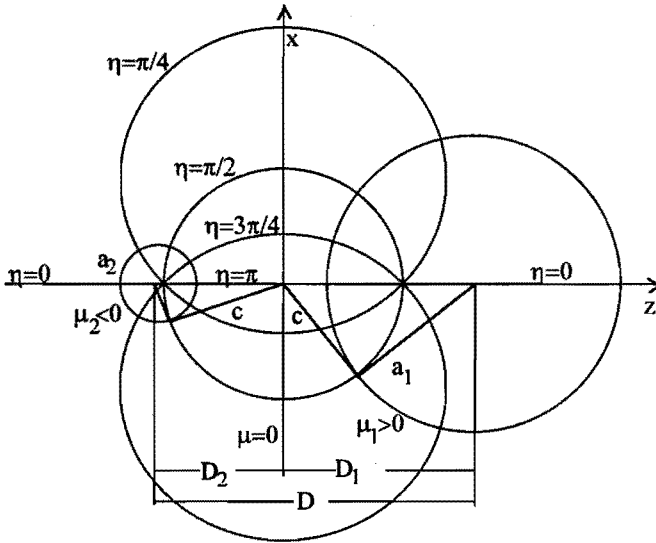


Figure 7.14. The bispherical coordinate system is axisymmetrical around the z-axis.

Appendix 1.

The coordinate transformation between the bispherical (bipolar) coordinate system (μ, η, φ) , as used by several authors^{1,6,10} to solve two sphere problems, and Cartesian coordinates (x, y, z) is given by

$$x = \frac{c \cdot \sin \eta \cdot \cos \varphi}{\cosh \mu - \cos \eta}, \quad y = \frac{c \cdot \sin \eta \cdot \sin \varphi}{\cosh \mu - \cos \eta}, \quad z = \frac{c \cdot \sinh \mu}{\cosh \mu - \cos \eta},$$

where

$$c^2 = D_1^2 - a_1^2 = D_2^2 - a_2^2, \quad D_1 + D_2 = D$$

(Fig.7.14). The spheres with radii a_1 and a_2 are given by the surfaces $\mu = \mu_1$ and $\mu = \mu_2$, respectively.

Appendix 2.

The expression presented by Hamaker^{3,9} for the potential energy Φ of two spherical particles due to the non-retarded van der Waals interaction

$$\Phi = -\frac{A}{6} \left[\frac{2a_1 a_2}{f_p} + \frac{2a_1 a_2}{f_m} + \ln \frac{f_p}{f_m} \right], \quad f_p = r^2 - (a_1 + a_2)^2$$

$$f_m = r^2 - (a_1 - a_2)^2$$

leads to the following expression for the mutual attractive force

$$F_A = -\frac{d\Phi}{dr} = \frac{A}{6} \left[\frac{-4ra_1 a_2}{f_p^2} + \frac{-4ra_1 a_2}{f_m^2} + \frac{f_m}{f_p} \frac{2r(f_m - f_p)}{f_m^2} \right]$$

$$= -\frac{A}{6} 4ra_1 a_2 \left[\frac{f_m^2 + f_p^2 - 2f_m f_p}{f_p^2 f_m^2} \right] = -\frac{A (4a_1 a_2)^3 r}{6 (f_p f_m)^2}$$

Substituting $a_2 = \lambda a_1$, $r = sa_1(1+\lambda)/2$, $f_p = a_1^2(1+\lambda)^2(s^2-4)/4$ and $f_m = a_1^2(s^2(1+\lambda)^2 - 4(1-\lambda)^2)/4$ leads to the attractive force

$$F_A = -\frac{A s}{6} \frac{4^3 \lambda^3}{2a_1 (1+\lambda)^3} \left(\frac{4}{s^2-4} - \frac{4}{s^2(1+\lambda)^2 - 4(1-\lambda)^2} \right)^2$$

Appendix 3.

Figure 7.15 shows the electric field in the middle between two equal spheres or the field on a conducting plate near a conducting sphere, as function of the dimensionless distance $s = 2r/(2a)$ between the spheres centers or sphere and image centers. The solid line is the exact solution according to chapter 6, that is compared to the small and large distance asymptotic approximations of the exact solution of Davis⁶ that were presented by Arp and Mason¹¹

$$E = E_0 \frac{2\pi^2}{3(s-2) \ln\left(\frac{s-2}{\gamma^*}\right)}, \quad E = E_0 \left(1 + \frac{32}{s^3}\right)$$

where $\gamma^* = 12.689$ is derived from Euler's constant.

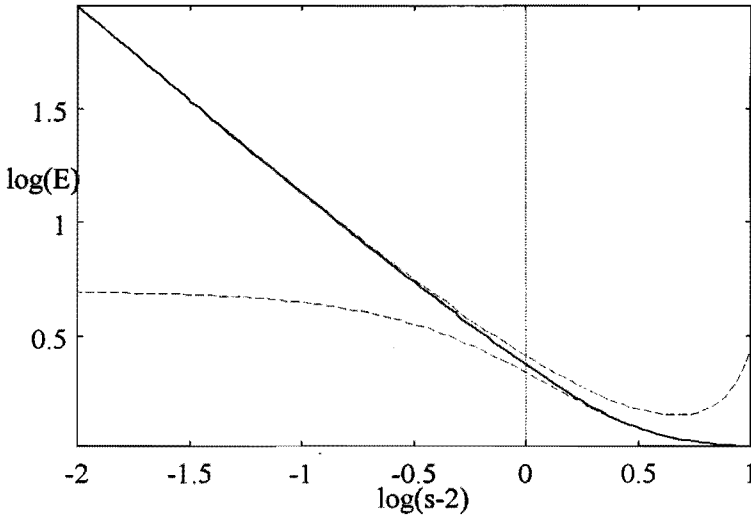


Fig.7.15. The electric field E in the middle between two equal spheres as function of the dimensionless distance s . The solid line gives the exact solution of Chapter 6, while the dotted lines present asymptotic approximations.

references

- ¹ S. Haber, G. Hetsroni and A. Solan, *Int. J. Multiphase Flow* **1**, 55 (1973).
- ² G. Hetsroni and S. Haber, *Int. J. Multiphase Flow* **4**, 1 (1978).
- ³ X. Zhang and R. H. Davis, *J. of Fluid Mech.* **230**, 479 (1991).
- ⁴ G. K. Batchelor, *J. of Fluid Mech.* **119**, 379 (1982).
- ⁵ X. Zhang, *AIChE Journal* **41**, 1629 (1995).
- ⁶ M.H. Davis, *Quart. J. Mech. Appl. Math.* **17**, 499 (1964).
- ⁷ C. D. Hendricks and S. E. Sadek, *IEEE Trans. Ind. Appl.* **IA-13**, 489 (1977).
- ⁸ S. E. Sadek and C. D. Hendricks, *Ind. Eng. Chem., Fundam.*, **13**, 139 (1974).
- ⁹ H. C. Hamaker, *Physica* **4**, 1058 (1937).
- ¹⁰ A. Z. Zinchenko, *Prikl.mat. mech.* **44**, 955 (1980).
- ¹¹ P. A. Arp and S. G. Mason, *Colloid Polym. Sci.* **255**, 566 (1977).
- ¹² O'Konski, C.T. and Thacher, H.C.Jr., *J.Phys.Chem.* **57**,955 (1953).

Chapter 8. Conclusions

8.1. Forward light scattering

In this thesis a method has been presented to study electrostatic coalescence quantitatively by determining the evolution of the size distribution of conducting drops in an insulating continuous phase in an electric field. For this purpose the forward scattering pattern is measured due to a laser beam incident on a dilute dispersion of water drops in kerosene in an experimental cell. The perfect spherical shape of the small water drops allows exact calculations of the scattering pattern of individual drops according to Mie. Although the experimental work is limited to drop sizes for which exact scattering patterns may be calculated within a reasonable time, attention was also given to the faster geometrical optics approximation, required for large spheres. This known approximation may be improved by adding a so called physical optics approximation for glory rays and a separate edge contribution to the forward scattering amplitude. A simple expression for the glory rays is derived from a known asymptotic approximation of the rigorous Mie scattering (chapter 3). To deduce a size distribution from a measured scattering pattern a scattering matrix may be calculated that consists of the averaged scattering patterns of a number of discrete size categories. It is demonstrated that knowledge of the separate contributions to the total scattering pattern and a specific required accuracy for this scattering matrix leads to minimal averaging conditions. These averaging conditions depend on the size and the relative refractive indices and apply for both exact and the approximate calculations (chapter 4). The scattering matrix only gives the correct relation between the measured scattering pattern and size distribution if multiple scattering is negligible. A multiple scattering inversion method is also presented, that calculates the redistribution of a discrete forward scattering pattern due to a thin single scattering slab perpendicular to the laser beam, leading after a number of such slabs to a multiple scattering pattern, that may be compared to the measured scattering pattern, and is used to modify an estimated single scattering pattern and size distribution for one slab (Chapter 5). The transparent walls of the experimental cell were made of perspex, that contrary to glass is hydrophobic in a kerosene environment, and less water drops attach to the walls. Due to the inferior surface quality of perspex, five cells were made initially, of which only two could be used to obtain usable scattering measurements. Later on five extra cells were made of which not a single one was usable. The scattering pattern resulting from just the cell walls of these cells was already quite large, making the inversion of the measured scattering patterns to size distributions less reliable.

8.2. Electrostatic coalescence

The resulting measured evolution of the size distribution of water drops is compared to the evolution according to a model that only considers binary interactions between drops in dilute dispersion, due to gravity, an electric field and the unretarded van der Waals force. Inertial forces, drop deformation and surface tension gradients are neglected. For the calculation of the electrostatic force between two spherical drops an exact calculation method based on electrical images is presented (Chapter 6). The relative velocity due to the three mentioned forces is calculated using exact solutions for quasi static hydrodynamic interaction between two fluid spheres. For very small distances the attractive electrostatic force may become very high so inertial forces and deformation of the drop will become important. The surface tension gradients in our experimental case was not large enough to lead to a remaining kerosene film between two water drops in an electrical field, but this does not directly justify its negligence. A calculation method that accounts for a surface tension gradient in two drop interaction is however not available yet. The relative velocity leads to relative trajectories and collision cross sections, due to the fact that only gravity induces a large distance relative velocity. The resulting evolution of a drop size distribution, using a measured initial distribution has however a significant difference with the measured evolution. The measured total fraction of water contained by drops in the dispersion decreases, while the model predicts that the total fraction remains initially constant. A higher solubility and thus a better diffusion of water in kerosene in an electric field leads to a better agreement between the calculated and the measured evolution of the drop size distribution. Besides the so far mentioned discrepancies between the model and reality, another difference with commercially used coalescers is that also shear instead of only gravity induces the first approach of two drops. Fuentes, Kim and Jeffrey^{1,2} have already presented some calculations for this case using velocity images.

1. Fuentes, Y.O., Kim, S and Jeffrey, D.J. *Phys.Fluids* **31**, 2445 (1988).
2. Fuentes, Y.O., Kim, S and Jeffrey, D.J. *Phys.Fluids* **A1**, 61 (1989).

List of symbols

a	sphere radius
a', b	spheroidal axis's
A	rainbow parameter (section 3.3), Hamaker constant
\mathbf{A}	Scattering matrix
a_n, b_n	Mie scattering coefficients
\mathbf{b}	discrete scattering pattern
c	wave velocity
C_{ext}	extinction cross section
d	distance (between centers of spheres)
D	geometrical divergence (Eq.2.23)
$e_{i,j}$	collision efficiency
\mathbf{E}, E	electric field strength, diffraction envelope function
Err	maximum deviation for scattering matrix calculation
f, f'	asymptotic phases (Eqs.3.5 and 3.6)
f_n, f_x	factor for subsequent discrete angles and size categories, respectively
$f_{ }, f_{\perp}, f_{\Gamma}$	electric force functions
FL	focal length of lens
\mathbf{F}	force vector, charge induction matrix (Eq.6.32)
g	size distribution function (Eq.5.10), gravity
G	phase of glory ray (Eq.3.13), forward $p=1$ modulus (Eq.4.14),
$G_{i,j,k}$	function relating axisymmetric solid angles (Eq.5.5)
G, H	hydrodynamic mobility functions
\mathbf{H}	smoothing matrix (Eq.5.1)
i, i_j	$\sqrt{-1}$, intensity function
I	light intensity
$J_{0,1,2}$	integer Bessel functions of the first kind
\mathbf{k}, k	wave vector, wave number
K	averaging number in one solid angle (Eq.4.3)
L	number of times that a glory ray passes the optical axis
L, M	hydrodynamic mobility functions
m	relative refractive index n_2 / n_1
M	Number of single scattering slabs
$\text{Min}(,)$	minimum of two values
n	refractive index, integer value
N	number of electric image positions
p	number of internal paths of a light ray, dipole component
P	averaging number in one size category

p	dipole
P	array of aligned dipole components
q	sign: $-1,+1$ (Ch.2), $(1+m^2)^{1/2}x^{-1/3}$ (Ch.3), point charge (Ch.6)
Q_{ext}	extinction efficiency
Q	array of point charges
r, r_j	spherical coordinate, reflection coefficient
r	(relative) position vector
R	detector radius
R	redistribution matrix
s	sign $(-1,+1)$, dimensionless distance $2r/(a_1+a_2)$ (Ch.7)
S_j	amplitude function
t	time
T_j	edge function
u	parameter defined below Eq.3.10
u_o, u_i	asymptotic phase functions (Eqs.3.5 and 3.6)
v	(relative) velocity
V	electric potential
W_n, W_x	relative scattering angle width, relative size category width
x	size parameter $2\pi a/\lambda$
x	discrete size distribution
x,y,z	Cartesian coordinates

greek symbols

α	angle of incidence, polarizability, electric field angle (Fig.7.1)
α, β	cell wall angles
β	angle of refraction, polarizability α/a^3
γ	angle $(2/x)^{1/3}$, surface tension
δ	Kronecker delta, distance from axis
$\Delta\omega$	general phase difference
ϵ_j	dielectric permittivity, total transmission coefficient
χ	Hadamard-Rybczynski factor $(\mu^* + 2/3)/(\mu^* + 1)$
κ	trajectory accuracy
λ	wave length, size ratio
ϑ, φ	spherical coordinates
$\mu^{(*)}$	$(m-1)x^{2/3}$ (Ch.3), viscosity (ratio) (Ch.7)
$\omega/(2\pi)$	frequency
ρ	phase delay of central ray $2x(m-1)$, mass density

σ	Phase delay, electric conductivity
π_n, τ_n	spherical harmonics
τ	complementary angle of incidence $\pi/2 - \alpha$
ψ	electric field angle (Fig. 7.1)
ζ	Riemann's zeta function (Eq. 6.41)

The symbols of appendices are not all included in this list.

Curriculum Vitae

De auteur werd geboren in Gassel op 7 december 1960. Nadat hij in 1979 slaagde voor het atheneum-B op het Elzendaalcollege te Boxmeer, studeerde hij Technische Natuurkunde aan de Technische Universiteit Eindhoven, waar hij in 1988 slaagde voor het ingenieursexamen. Het afstudeerwerk bij de vakgroep Analyse van Fysische Meetmethoden onder prof. Poulis werd verricht in het Laboratorium voor Akoestiek onder begeleiding van dr.ir. H.Martin. Het in dit proefschrift beschreven promotie-onderzoek verrichtte hij van 1989 tot 1996 bij de vakgroep scheidingstechnologie van prof.dr.ir. P.J.A.M. Kerkhof op dezelfde universiteit bij de faculteit Scheikundige Technologie.

Stellingen
behorende bij het proefschrift van Erik van den Bosch

1. De dubbele oneindige sommatie voor de krachtberekening tussen twee even grote, elkaar rakende, elektrisch geleidende bollen in een elektrisch veld is een leuke wiskunde som.

"Dipole moments of conducting particle chains", T.B.Jones, J. Appl.Phys.60, 2226.

Dit proefschrift hoofdstuk 6.

2. Het feit dat de combinatie van een verticaal zwaartekrachtveld en een horizontaal elektrisch veld niet rotatiesymmetrisch is, kan door een auteur van wetenschappelijke publicaties over het hoofd gezien worden

"Theoretical prediction of electric field-enhanced coalescence of spherical drops", X.Zhang, AIChE Journal 41, 1629 (1995).

Dit proefschrift hoofdstuk 7.

3. De afleiding door Langley en Marston van een extra faseterm voor een axiaal gefocuseerde oftewel "glory" bijdrage aan licht- of geluid- verstrooiing door bolvormige deeltjes bevat een inzichtelijke fout. De betreffende faseterm volgt dan ook niet uit een asymptotische benadering van de exacte oplossing voor lichtverstrooiing.

"Forward Glory Scattering From Bubbles", D. S. Langley and P. L. Marston, Appl. Opt. 30, 3452-3458 (1991).

"Glory- and rainbow-enhanced acoustic backscattering from fluid spheres: Models for diffracted axial focusing", P. L. Marston and D. S. Langley, J.Acoust.Soc.Am.73, 1464 (1983) (Appendix B, $ka(1 - \cos\gamma)$).

Dit proefschrift, hoofdstuk 3.

4. Zowel de kracht die bij electrostatische coalescentie van een druppel water in olie met een vlak wateroppervlak voor afplatting van de druppel zorgt, als de kracht die zorgt dat de oliefilm tussen druppel en wateroppervlak leegstroomt, zijn vele malen groter dan Brown and Hanson veronderstellen.

"The effect of oscillating fields on the coalescence of liquid drops", A.H. Brown and C.Hanson, Chem.Eng.Sci.23, 841 (1968).

5. Een goede analyticus gebruikt weinig woorden om een concept uit te leggen.
"On the "dimpling" during the approach of two interfaces", S. Frankel and K.J. Mysels, J.Phys.Chem., 66, 190 (1962).
6. Bij de beoordeling van de efficiency van industriële processen komt van beide hoofdwetten der thermodynamica niet de eerste maar de tweede hoofdwet op de eerste plaats.
7. Het is verre van voor de hand liggend dat de "electronische snelweg" tot een betere wetenschappelijke-kennisoverdracht leidt, dan het gelukkig nog bestaande systeem van geaccepteerde publicaties in als goed beoordeelde wetenschappelijke tijdschriften.
"The information highway", Gianni Astarita, Chem.Eng.Sci. 51, 4353 (1996).
8. Het mondstuk van een koperen blaasinstrument is, in tegenstelling tot de algemene opinie, een sterk medebepalende factor voor de stemming van het instrument.
"Ein Beitrag zur Ermittlung der Stimmung von Blechblasinstrumenten", K. Wogram, Dissertation TU Carolo-Wilhelmina zu Braunschweig (1972).
9. De waardering voor een muzikale of wetenschappelijke prestatie hangt ook af van de persoon die de prestatie geleverd heeft.
10. Waarschijnlijk is de correlatie tussen sociale en technische vaardigheden groter dan de correlatie tussen sociale en muzikale vaardigheden.
11. De stelling dat BSE in het jaar 2003 vanzelf verdwenen zal zijn, zal binnenkort al voor een stijgende rundvleesconsumptie zorgen.